Level densities, gamma-ray strength functions and the evolution of the pygmy resonance in Sn isotopes

Heidi Kristine Toft

Thesis submitted in partial fulfilment of the requirements for the degree of Philosophiae Doctor

Department of Physics
Faculty of Mathematics and Natural Sciences
University of Oslo

March 2011

Series of dissertations submitted to the
Faculty of Mathematics and Natural Sciences, University of Oslo
No. 1047

ISSN 1501-7710

Cover: Inger Sandved Anfinsen.
Printed in Norway: AIT Oslo AS.

Produced in co-operation with Unipub.
The thesis is produced by Unipub merely in connection with the
thesis defence. Kindly direct all inquiries regarding the thesis to the copyright
holder or the unit which grants the doctorate.

Acknowledgments

First and foremost, I would like to express my deepest gratitude to my supervisors, Sunniva Siem, Magne Guttormsen and Ann-Cecilie Larsen, for your guiding in all aspects of this PhD study. Your deep knowledge of nuclear physics, technical equipment and data analysis has been very helpful. During these years, you have always been available, including during evenings, weekends, and your holidays and leaves. Your high priority to considering my questions and reading through my drafts has been very appreciated.

Without the advices and suggestions from the three of you, this thesis would not have been possible. It also would not have been possible without Sunniva's YFF, from which my position was offered.

The technical personnel at the Oslo Cyclotron Laboratory deserves a great thanks: Eivind Atle Olsen, Jon C. Wikne, and Andrey Semchenkov. You have made possible running the nuclear experiments studied in this thesis. Many times it looked dark at the start-ups of the experiments, but no problem was too hard for you to figure out and solve.

I am also very thankful to Alexander Bürger, who made, amongst other things, a sorting programme for the new SiRi detectors, which I used for the analysis of my last experiment. In addition to my supervisors and Alexander, many members of the experimental nuclear physics group at the OCL have been involved in the discussions and proof readings of the article(s): Andreas Görgen, Hilde T. Nyhus, Therese Renstrøm, Naeem Ul Hasan Syed, Gry M. Tveten, and Kristine Wikan. Several external collaborators have also contributed similarly: Undra Agvaanluvsan, Gary E. Mitchell, Andreas Schiller, and Alexander Voinov.

My supervisors, the engineers and all the people taking shifts stretched far for the successful carrying-out of the experiments and got many nights of sleep spoiled. In addition to all the names already mentioned, these kind shift takers were Trine W. Hagen, Pejman Mansouri, and Inger Eli Ruud. You spent Friday nights in the lab or showed up on Sunday mornings at 07:45. On this help, I was dependent.

It has indeed been a pleasure to be a part of the SAFE centre, both from an academic and a social point of view. I would like to thank Tomas Kvalheim Eriksen and Sunniva J. Rose, as well as all the nuclear chemists, for valuable discussions and for being a part of our centre. A special thanks to Cecilie for baking a cake on my choice to welcome me when I was new.

Finally, I owe my gratitude to my family and friends for supporting me during this PhD study in a non-technical way. This includes my parents, grandparents and Marit Sletmoen and Tore Vamraak.

Thank you!

Contents

Chapter 1

Introduction

The aim of experimental nuclear physics is to increase our knowledge of atomic nuclei under various conditions. Although the bare two-nucleon force is rather well determined, the many-particle system of an excited atomic nucleus becomes almost impossible to solve theoretically. However, at low excitation energies or for highly collective states, detailed wave functions can be derived with certain accuracy. These predictions of well-defined states and the transition rates between them can then be compared with experiments. Through this program, our understanding of the simplest nuclear excitations has been constantly increasing during the last decades.

For more complex nuclear excitations, there exist very limited information, both experimentally and theoretically. The present work concerns the study of the quasi-continuum part of the nuclear excitation regime, where individual levels are no longer resolvable with traditional experimental methods. Here, the high density of levels makes statistical averages much more relevant than the detailed descriptions of each level.

Two very fruitful statistical concepts appropriate in the quasi-continuum region and for higher energies are the level density and the γ-ray strength function. The level density is defined as the number of levels per unit of excitation energy. The γ-ray strength function characterises the average electromagnetic properties for excited nuclei as a function of γ-ray energy. The strength function is proportional to the reduced transition probability, which is independent of the density of final states.

The level density and γ-ray strength function are of fundamental importance for understanding nuclear structure and reactions involving γ-ray transitions. Local deviations from a smooth level density is expected to be due to shell gaps, breaking of nucleon Cooper pairs, and/or changes of nuclear shape. Local deviations in the strength function may indicate the presence of collective excitation modes (resonances). Both the level density and the strength function are

used for many aspects of fundamental and applied physics, including calculations of nuclear properties, like reaction cross sections. Such cross reactions are used for calculations in, e.g., reactor physics, nuclear waste management, and astrophysical models describing the nucleosynthesis in stars.

The γ-ray strength function is usually measured using photonuclear reactions for excitation energies above the particle separation energy. Here, the giant electric dipole resonances (GEDR), observed in all nuclei across the nuclear chart, dominates. This has lead to the development of several theoretical models for the low-energy tail of the GEDR. Relatively few experiments have been performed below the particle separation energies.

The Oslo method, which is developed at the OCL, makes possible a simultaneous extraction of the functional forms of both the level density and the strength function below the particle separation energy from the measured data. The observed level densities and γ-ray strength functions often deviate significantly from existing theoretical models.

During the past 15 years, level densities and γ-ray strength functions have been investigated in OCL experiments. Most of the nuclei investigated have been in the rare-earth region of $A = 140 - 180$, but some have also been lighter or heavier. Examples of interesting publications are the experimental evidence of the breaking of nucleon Cooper pairs [1], the discovery of the strongly enhanced strength function at low energies in Fe and Mo isotopes [2, 3], and the $M1$ scissor-mode pygmy resonance in rare-earth nuclei [4, 5].

In neutron-rich Sn isotopes, as well as in other neutron-rich medium-heavy or heavy nuclei, a small resonance on the tail of the GEDR has been observed. This so-called pygmy resonance has been measured in many experiments using various techniques. At the OCL, this resonance has earlier been measured in ^{117}Sn [6]. This experiment was the first time that the resonance was measured below the neutron-separation energy in an odd, stable Sn nucleus. It was not found that the nucleus has a strongly enhanced strength function for lower energies, which has been seen for some light and medium-heavy nuclei. The level densities of ^{116,117}Sn measured in this experiment, were also interesting because distinctive steps were observed [7]. Some of the steps were interpreted as signatures of neutron pair breaking and were explained by the magic number of protons in Sn ($Z = 50$). Only pair breakings of neutrons occur at low excitation energy. The steps in the level density of ^{116}Sn were the most pronounced steps ever seen in experiments done at the OCL.

The origin of the pygmy resonances in Sn and other nuclei is still unclear. Theoretical models often assume the neutron-skin oscillation mode, where the resonance is created by excess neutrons in a skin collectively oscillating against a $N \approx Z$ core. According to this interpretation, the strength of the resonance should increase with an increasing number of neutrons. Tin is an ideal element for a

systematic resonance study due to the large number of stable isotopes. For this thesis, we have performed experiments on ^{116,118,119,121,122}Sn and extracted their level densities and strength functions. One aim is to investigate the evolution of the pygmy resonance with increasing neutron number. The results are published in Refs. [8, 9], which are included in this thesis as the scientific Articles $1-2$.

Another aim is a thorough review of the Oslo method with the purpose of investigating possible systematic uncertainties. Typical data sets from various mass regions as well as simulated data have been tested against the assumptions behind the data analysis. The study is published in Ref. [10] and is included here as Article 3.

The present thesis starts with chapters providing background information. Chapter 2 presents an overview of the experiments analysed and of the experimental set-ups. Chapter 3 describes the data analysis for extracting the events to proceed with from the measured data. Chapters 4 and 5 go through the Oslo method. The first of these two chapters concerns the preparation of the γ-ray spectra, i.e., the unfolding and the extraction of the first-generation γ rays. The latter presents how the level density and the γ-ray strength function are extracted with the Oslo method. Brief background information about the pygmy resonance is given in Chapter 6. Articles $1-3$ are included in Chapter 7. Chapter 8 summarises the results and draws conclusions.

Chapter 2

Experiments and set-ups

The experiments covered in this thesis were all performed at the OCL, which is located at Centre for Accelerator based Research and Energy Physics (SAFE) at the University of Oslo. The cyclotron was built in 1979 and is Norway's only nuclear physics research cyclotron. It is an MC-35 Scanditronix model, able to deliver pulsed light-ion beams of p, d, ^{3}He and α. The cyclotron is shown in Fig. 2.1. The picture also shows the 90° analysing magnet, used as momentum filter. When the beam reaches the target, its diameter has been focused and collimated to about $1-2$ mm.

In this thesis, three experiments are studied, and experimental data on ^{116}Sn, ^{118,119}Sn and ^{121,122}Sn are analysed. Two nuclear reactions are considered, namely the inelastic scattering reaction (^{3}He,^{3}He$'\gamma$) and the neutron pick-up

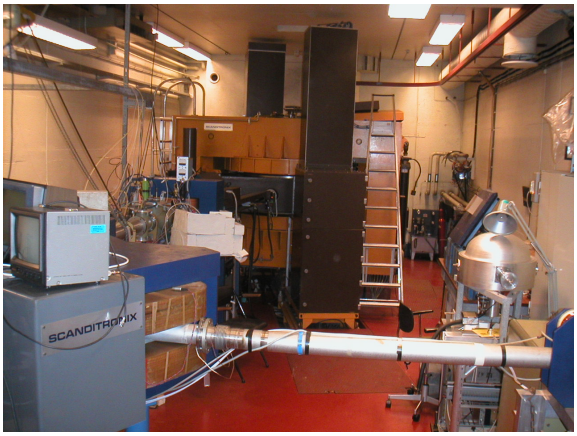

Figure 2.1: The Oslo Cyclotron with the analysing magnet to the left.

Target	Enrichment (%)	Mass thickness (mg/cm^2)	Beam energy (MeV)	Current (nA)	Reactions studied
^{117}Sn	92.0	1.9	38	1.5	^{117}Sn(^{3}He,$\alpha\gamma$)^{116}Sn
^{119}Sn	93.2	1.6	38	1.5	^{119}Sn(^{3}He,^{3}He$'\gamma$)^{119}Sn ^{119}Sn(^{3}He,$\alpha\gamma$)^{118}Sn
^{122}Sn	94	1.4	38	0.2	^{122}Sn(^{3}He,^{3}He$'\gamma$)^{122}Sn ^{122}Sn(^{3}He,$\alpha\gamma$)^{121}Sn

Table 2.1: The enrichment and mass thickness of the targets, the energy and current of the beams, and the reactions studied in the experiments presented in this thesis. The last experiment was performed with the new 64 telescope SiRi system.

reaction (^{3}He,$\alpha\gamma$). The experiment on ^{116}Sn was run for eleven days in 2003, the experiment on ^{118,119}Sn for three days in 2008, and the one on ^{121,122}Sn for five days in 2010. All experiments had beams of ^{3}He with typical pulse frequencies of 15.3 MHz. The technical details of the experiments are listed in Tab. 2.1.

The γ rays and particle ejectiles emitted in the nuclear reactions are measured with NaI(Tl)-scintillation detectors and Si semiconductor detectors, respectively. An illustration of the particle-γ-ray coincidence detection set-up is shown in Fig. 2.2.

The CACTUS γ-ray multidetector system consists of 28 5"$\times$5" NaI(Tl) detectors. CACTUS is described in Ref. [11] and shown in Fig. 2.3. The detectors are distributed on a spherical frame in a distance of 22 cm from the target. At the

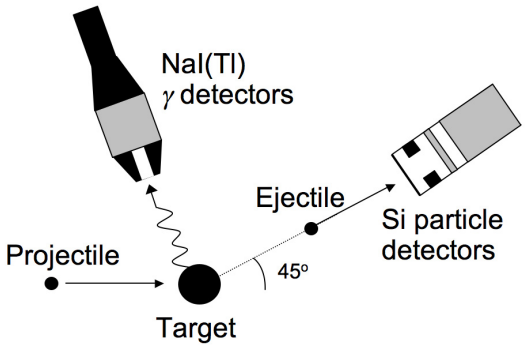

Figure 2.2: Schematic set-up for particle-γ-ray detection. The illustrated particle detector is of the old type, placed in an azimuthal angle of 45° with respect to the beam axis.

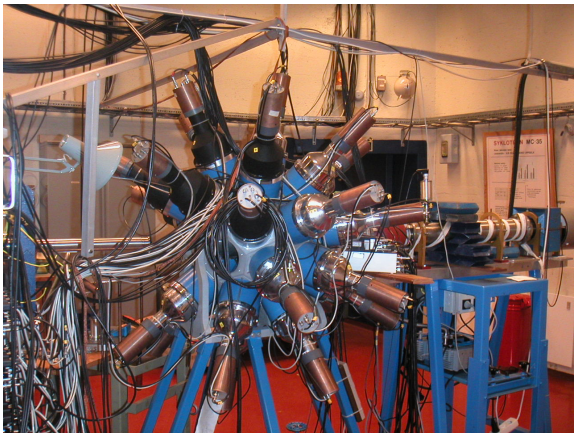

Figure 2.3: The γ-ray multidetector system CACTUS, consisting of 28 NaI(Tl)-scintillation detectors. The target and the particle detectors are placed inside the CACTUS sphere.

γ-ray energy of 1332 keV, CACTUS' total detection efficiency is 15.2%, while the energy resolution of a single detector is $\approx 6\%$ Full Width at Half Maximum (FWHM). The NaI crystals are collimated by lead collimators in order to obtain a good peak-to-total ratio (from reducing the escape out of the NaI crystal of Compton-scattered γ rays). The inner diameter of the collimator is 7 cm. A total solid angle of $\approx 18\%$ out of 4π is covered by the 28 NaI detectors. Copper absorbers of 2 mm thickness in front of each NaI detector reduce the background from X rays.

The target and the Si detector system are located inside the CACTUS sphere. Two different Si detector systems have been used in this thesis, as the old detector system was replaced by SiRi (Silicon Ring) in 2009. They will both be briefly described in the following.

The original particle detector system consisted of eight Si $\Delta E - E$ detectors. The thicknesses of the ΔE detectors were $\sim 140 - 150$ μm, while those of the E detectors were 1500 μm. Aluminium foils of thickness 15 μm were placed in front of each ΔE detector in order to stop the δ electrons, originating from the target foil.

The detectors were distributed on a ring with a distance of 5 cm from the target and having an angle of 45° with respect to the beam axis. This choice of angle is a compromise. Both the elastic scattering reaction and the reactions of interest have their largest cross sections at small scattering angles. A large deflection angle is favourable in order to reduce the dominance from the elastic scattering. On

the other hand, the angle should not be too large, since the rate of the interesting reactions are also reduced when the scattering angle is increased.

The ΔE detectors were collimated to reduce the occurrences of partial detection of the ejectiles' energies on the edge of the active area, and to ensure narrow spreads $\Delta\theta$ of the scattering angles. Since the energy of a scattered particle depends on the scattering angle, a smaller fluctuation in scattering angle leads to smaller spread in the detected energy. Thus, a small collimator leads to a better energy resolution. However, large collimators are favourable from a detection efficiency point of view. The size of the collimator may therefore be adjusted to the target mass. A heavy nucleus causes a smaller spread in the ejectile's energy per $\Delta\theta$ and therefore allows for a larger collimator, compared to a light nucleus.

The first two experiments in this thesis used the old Si detector system. The ^{116,117}Sn experiment had collimators with spherical openings of diameter 6 mm, giving the particle detector system a total solid-angle coverage of $\approx 0.72\%$ out of 4π. In the ^{118,119}Sn experiment, the collimators were shaped as squared openings of 6×10 mm^2, giving a total solid-angle coverage of $\approx 1.5\%$.

The new SiRi particle detector system was used for the last experiment, ^{121,122}Sn. SiRi consists of eight trapeziums distributed on a ring with a fixed angle with respect to the beam axis in a distance of 5 cm from the target, see Fig. 2.4. The ΔE detectors of each trapezium are assigned to individual angles of $40-54^\circ$, as shown in Fig. 2.5.

Each trapezium consists of eight independent ΔE detectors and one common E detector on the back. In total, SiRi has 64 $\Delta E - E$ detectors. The detector thicknesses are 130 μm (ΔE) and 1550 μm (E). A conic Al absorber with a mass thickness of 2.8 mg/cm^2 covers the front of the trapeziums in order to stop δ electrons.

As each tick on the axes in Fig. 2.5 corresponds to 2 mm in reality, each detector is less than 2 mm narrow in the y axis. As the old Si detector system had a 6 mm opening in this direction, SiRi gives an improvement in the energy resolution from less spread in the scattering angle. In addition, there is an improvement in the detection efficiency from a larger total solid-angle coverage, which is $\approx 9\%$ out of 4π.

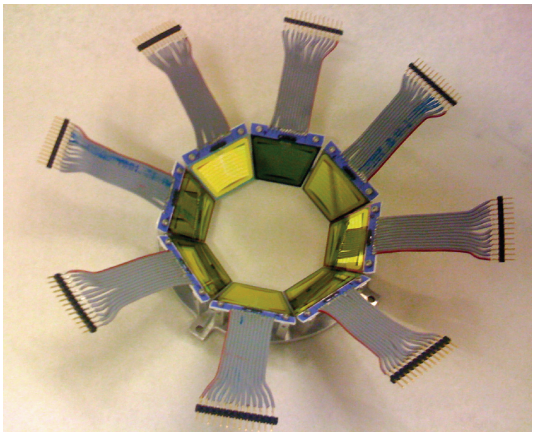

Figure 2.4: SiRi's eight trapeziums distributed on a ring.

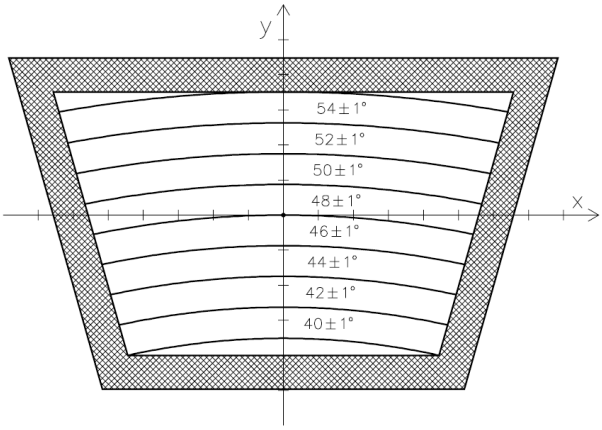

Figure 2.5: The front of one of the SiRi trapeziums, which has eight arch-shaped ΔE detectors. The angular assignments of each of the ΔE detector are indicated in the figure. One tick on the axes corresponds to 2 mm in reality.

Chapter 3

Particle-γ-ray coincidence measurements

The first step of the data analysis is to calibrate and align the detectors and to extract the relevant events, which are the particle-γ-ray coincidences. The method is discussed in this chapter.

3.1 Detector calibration and alignment

Each of the individual detectors of particles and γ-rays were calibrated in energy according to a linear relationship between channel ch and detected energy E':

$$E' = a_0 + a_1 \cdot \mathrm{ch}\,, \tag{3.1}$$

where a_0 is the shift constant and a_1 the dispersion. The appropriate values for a_0 and a_1 were determined for each individual particle/γ-ray detector. Likewise, the detectors were calibrated and aligned in time.

Data from the aligned individual particle detectors were added to one energy spectrum and one time spectrum, and likewise for the γ-ray detectors. Good alignment is important in order to obtain a good energy/time resolution in the total spectra. The FWHM of the elastic ^{3}He peak was determined to ≈ 280 keV at 36.8 MeV in the ^{118,119}Sn experiment, and to ≈ 210 keV at 37.0 MeV in the ^{121,122}Sn experiment. The energy resolution of the total γ-ray spectrum at 1.1 MeV was determined to $\approx 6.4\%$ FWHM in the ^{118,119}Sn experiment, and to $\approx 5.3\%$ FWHM in the ^{121,122}Sn experiment.

3.2 Particle identification

In order to gate on a specific particle, a way to identify the type of charged particles (p, d, t, ^{3}He or α) is needed. Figure 3.1 shows the $\Delta E - E$ matrix for the ^{121,122}Sn experiment. In the $\Delta E - E$ matrix, the particle types are distinguished from their different combination of energy deposits in the ΔE and E detectors.

The energy loss per length, $\mathrm{d}E'/\mathrm{d}x$, in the ΔE detector may be calculated from the Bethe-Block formula, where the leading term is [12]:

$$-\frac{\mathrm{d}E'}{\mathrm{d}x} = C\left(\frac{Z}{v}\right)^2, \tag{3.2}$$

where C is a constant and v the particle's velocity. This expression may be rearranged to explicitly include the particle mass m, if one considers the special case where several particle types having the same kinetic energy E_k:

$$-\frac{\mathrm{d}E'}{\mathrm{d}x} = C\frac{Z^2}{2E_k/m}. \tag{3.3}$$

A change of the particle type will lead to a change in the energy deposit in the ΔE detector, and of course also correspondingly in the E detector. Since the particle types can take a broad range of kinetic energies, the result is the shapes that we see in the $\Delta E - E$ matrix in Fig. 3.1.

Figure 3.1 visualises that the separation in ΔE is larger between different values of Z than of m. There is a large gap between different Z and equal m (t and ^{3}He), and smaller gaps between different m's and equal Z's (e.g., ^{3}He and α).

The so-called thickness spectrum reduces the two-dimensional $\Delta E - E$ matrix to a one-dimensional spectrum. Then a particle type may be identified with a single window. We apply the known range R^α of α particles in Si as a function of energy and define the thickness T as the range of an α particle of energy $E_\mathrm{k} = \Delta E + E$ in Si minus the corresponding range for energy E:

$$T = R^\alpha(E_\mathrm{k}) - R^\alpha(E). \tag{3.4}$$

The thickness T is calculated for all particles detected in the experiment.

The resulting thickness spectrum will consist of one peak for each particle type. The peak that reproduces the actual thickness of the ΔE detector consists of the α particles. The other particle types have smaller m and possibly smaller Z^2 than α particles, and therefore they deposit less energy in the ΔE detector than an α particle with the same kinetic energy do.

Figure 3.2 shows the thickness spectrum for the ^{118,119}Sn experiment. The peak with centroid energy of ≈ 145 μm consists of α particles, while the larger peak at a smaller thickness consists of ^{3}He.

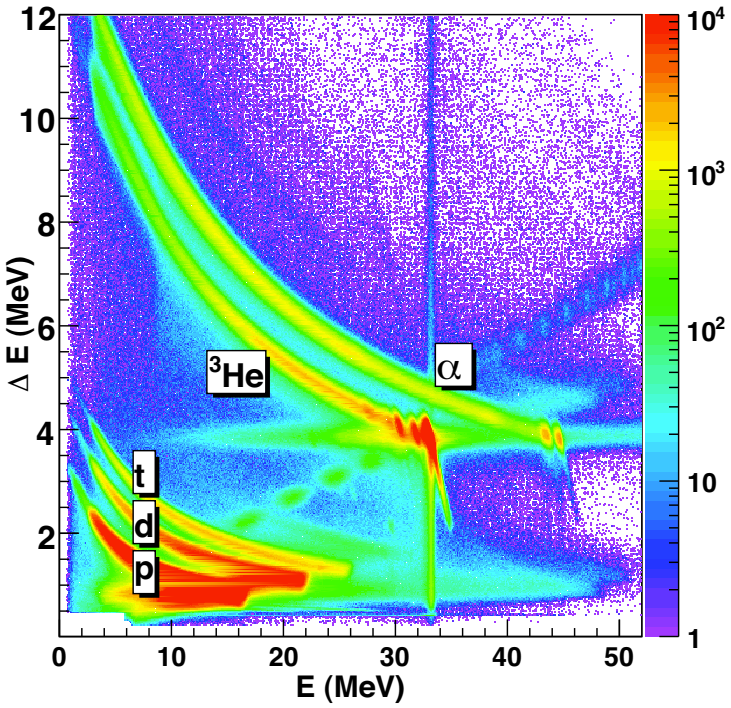

Figure 3.1: Identification of the particle types from the $\Delta E - E$ matrix by the combination of the energy deposits in the ΔE and E detectors. The shown $\Delta E - E$ matrix is from the ^{121,122}Sn experiment.

3.3 Coincidence gating

In order to extract the true particle-γ-ray coincidences, we measure the time difference between detection of good particle events (i.e., both ΔE and E detection) and γ-ray events with 28 time-to-digital converters (TDC). A delay is added to the time signal of the γ ray, so that the detected time difference is a non-zero value. The particle events give the start signals, while the γ-ray events give the stop signals. The time difference is shown in the time spectrum, where the true coincidences are found in the so-called prompt time peak. The TDC measures the entire prompt peak due to the applied delay.

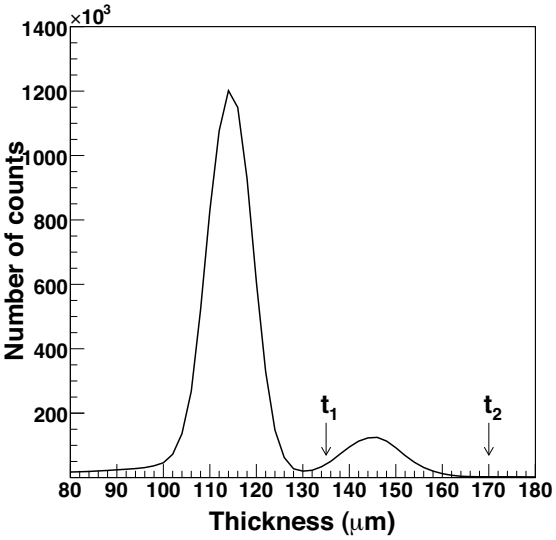

Figure 3.2: The thickness spectrum for one of the ΔE detectors in the ^{118,119}Sn experiment. The peak having a centroid thickness ≈ 145 μm represents the α particles, while the peak at ≈ 115 μm is ^{3}He. The two arrows show the low (t_1) and high (t_2) gates set to extract α particles.

Figure 3.3 shows the time spectrum for the ^{119}Sn(^{3}He,^{3}He$'\gamma$)^{119}Sn reaction. The prompt peak is centered around time difference ≈ 200 ns, which corresponds to the chosen delay. The time resolution, determined from the FWHM of the prompt peak, is ≈ 18 ns.

The smaller peak to the left of the prompt peak consists of random coincidences[1] and is used for background subtraction. Hence for the particle-specific spectrum, gates for incrementation are set on the prompt peak, while gates for decrementation are set on the smaller peak.

[1]The random coincidences in the smaller peak comes from particles from the nuclear reaction of the present beam burst coinciding with background γ rays or γ rays originating from the previous burst, as well as particles from the reaction of the preceding burst coinciding with γ rays from the present burst.

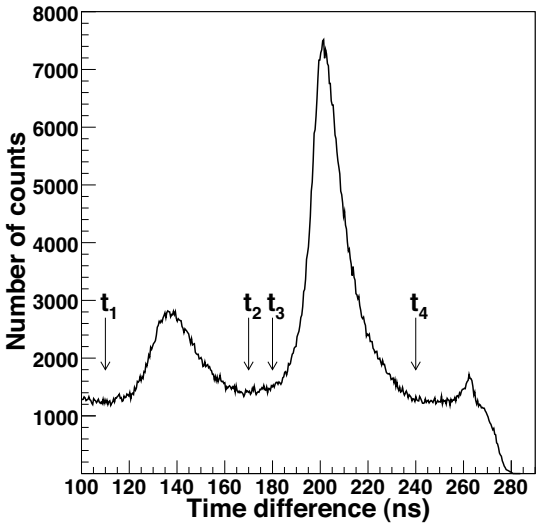

Figure 3.3: The time spectrum for ^{119}Sn(^{3}He,^{3}He′γ)^{119}Sn showing the time difference between detection of ^{3}He particles and γ rays. The two arrows t_1 and t_2 show the gates set on the peak of random coincidences (decrementation), while t_3 and t_4 show the gates set on the prompt peak (incrementation).

3.4 Particle-γ-ray coincidence matrix

After gating on the selected particle type and on the prompt time peak, we are left with the particle-γ-ray coincidence events, where the γ-ray energies are the observed (raw) energy from the NaI detectors. These coincidence events may be arranged in a two-dimensional coincidence matrix $P'(E,E_\gamma)$, which has the observed γ-ray energy E_γ on the x axis and the excitation energy E of the residual nucleus on the y axis.[2] This excitation energy is calculated from the detected energy of the ejectile using reaction kinematics and the Q value of the corresponding nuclear reaction.

The observed ^{3}He-γ-ray coincidence matrix for ^{122}Sn is shown in Fig. 3.4. Several typical features are seen in this matrix. The γ-ray energies are less than or equal to the excitation energy. (There are relatively few exceptions, caused by γ-ray pileups.) The $E = E_\gamma$ diagonal represents first-generation γ rays decaying directly to the nucleus' ground state. The number of counts is dramatically reduced above the neutron separation energy $E = S_n$, which is ≈ 8.8 MeV for

[2]From now on, the physical meaning of the quantity E is excitation energy.

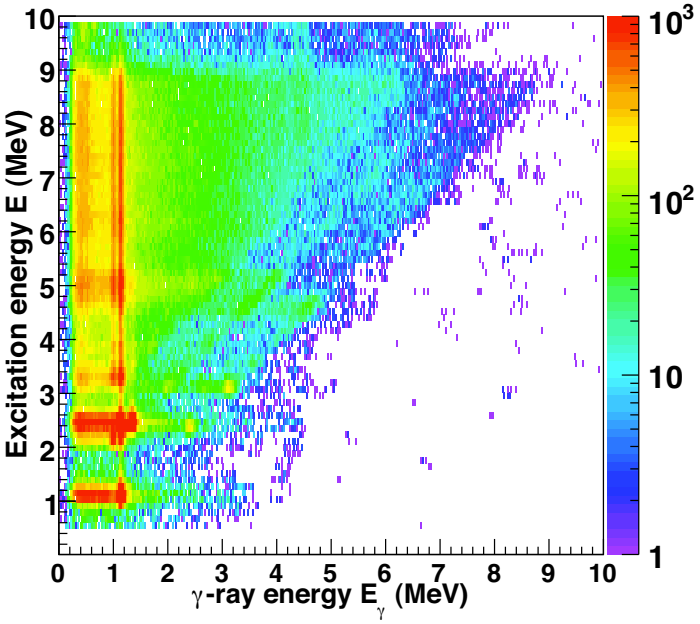

Figure 3.4: The ^{3}He-γ-ray coincidence matrix for ^{122}Sn consisting of the observed γ-ray spectra.

this isotope. This reduction is explained by neutron emission being possible and generally favoured to γ-ray decay above S_n. Some yrast transitions are also displayed in the figure, recognised as strong (red) vertical lines.

Chapter 4

Preparation of the γ-ray spectra

The final part of the data analysis is to apply the Oslo method. The Oslo method consists of four steps to simultaneously extract the experimental level density and the γ-ray strength function from the measured data.

In this chapter, we present how the observed γ-ray spectra are prepared for the simultaneous extraction. Special techniques are used for the unfolding (Sec. 4.1) and for the rejecting of the higher-than-first generation γ rays (Sec. 4.2). These steps are the first two of the Oslo method.

In the next chapter, we will present the last two steps, which are the factorisation from the first-generation coincidence matrix as well as the normalisation of the experimental level density and transmission coefficient.

4.1 Unfolding of the γ-ray spectra

The γ-ray spectra have to be corrected for the response of the NaI detectors. This unfolding (deconvolution) is necessary because the energy deposited in the γ-ray detector is often not equal to the energy of the incident photon. The unfolding of the γ-ray spectra in the Oslo method follows the procedure described in Ref. [11]. The folding iteration method, based on successive foldings of better and better trial functions, is performed first. Afterwards, the Compton subtraction method, developed at the OCL, ensures a large improvement in the reduction of the fluctuations of the unfolded spectra.

The photon interacts with matter mainly in three ways, and their energy dependences are different. Photoelectric absorption gives complete detection and hence, a full-energy peak. This peak does not need correction. The photon may also undergo Compton scattering in the detector while the scattered photon itself escapes. Such cases give rise to the broad Compton background. The third important interaction is the pair production, where the photon may interact with

matter and create an electron-positron pair. The positron will annihilate, and one or two of the annihilation photons may escape detection. If so, the energy detected will be 0.511 or 1.022 MeV less than that of the incoming photon. Also background peaks at 511 keV and at $\sim 200-300$ keV, respectively originating from annihilation radiation and from backscattering outside the detector, are found in the observed spectra.

The objective of the unfolding is to find the actual energy of the incident photons. For this, we need to know the detector's responses as a function of incident γ-ray energy. This may be given in the response matrix $\mathbf{R}(E', E_\gamma)$, where E' is the energy deposited in the NaI detector and E_γ the energy of the incident photon. The response matrix is used to deduce the full-energy spectra from the observed spectra.

4.1.1 Determining the response functions

The response function of the CACTUS detector has been determined by performing experiments and measuring the detector's response function for a wide range of monoenergetic γ-ray energies. Of practical reasons, this has been done for a series of ten energies (122, 245, 344, 662, 1173, 1333, 1836, 4439, 6130 and 15110 keV), while all energies in between have been interpolated.

The interpolation is done separately for the different structures in the spectra. The full-energy peak is easily interpolated. The Compton background, however, needs a more complicated treatment, since the energy region of the Compton background depends on the respective full energy. The energy E'' transferred to the electron in a Compton process is given by

$$E'' = E_\gamma - \frac{E_\gamma}{1 + \frac{E_\gamma}{m_e c^2}(1 - \cos\theta)}, \tag{4.1}$$

where θ is the scattering angle between the directions of the incident and scattered photons, and m_e is the mass of the electron. The maximum transferred energy, the Compton edge, is found at $\theta = 180^\circ$. A reasonable procedure is to interpolate for each spectrum the response functions of the Compton background at energies corresponding to the same values of θ. The interpolation then operates along a set of curves forming a fan, as illustrated in Fig. 4.1.

The set of interpolated response functions make the response matrix $\mathbf{R}(E', E_\gamma)$. More information about the method of determining CACTUS' response matrix is found in Ref. [11].

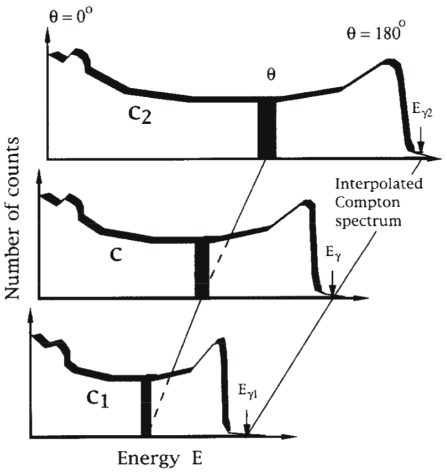

Figure 4.1: Interpolation of the response functions C_2, C and C_1 of the Compton background for different incident γ-ray energies ($E_{\gamma 2}$, E_γ and $E_{\gamma 1}$). The response functions are shown as spectra with energy E'' transferred to the electron on the x axis and the number of counts on the y axis. The figure illustrates how the energy region of the Compton background and the $\Delta\theta$ increase with increasing full energy E_γ. The interpolation of the three Compton response functions are performed at the same angle θ (left diagonal line). The simple interpolation of the full energies is also shown (right diagonal line). The drawing is taken from Ref. [11].

4.1.2 The folding iteration method

The Oslo method unfolds by an iterative procedure, called the difference approach. The procedure was first described in less available institute reports and is therefore also outlined in Ref. [11]. Utilising the response matrix to perform a folding is very straightforward, while inverting the response matrix in order to unfold would cause large fluctuations due to the limited number of events. The idea therefore is to unfold by applying the folding matrix. We start with a trial function which we fold (using the known CACTUS response matrix), modify and refold in an iteration process until the folded redefined trial function is equal to the observed (raw) spectrum. When the spectrum folded equals the observed spectrum, the unfolded spectrum has been found.

The matrix element R_{ij} of the response matrix is defined as the response in channel i when the detector is hit by γ rays with an energy corresponding to channel j. The response function is normalised so that for each incident γ ray in channel j, we have $\sum_i R_{ij} = 1$. The folding of an unfolded spectrum u is then

expressed as:

$$f = \mathbf{R}u\,, \tag{4.2}$$

where f is the folded spectrum.

The folding iteration is performed as following:

1. A trial function u^0 for the unfolded spectrum is assumed, with the same shape as the observed spectrum r:

$$u^0 = r\,. \tag{4.3}$$

2. The first folded spectrum is calculated:

$$f^0 = \mathbf{R}u^0\,. \tag{4.4}$$

3. The resulting folded spectrum is compared to the observed spectrum, and the deviation is $f^0 - r$. The second trial function is the folded spectrum minus this deviation:

$$u^1 = u^0 - (f^0 - r)\,. \tag{4.5}$$

4. The second folding gives the second folded spectrum:

$$f^1 = \mathbf{R}u^1\,, \tag{4.6}$$

which again is used to obtain the next trial function:

$$u^2 = u^1 - (f^1 - r)\,. \tag{4.7}$$

5. The iteration is continued until $f^i \sim r$, where i is the iteration index.

More details about the iteration process are found in Ref. [11].

The folding iteration by the difference approach is a well-proven method giving reliable results. The disadvantage is the relatively large fluctuations from channel to channel in the unfolded spectrum. Because these fluctuations increase with the number of iterations, it is important to terminate the iteration as soon as the folded spectrum agrees with the observed spectrum within the experimental uncertainties. Typically, ten iterations are sufficient.

4.1.3 The Compton subtraction method

The fluctuations in the folded spectrum is in the Oslo method mended by the Compton subtraction method, developed in Ref. [11]. The idea is that since the Compton background is a slowly varying function of energy, the Compton part of the resulting unfolded spectrum u^i can be smoothed and subtracted from the observed spectrum. The result is an unfolded spectrum with the same statistical fluctuations as the observed spectrum.

The starting spectrum of the Compton subtraction method is the unfolded spectrum u^i resulting from the iteration process, which we rename u_0. The probabilities for an event in channel i in the unfolded spectrum u_0 to be found in the full-energy peak is denoted $p_{\rm f}(i)$, in the single escape peak denoted $p_{\rm s}(i)$, in the double escape peak denoted $p_{\rm d}(i)$, and in the annihilation peak denoted $p_{\rm a}(i)$. These probabilities are known as functions of energy as they are parts of the detector's responses. The probabilities are normalised so that:

$$\sum_i p_{\rm f}(i) + p_{\rm s}(i) + p_{\rm d}(i) + p_{\rm a}(i) + p_{\rm c}(i) = 1\,, \tag{4.8}$$

where $p_{\rm c}(i)$ is the probability for having a Compton event (as well as background events, etc.) in channel i.

The probability functions are used for folding. Assume that i is the specific channel i denoting the full-energy peak, and that the channels i_{511} and i_{1022} represent channels with energies 511 and 1022 keV, respectively. The *expected* (folded) contribution to the observed spectrum from the peaks of full energy ($u_{\rm f}$), single escape ($u_{\rm s}$), double escape ($u_{\rm d}$) and annihilation ($u_{\rm a}$) are found from:

$$u_{\rm f}(i) = p_{\rm f}(i)u_0(i)\,, \tag{4.9}$$

$$u_{\rm s}(i-i_{511}) = p_{\rm s}(i)u_0(i)\,, \tag{4.10}$$

$$u_{\rm d}(i-i_{1022}) = p_{\rm d}(i)u_0(i)\,, \tag{4.11}$$

$$u_{\rm a}(i_{511}) = \sum_i p_{\rm a}(i)u_0(i)\,. \tag{4.12}$$

The sum over i for u_a is explained by the fact that all γ-ray energies above 1022 keV will contribute to the peak at 511 keV.

The expected contributions from Eqs. (4.9) − (4.12) have large fluctuations due to the iteration process. Therefore, the expected contributions are smoothed to the observed experimental resolution, which is 1.0 FWHM. The smoothed spectra are denoted $\widetilde{u}_{\rm f}$, $\widetilde{u}_{\rm s}$, $\widetilde{u}_{\rm d}$, and $\widetilde{u}_{\rm a}$, etc.

Now we have a good estimate for the contributions to the observed spectrum from the full energy, single escape, and double escape processes. The expected contribution from the Compton background $c(i)$ may hence be calculated from:

$$c(i) = r(i) - \widetilde{u}_{\rm f}(i) - \widetilde{u}_{\rm s}(i-i_{511}) - \widetilde{u}_{\rm d}(i-i_{1022}) - \widetilde{u}_{\rm a}(i_{511})\,. \tag{4.13}$$

The expected contribution $c(i)$ has strong fluctuations because it is found from the unfolded spectrum u_0. It is expected that the Compton contribution is a slowly varying function of energy. Thus, a smoothing of, e.g., a resolution of 1.0 FWHM, is applied on c to get the smoothed contribution $\widetilde{c}$.

The final unfolded spectrum of the full-energy peaks only is obtained by taking the observed spectrum and subtract the smoothed expected contribution from the Compton background as well as the expected contributions from the single escape, double escape, and the annihilation:

$$u_{\mathrm{unf}}(i) = r(i) - \widetilde{c} - \widetilde{u}_{\mathrm{s}}(i - i_{511}) - \widetilde{u}_{\mathrm{d}}(i - i_{1022}) - \widetilde{u}_{\mathrm{a}}(i_{511})\,. \tag{4.14}$$

Finally, the true unfolded γ-ray energy distribution U_{unf} is calculated by correcting for the full-energy probability $p_{\mathrm{f}}(i)$ and the energy dependent total γ-ray detection efficiency ε of the detector:

$$U_{\mathrm{unf}}(i) = \frac{u_{\mathrm{unf}}(i)}{p_{\mathrm{f}}(i)\varepsilon_{\mathrm{tot}}(i)} \tag{4.15}$$

See Ref. [11] for more details on the Compton subtraction method.

Figure 4.2 shows comparison of the observed γ-ray spectrum, the unfolded spectrum, and the unfolded spectrum refolded, in the case of ^{121}Sn for a chosen excitation energy interval (see figure text). The background is clearly removed in the unfolded spectrum, and only the full-energy peaks are left. Refolding the unfolded spectrum returns a spectrum that is very equal to the observed spectrum.

4.2 Extraction of the first-generation γ rays

The Oslo method uses the first-generation method to extract the first-generation γ rays from the spectra. This method is an in-house developed procedure described in Ref. [13]. We will give an introduction to its main features.

The deexcitation of a highly excited state below the particle threshold may involve a cascade of transitions. Each transition will result in the emission of a γ ray. The transition probability depends on the γ-ray energy and the final level density. In order to extract the γ-ray strength function, we therefore also need to know which γ rays decay to which levels. This is done by considering only the first-generation γ ray of each transition, since then, the final excitation energy is known from an easy calculation from the initial state and the γ-ray energy.

The time resolution of the experiment is not in any way able to separate out the first-generation γ rays. A γ decay in the quasi continuum is very fast, typically $\sim 10^{-15}$ s for the entire process. In the analysis, it therefore seems like all the γ rays in a decay occur at the same time. The generations of the γ rays are also not

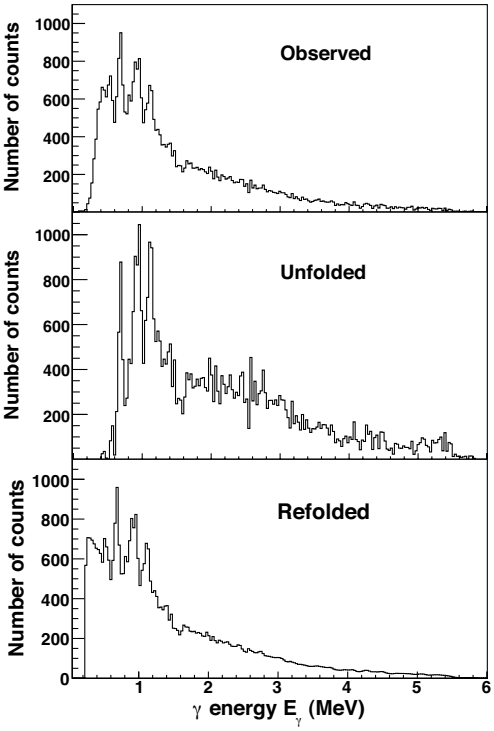

Figure 4.2: Comparison of the observed γ-ray spectrum (upper panel), the unfolded spectrum (middle panel), and the unfolded spectrum refolded (lower panel) for ^{121}Sn. The spectra are shown for excitation energies E in the region $4.5 - 5.6$ MeV.

well separated in energy either, so that discriminating on the energy is no option. The first-generation γ rays must be extracted in another way in the data analysis. This is the motivation for the first-generation method.

4.2.1 Simple example

The main assumption of the first-generation method is that the γ-ray decay from any excitation-energy bin is independent of how the nucleus was excited to this bin. In other words, that the decay routes are the same whether they were initiated directly by the nuclear reaction or by the feeding from γ-ray decay from

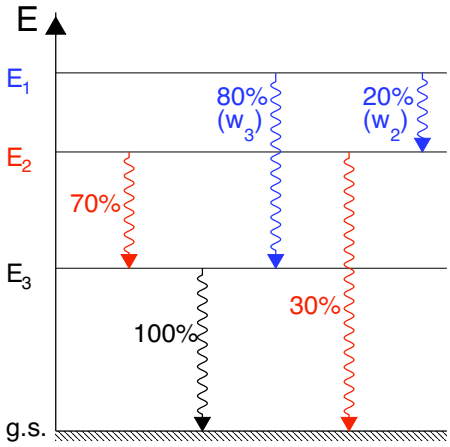

Figure 4.3: A hypothetical decay route from energy level E_1. First-generation γ rays are coloured in blue, second-generation in red, and third-generation in black. The branching ratio w_2 is the probability of decay from level E_1 to E_2, while w_3 is the probability of decay from E_1 to E_3.

higher-lying states. In the following simple example, we will see in what way the main assumption of the first-generation method is introduced.

Figure 4.3 shows a hypothetical decay route from the discrete excitation-energy level E_1, where the γ rays may decay to lower-lying levels E_2 and E_3 with decay-route branching ratios w_2 and w_3, respectively. We assume for simplicity that all energy levels are equally populated. Let us give the name f_1 to the total (all-generations) γ-ray spectrum from E_1, f_2 to the total spectrum from E_2, and f_3 to the total spectrum from E_3. With the above-mentioned assumption that a state populated by the first γ transition has the same decay properties as if it had been populated directly by the nuclear reaction, the second and third generation γ rays originating from E_1 is accessed from f_2 and f_3 multiplied with their respective branching ratios. Hence, the first-generation γ-ray spectrum h from E_1 is in this simple example found by:

$$h = f_1 - w_2 f_2 - w_3 f_3 \,. \tag{4.16}$$

The reaction cross section instead varies from level to level, leading to different population of the levels. To compensate, we therefore introduce the corresponding weighting of the spectra. The normalisation factor n_2 between level

E_1 and level E_2 is:

$$n_2 = \frac{S_1}{S_2}\,, \tag{4.17}$$

where S_1 is the population of level E_1, etc. A similar definition is done for n_3. Hence, taking the varying population of the levels into account, the first-generation γ-ray spectrum h from E_1 is found by:

$$h = f_1 - n_2 w_2 f_2 - n_3 w_3 f_3\,. \tag{4.18}$$

4.2.2 Technical details of the first-generation method

We would like to write a general expression for the first-generation spectrum from an excitation energy bin, but keep the consideration to only the highest energy bin (bin 1) for simplified notation. The results may easily be generalised to any lower-lying energy bin j. We recall the assumption of the first-generation method: The decay route of a state is the same whether the state has been populated directly by the nuclear reaction of by γ decay from higher-lying states, i.e., independence of the method of formation.

The first-generation γ-ray spectrum of bin 1, h, is found from:

$$h = f_1 - g\,, \tag{4.19}$$

where f_1 is the total spectrum of bin 1, and where g is the weighted sum of all the spectra:

$$g = \sum_i n_i w_i f_i\,. \tag{4.20}$$

In this sum, the coefficients w_i (normalised to $\sum_i w_i = 1$) are the (unknown) probabilities of γ decay (branching ratios) from bin 1 to an underlying bin i. The coefficients n_i are the normalising factors for the differences in the cross sections for populating bin 1 and the underlying bins i. The subtraction of g in Eq. (4.19), as defined by w_i and n_i in Eq. (4.20), equals the assumption that the decay routes are independent of the method of formation.

There are two ways to determine n_i: The *singles normalisation* and the *multiplicity normalisation*. Their major difference is the use of single particle counts in the first case, and of the number of γ rays in each spectrum f_i in the latter.

- Singles normalisation: The cross-section correction factor n_i is determined from the ratio of singles particle counts (populations) S in energy bin 1 and bin i:

$$n_i = \frac{S_1}{S_i}\,. \tag{4.21}$$

- Multiplicity normalisation: The deexcitation of a state at energy level E_i will lead to a cascade of γ rays with average multiplicity M_i. The number of particle populations may in general be found from dividing the number of γ rays by the multiplicity. Hence, the population of energy bin i, S_i, is proportional to $A(f_i)/M_i$, where $A(f_i)$ is the number of counts (area) of the γ-ray spectrum f_i. Hence, the cross-section correction factor n_i may be determined from:

$$n_i = \frac{A(f_1)/M_1}{A(f_i)/M_i} = \frac{A(f_1)M_i}{A(f_i)M_1}. \tag{4.22}$$

  The average multiplicity as a function of excitation energy may easily be deduced from the experiment.

The two normalisation methods may give different results due to presence of isomeric states. The γ rays of possible isomeric states may not be considered in the multiplicity normalisation, if their decay time exceed the TDC time range. However in singles normalisation, the isomeric states will be taken into account, but not their γ rays. In such a case, the singles normalisation will lead to stronger subtraction than the multiplicity normalisation. Usually, the difference between singles and multiplicity normalisation is very small, and both methods are performed and compared when analysing an experiment. Multiplicity normalisation was chosen for all the Sn experiments in this thesis.

Because the unknown weighting coefficients w_i correspond directly to the first-generation spectrum h, the w_i's are found from a fast converging iteration procedure [13]:

1. Assume a trial function w_i.
2. Deduce h.
3. Transform h to w_i by giving h the same energy calibration as w_i and by normalising the area to unity.
4. Repeat from step 2 until w_i (new) $\approx w_i$ (old). Then, convergence has been reached, and the procedure is finished.

Tests have shown that the first-generation method gives very correct results with small dependence on the choice of trial function after only three iterations [13]. Usually, at least ten iterations are performed.

Figure 4.4 shows the total, the higher-than-first-generation and the first-generation γ-ray spectra for a chosen excitation energy region in ^{121}Sn.

The first-generation γ-ray spectra are arranged in a two-dimensional matrix $P(E, E_\gamma)$. This matrix is normalised for every excitation-energy bin E so that the

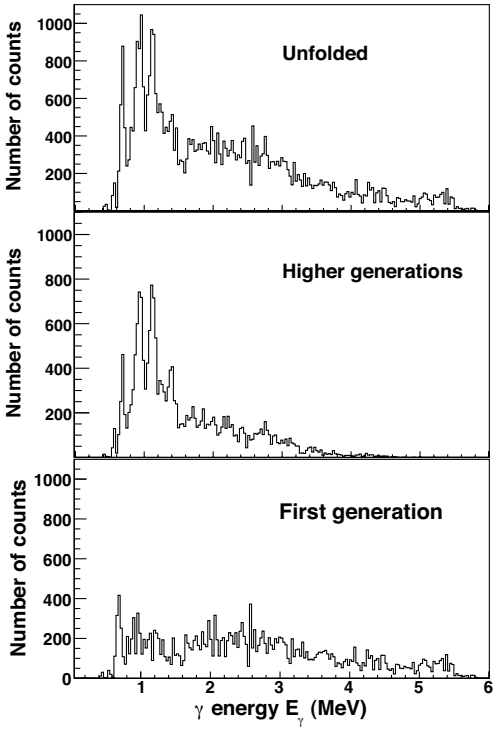

Figure 4.4: Comparison of the total (unfolded) γ-ray spectrum (upper panel), the higher-than-first-generation spectrum (middle panel), and the first-generation spectrum (lower panel) for ^{121}Sn. The spectra are shown for excitation energies in the region $4.5-5.6$ MeV.

sum over all γ-ray energies E_γ from some minimum value ${E_\gamma}^{\min}$ to its maximum value ${E_\gamma}^{\max} = E$ at this excitation-energy bin is unity:

$$\sum_{E_\gamma={E_\gamma}^{\min}}^{E} P(E,E_\gamma) = 1\,. \tag{4.23}$$

In this way, its entries are the relative γ-decay probabilities, i.e. the probability that a γ ray of energy E_γ is emitted from an excitation-energy bin E.

The P matrix is shown for ^{122}Sn in Fig. 4.5. There are regions in this matrix for which the first-generation method has not worked very well. The empty region

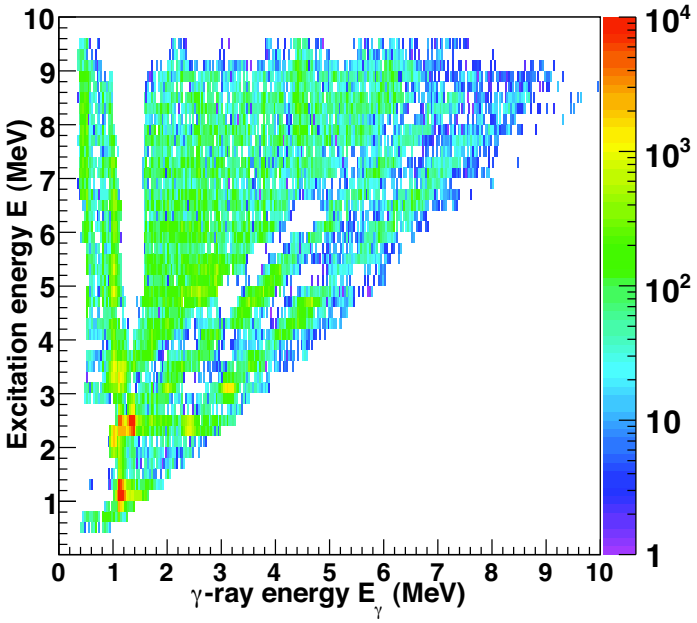

Figure 4.5: First-generation matrix $P(E, E_\gamma)$ of ^{122}Sn.

at lower γ-ray energies and higher excitation energies is explained by differences in shape of the γ-ray spectra between lower and higher excitation energies, caused by differences in the feeding of the states from the nuclear reaction and from the decay from higher-lying states (non-independence of method of formation). The differences in shape may be understood by, e.g., the two strongly populated states at lower excitation energy (visualised as the two red spots), causing too strong subtraction. The shortcoming of the method is eliminated by excluding this region of low γ-ray energy in the further analysis. Article 3 elaborates on this kind of shortcoming.

Chapter 5

Extraction of the level density and the γ-ray strength function

The present chapter concerns the last two parts of the Oslo method: The factorising of the experimental first-generation matrix $P(E,E_\gamma)$ into the unnormalised level density $\rho(E)$ and γ-ray transmission coefficient $\mathscr{T}(E_\gamma)$ (Sec. 5.1), as well as their normalisation (Sec. 5.2). Afterwards, the γ-ray strength function $f(E_\gamma)$ may easily be estimated from the transmission coefficient (Sec. 5.3).

5.1 Factorisation of level density and transmission coefficient

A method of simultaneous extraction of the experimental level density $\rho(E)$ and γ-ray strength function $f(E_\gamma)$ has been developed at the OCL [14]. The method uses the first-generation matrix $P(E,E_\gamma)$ as the basis, as well as the assumption that the γ decay is statistical. We will present the main features of the factorisation method.

The general rule describing the transition probability per time between energy levels in a quantum system is the well-known Fermi's golden rule:

$$\lambda = \frac{2\pi}{\hbar}|\langle f|\widehat{H}_{\rm int}|i\rangle|^2\rho(E_{\rm f})\,. \tag{5.1}$$

Here λ is the transition probability per time (transition rate) of the initial state $|i\rangle$ to the final state $|f\rangle$. The quantity $\widehat{H}_{\rm int}$ is the perturbating transition operator, and $\rho(E_{\rm f})$ is the level density at the final excitation energy $E_{\rm f} = E - E_\gamma$. As we see from Eq. (5.1), the transition rate is proportional to both the square of the absolute

value of the matrix element of perturbation and to the level density at the final excitation energy E_f.

The Brink-Axel hypothesis [15, 16] states that collective excitation modes built on excited states have the same decay properties as those built on the ground state. In other words, we assume that the γ-ray transmission coefficient $\mathscr{T}(E_\gamma)$ is only a function of γ-ray energy and independent of excitation energy E (and thus the nuclear temperature).

The Brink-Axel hypothesis is assumed to be valid for statistical γ decay (except for very high temperatures and/or spins, beyond those achievable at OCL). Statistical γ decay is the decay from a compound nucleus. A compound nucleus is a nucleus that has thermalised prior to deexcitation, and thus its energy is shared on a relatively large number of nucleons. As a consequence, the nucleus "forgets" its way of formation, and hence, the decay is statistical. In this case, the probability of γ decay $P(E,E_\gamma)$ may be expressed as:

$$P(E,E_\gamma) \propto \mathscr{T}(E_\gamma)\rho(E_f)\,. \tag{5.2}$$

The reactions that we study, (^{3}He,^{3}He$'\gamma$) and (^{3}He,$\alpha\gamma$), are not compound reactions, but direct reactions involving only a few nucleons in the nucleus. Still, in the region of high level density, which usually means levels at high excitation energy, the nucleus seems to attain a compound-like system before deexcitation. This is due to two factors. First, a large degree of configuration mixing appears at high level density [17]. Second, the typical life time of states in the quasi continuum ($\sim 10^{-15}$ s) is many orders of magnitude larger than the time required to create a compound state ($\sim 10^{-18}$ s). However, we do not have compound states in the discrete excitation energy region. Therefore, this low-energy region is not used in the factorisation procedure.

To extract the level density and the γ-ray transmission coefficient, an iterative χ^2 procedure [14] is applied to the first-generation γ-ray matrix $P(E,E_\gamma)$. The basic idea is to globally minimise χ^2:

$$\chi^2 = \frac{1}{N_{\text{free}}} \sum_{E=E^{\min}}^{E} \sum_{E_\gamma=E_\gamma{}^{\min}}^{E} \left(\frac{P_{\text{fit}}(E,E_\gamma) - P(E,E_\gamma)}{\Delta P(E,E_\gamma)} \right)^2 , \tag{5.3}$$

where N_{free} is the number of degrees of freedom, $P(E,E_\gamma)$ is the experimental first-generation matrix, $\Delta P(E,E_\gamma)$ is the uncertainty in the experimental $P(E,E_\gamma)$ matrix, and $P_{\text{fit}}(E,E_\gamma)$ is the χ^2-fitted output matrix from the iteration. This output is fitted as a normalised product of the level density and the transmission coefficient:

$$P_{\text{fit}}(E,E_\gamma) = \frac{\rho(E-E_\gamma)\mathscr{T}(E_\gamma)}{\sum_{E_\gamma=E_\gamma{}^{\min}}^{E} \rho(E-E_\gamma)\mathscr{T}(E_\gamma)}\,. \tag{5.4}$$

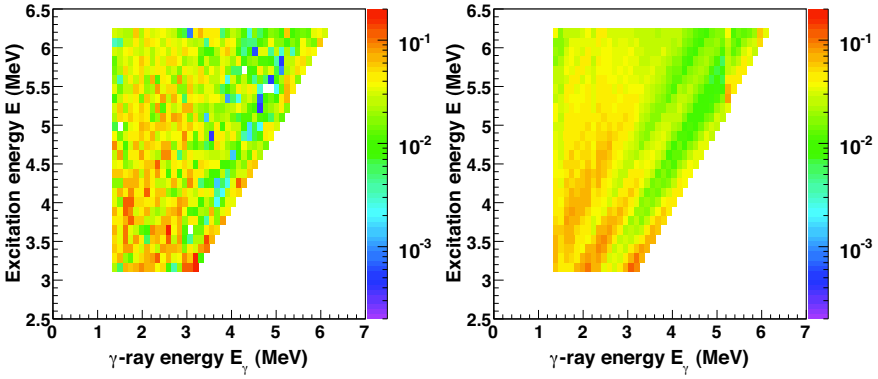

Figure 5.1: First-generation matrixes of ^{121}Sn. The left panel shows the experimental matrix $P(E,E_\gamma)$, while the right panel shows the output matrix $P_{\rm fit}(E,E_\gamma)$ calculated from χ^2 fitting. The cuts of data illustrate the limits that were set prior to the extraction. The energy bins of E_γ and E are 120 keV/ch.

The denominator of the expression assures that $P_{\rm fit}$ is normalised to unity.

Every points of the $\rho(E-E_\gamma)$ and $\mathscr{T}(E_\gamma)$ functions are assumed to be independent variables, so that χ^2 in Eq. (5.3) is minimised for every argument $E-E_\gamma$ and for E_γ. When a certain matrix $P_{\rm fit}$ minimises χ^2, the two independent functions $\rho(E-E_\gamma)$ and $\mathscr{T}(E_\gamma)$ have been found. The method usually converges very well [14].

Figure 5.1 shows for ^{121}Sn the input (experimental) matrix $P(E,E_\gamma)$ in the left panel and the output (χ^2-fitted) matrix $P_{\rm fit}(E,E_\gamma)$ in the right. These limits set prior to the extraction procedure were chosen to ensure that the data used in the iteration method are from the statistical excitation-energy region $(E^{\rm min},E^{\rm max})$, and that the γ-ray energies are above a certain threshold where the first-generation method works well ($E_\gamma{}^{\rm min}$) (see Sec. 4.2.2).

The quality of the procedure when applied to the measurements on ^{122}Sn is demonstrated in Fig. 5.2. The experimental first-generation spectra (filled squares) for various excitation energies are compared to the χ^2-fitted solution (solid lines). In general, the agreement between the experimental data and the fit is very good. It is noted that in some of the panels (e.g., the transition to the ground state for the panel of $E=4.1$ MeV, and to the first-excited state for the panel of $E=4.8$ MeV), the fitted curves are significantly lower than the experimental data. This discrepancy is discussed in Article 2.

The globalised fitting to the experimental points gives only the functional

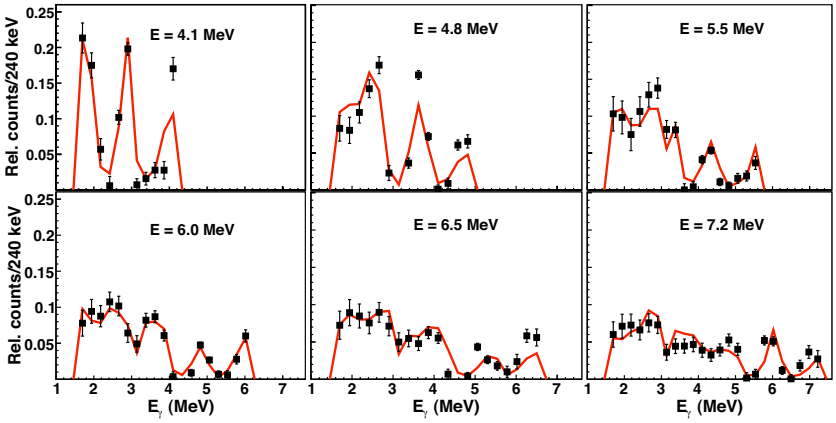

Figure 5.2: Comparison of the experimental P matrix with the χ^2-fitted P_{fit} matrix for ^{122}Sn. Gamma-ray spectra are shown for different excitation energies E, with experimental data as filled squares and χ^2-fitted data as solid lines. The energy bins are compressed to 240 keV/ch in E and in E_γ. While the illustrations have been made for different excitation energies E (indicated in the panels), the χ^2 fit was performed simultaneously for all excitation energies within the chosen region.

forms of ρ and $\mathscr{T}$. It has been shown [14] that if one solution for the set of functions ρ and $\mathscr{T}$ is known, one may construct an infinite number of other sets that give identical fits to the experimental $P(E,E_\gamma)$ matrix:

$$\tilde{\rho}(E-E_\gamma) = A\exp\left[\alpha(E-E_\gamma)\right]\rho(E-E_\gamma), \quad (5.5)$$

$$\tilde{\mathscr{T}}(E_\gamma) = B\exp(\alpha E_\gamma)\mathscr{T}(E_\gamma). \quad (5.6)$$

The parameters A, B, and α are determined so that the functions ρ and $\mathscr{T}$ correspond to the physical solution. This normalisation is treated in the next section.

5.2 Normalisation

The final step for extracting the level density ρ and the γ-ray transmission coefficient $\mathscr{T}$ is the determination of the parameters A, B, and α (see Eqs. (5.5) – (5.6)) that correspond to the physical solution. This is done by comparing these extracted functional forms of ρ and $\mathscr{T}$ to known, experimental data. The details of this normalisation procedure is briefly explained in the following.

5.2.1 Level density

The normalisation procedure for the level density was developed in Ref. [14]. In the discrete excitation-energy region, typically up to $\approx 2-3$ MeV in heavy nuclei like Sn, the level density function is known from spectroscopy. At the neutron separation energy S_n, we can deduce the level density from the level spacing D, obtained from neutron (or proton) resonance experiments, if available. For simplicity, we show it here only for s-wave neutrons (D_0, denoting $\ell = 0$).

The level spacing D_0 is found from neutron resonance experiments using neutrons with spin/parity $1/2^+$. Then levels with spin $I = I_t \pm 1/2$, where I_t is the target spin, are accessible. The s-wave level spacing is

$$D_0 = \frac{1}{\rho(S_n, I_t \pm 1/2, \pi_t)}, \tag{5.7}$$

where π_t is the target parity. Assuming that both parities contribute equally to the level density at the neutron separation energy S_n, the value of D_0 may be determined from:

$$\frac{1}{D_0} = \frac{1}{2}\left[\rho(S_n, I_t + 1/2) + \rho(S_n, I_t - 1/2)\right]. \tag{5.8}$$

We are interested in expressing D_0 as a function of the total (all spins) $\rho(S_n)$. To establish an expression for the value of $\rho(S_n)$, it is necessary to assume models for the spin distribution $g(U,I)$ and the spin cut-off parameter $\sigma(U)$, where U is the nucleus' intrinsic excitation energy. In all the studies on Sn isotopes presented in this thesis, the back-shifted Fermi-gas (BSFG) model with the original parametrization of von Egidy *et al.* [18] was the most appropriate. Here, the spin distribution g and the spin cut-off parameter σ are kept as the original Gilbert and Cameron expressions [19], but with a redefined parameterisation of U and the level-density parameter a (see also Article 1).

The theoretical Fermi-gas prediction for level density $\rho(U)$ as a function of intrinsic excitation energy U for all spins and both parities is [19]:

$$\rho(U) = \frac{\sqrt{\pi}}{12}\frac{\exp(2\sqrt{aU})}{a^{1/4}U^{5/4}}\frac{1}{\sqrt{2\pi}\sigma}, \tag{5.9}$$

while the spin distribution is [19]:

$$g(U,I) = \frac{2I+1}{2\sigma^2}\exp\left[-(I+1/2)^2/2\sigma^2\right]. \tag{5.10}$$

The spin distribution is normalised to $\sum_I g(U,I) \approx 1$. Hence, the theoretical prediction for level density as a function of U and spin I for both parities is found

from:

$$\begin{aligned}\rho(U,I) &= \rho(U)g(U,I) \\ &= \frac{\sqrt{\pi}}{12}\frac{\exp(2\sqrt{aU})}{a^{1/4}U^{5/4}}\frac{(2I+1)\exp\left[-(I+1/2)^2/2\sigma^2\right]}{2\sqrt{2\pi}\sigma^3}. \end{aligned} \quad (5.11)$$

Determining $\rho(S_n, I_t \pm 1/2)$ from the expression in Eq. (5.11) and inserting these into Eq. (5.8), we may express the total level density $\rho(S_n)$ as a function of D_0:

$$\rho(S_n) = \frac{2\sigma^2}{D_0}\frac{1}{(I_t+1)\exp\left[-(I_t+1)^2/2\sigma^2\right] + I_t\exp\left[-{I_t}^2/2\sigma^2\right]}. \quad (5.12)$$

The value of the spin cut-off parameter at the neutron separation energy, $\sigma(S_n)$, according to the chosen parameterisation of Ref. [18] is inserted into Eq. (5.12). Hence, the normalisation value $\rho(S_n)$ has been found, expressed by D_0. The experimental value of D_0 is often available in literature.

While we would like to normalise to $\rho(S_n)$, our experimental results do not reach $E = S_n$, due to methodical limitations. We therefore make an interpolation from $\rho(S_n)$ down to our data points, and instead, we normalise our measurements to this interpolation. The interpolation is made using the level density prediction in Eq. (5.9), where we keep the shape but scale it to agree with $\rho(S_n)$. Figure 5.3 shows the normalised level density function for ^{121}Sn. Included in the figure is also the normalisation value $\rho(S_n)$ and arrows showing the regions of normalisation, both to the discrete levels from spectroscopy and to the level density interpolation from $\rho(S_n)$.

Since $\rho(S_n)$ includes all spins, while we only measure for low spins in the experiments, normalising our measurements to $\rho(S_n)$ also normalise the measured data into all spins. It is assumed that the structures of the level density is approximately the same in a region of low spins compared to if all spins were included (see Article 3).

5.2.2 Transmission coefficient

The log-scale slope of the γ-ray transmission coefficient $\mathscr{T}$ has already been normalised with the correction parameter α. It remains to normalise the absolute value, i.e., finding the absolute value correction B, defined in Eq. (5.6). The normalisation method was developed in Ref. [20] and is briefly explained here.

The γ-ray transmission coefficient is related to the average total radiative width $\left\langle \Gamma_\gamma(E, I_\mathrm{i}, \pi_\mathrm{i}) \right\rangle$ of excitation energy levels with initial energy E, initial spin I_i and

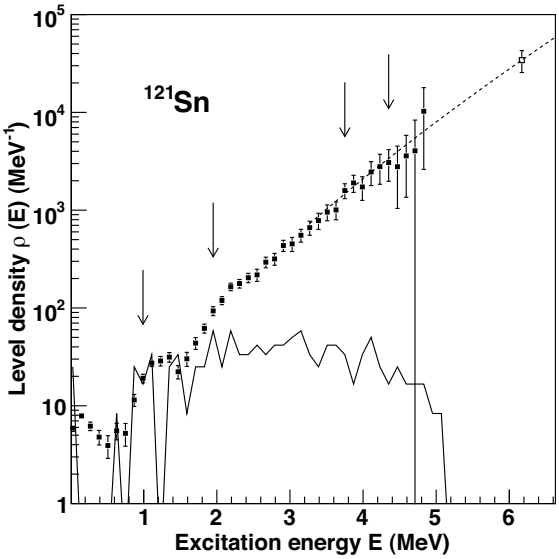

Figure 5.3: Normalised level density $\rho(E)$ (filled squares) as a function of final excitation energy E for ^{121}Sn. The energy bin is 120 keV/ch. The solid lines represent the discrete level density, obtained from spectroscopy. The dashed line is the predicted level density interpolation, scaled to agree with the normalisation value $\rho(S_n)$ (open square), which has been calculated from neutron-resonance data. The arrows show the two normalisation regions.

initial parity $\pi_\mathrm{i} = \pi_t$ (parity of the target in the neutron-capture reaction) by [21]:

$$\left\langle \Gamma_\gamma(E, I_\mathrm{i}, \pi_\mathrm{i}) \right\rangle = \frac{1}{2\pi\,\rho(E, I_\mathrm{i}, \pi_\mathrm{i})} \times \sum_{XL} \sum_{I_f, \pi_f} \int_{E_\gamma}^{E} \mathrm{d}E_\gamma \mathscr{T}_{XL}(E_\gamma)\,\rho(E - E_\gamma, I_f, \pi_f)\,. \tag{5.13}$$

The summations and the integration are over all final energy levels of spin I_f and parity π_f that are accessible through a γ-ray transition categorised by the γ-ray energy E_γ of electromagnetic character X and multipolarity L. It is clarified that the final state of I_f and π_f is the state after the γ-ray deexcitation of the nucleus, while the initial state of I_i and π_t is the state after the neutron-capture reaction and before the γ-ray transition.

In our experiment, we measure $B\mathscr{T}$, which will replace the component-based sum in Eq. (5.13). We set $\sum_{XL} \mathscr{T}_{XL} = B\mathscr{T}$.

We assume that there are equally many accessible states with positive and negative parity for all excitation energies and spins. Then we may simplify the level density function in Eq. (5.13) at the neutron separation energy S_n by:

$$\rho(S_n - E_\gamma, I_\mathrm{f}, \pm\pi) = \frac{1}{2}\rho(S_n - E_\gamma, I_\mathrm{f}). \tag{5.14}$$

We normalise $\mathscr{T}$ to experimental values of the average total radiative width at the neutron separation energy S_n, $\langle\Gamma_\gamma(S_n, I_\mathrm{i}, \pi_t)\rangle$. This quantity is measured in neutron-capture experiments (n,γ) and is often found in literature both for s-wave neutrons and for p-wave neutrons. In the following, we will consider s-wave resonances. The initial spin will then be $I_\mathrm{i} = I_t \pm 1/2$, where I_t is the spin of the target in the neutron-capture reaction. The final spin is $I_\mathrm{f} = I_t \pm 1/2 + J$, where J is the vector addition of the spin transfer in the γ-ray transition of multipolarity L, i.e., $J = -L, -L+1, ..., L$. Note that the factor $1/\rho(S_n, I_t \pm 1/2, \pi_t)$, seen in Eq. (5.13) for $E = S_n$ and assuming s waves, is recognised as the s-wave neutron level spacing D_0.

Further, we assume that the governing contribution to the experimental $\mathscr{T}$ is from dipole radiation, which is indeed the case in the measurements. This implies that the γ-ray transition has $L = 1$, which leads to J being any of -1, 0 or 1.

Our experimental data have been normalised to include all spins (see Sec. 5.2.1), while we now need to find the level density for I_f. We do this with the help of the spin distribution $g(E, I)$. At a general final excitation energy $E - E_\gamma$, Eq. (5.14) may be expressed as:

$$\rho(E - E_\gamma, I_\mathrm{f}) = \rho(E - E_\gamma) \sum_{J=-1}^{1} g(E - E_\gamma, I_t \pm 1/2 + J), \tag{5.15}$$

where the function $\rho(E - E_\gamma)$ is our experimental data for all spins. As a spin distribution we assume the same theoretical expression from Ref. [19], as in Sec. 5.2.1.

Combining all expressions, the average total radiative width at the neutron separation energy S_n for neutron s-wave capture resonances is given by:

$$\begin{aligned}\langle\Gamma_\gamma(S_n, I_t \pm 1/2, \pi_t)\rangle \;&=\; \frac{BD_0}{4\pi}\int_{E_\gamma=0}^{S_n} \mathrm{d}E_\gamma \mathscr{T}(E_\gamma)\rho(S_n - E_\gamma) \\ &\quad\times \sum_{J=-1}^{1} g(S_n - E_\gamma, I_t \pm 1/2 + J),\end{aligned} \tag{5.16}$$

where our measured data are inserted for $\mathscr{T}(E_\gamma)$ and $\rho(S_n - E_\gamma)$. We also insert the values of $\langle\Gamma_\gamma(S_n, I_t \pm 1/2, \pi_t)\rangle$ and D_0, which are known from experiments and given in literature. Afterwards, we solve for B.

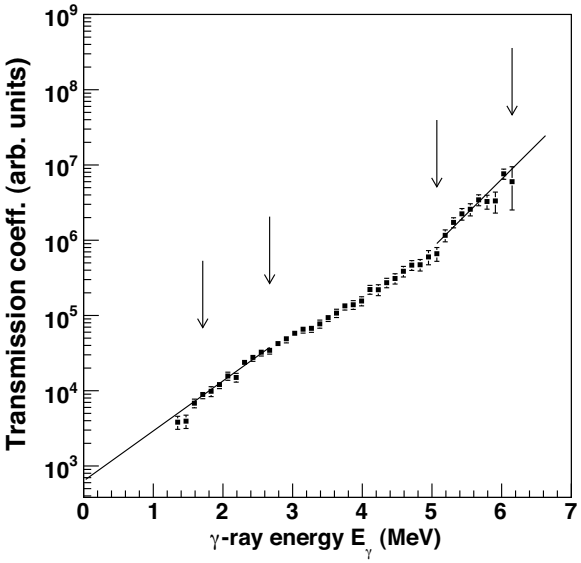

Figure 5.4: Normalised γ-ray transmission coefficient $\mathscr{T}(E_\gamma)$ as a function of γ-ray energy E_γ for ^{121}Sn. The γ-ray energy bin is 120 keV/ch. The arrows indicate the low and high γ-ray energy regions for which the data points are used to make the exponential extrapolations.

Some extra treatment of the transmission coefficient $\mathscr{T}$ is however performed before the calculation. The transmission coefficient is only determined for γ-ray energies $E_\gamma > E_\gamma{}^{\min}$ (see Eq. (5.4)), and the measurements at the highest E_γ below S_n suffer from poor statistics. Thus, the low and high-energy values of $\mathscr{T}$ are fitted with exponential extrapolations. The errors due to possibly poor extrapolations normally do not exceed 15% and are thus expected to be of minor importance [20]. Figure 5.4 demonstrates the extrapolations applied for normalising $\mathscr{T}$ in the case of ^{121}Sn.

5.3 The γ-ray strength function

The γ-ray strength function $f(E_\gamma)$ may be defined as [22]:

$$f_{XL}(E_\gamma) = \frac{\langle \Gamma_{\gamma\ell} \rangle}{E_\gamma{}^{2L+1} D_\ell}, \tag{5.17}$$

where $\langle \Gamma_{\gamma\ell} \rangle$ is the average radiative width, D_ℓ the level spacing for ℓ-wave resonances (usually *s*- or *p*-wave) obtained from neutron resonance experiments, and X and L denote the electromagnetic character and multipolarity, respectively, of the γ decay. The quantity transmission coefficient $\mathscr{T}(E_\gamma)$ is related to the strength function by:

$$\mathscr{T}(E_\gamma) = 2\pi \sum_{XL} {E_\gamma}^{2L+1} f_{XL}(E_\gamma) \,. \tag{5.18}$$

We estimate the γ-ray strength function from the normalised transmission coefficient $\mathscr{T}(E_\gamma)$ according to Eq. (5.18), assuming dipole radiation:

$$f(E_\gamma) = \frac{1}{2\pi {E_\gamma}^3} \mathscr{T}(E_\gamma) \,. \tag{5.19}$$

In the OCL experiments, we cannot distinguish between magnetic and electric dipole radiation, hence both contributions are included in our measurements. The normalised strength function of ^{121}Sn is as an example shown in Fig. 5.5.

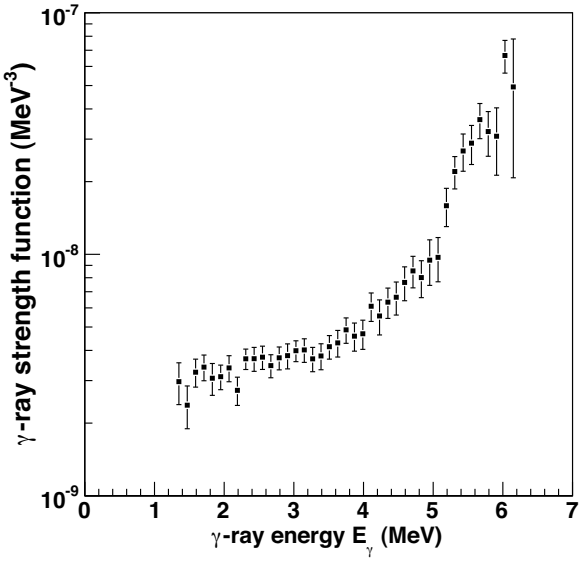

Figure 5.5: Normalised γ-ray strength function $f(E_\gamma)$ as a function of γ-ray energy for ^{121}Sn. The energy bin is 120 keV/ch.

Chapter 6

The $E1$ neutron-skin oscillation mode

The nature and origin of the low-energy pygmy electric dipole resonance in medium and heavy-mass neutron-rich nuclei are heavily debated. The present chapter provides a brief presentation of this resonance as a phenomenon.

Additional γ-ray strength, compared to standard strength models, are observed for γ-ray energies below the GEDR (located at $E_\gamma \approx 16$ MeV) in neutron-rich Sn isotopes, as well as in other neutron-rich medium-heavy or heavy nuclei. It has not been determined yet if the neutrons causing this extra strength are excited as single particles or as a collective phenomenon. However, there exist several theoretical analyses that predict the existence of a collective mode in these nuclei (see, e.g., Ref. [23] and references therein).

In the present thesis, we have chosen to call the extra strength in Sn a ”resonance”, assuming collectivity, even though it is questionable [23]. The term ”pygmy” is often applied on the resonance in the medium and heavy nuclei, which is understood by its relatively small integrated strength compared to the GEDR.

These nuclei are often assumed to have a so-called neutron skin. This skin is thought of as a thin layer of excess neutrons close to the nuclear surface. The densities of the core nucleons and the excess neutrons overlap, but the excess neutrons extend beyond the density of the core. The neutron-skin oscillation mode is thought to originate from the neutron skin being excited to perform collective oscillations against the proton-neutron core. The existence of this mode has not been experimentally confirmed yet. Though, several experiments have been performed with the aim to measure the thickness of the neutron skin (see Ref. [23] and references therein).

Many theoretical studies have investigated the collective approach. Until the beginning of the 1990 decade, macroscopical hydrodynamical models were applied. The nucleons were modeled as fluids and the resonance by classical

oscillations [23]. For instance the three-fluid hydrodynamical model [24], published as early as 1971, modeled three fluids: The protons, the neutrons located in the same orbitals as the protons, and the remaining neutrons. Another hydrodynamical study, of Van Isacker *et al.* [25], predicted an analytical expression for the ratio of the integrated strength of the pygmy resonance to that of the GEDR. This ratio is: $(N-N_c)Z/(Z+N_c)N$, where N_c is the number of neutrons in the core fluid. In Article 2, we compare this ratio for the Sn isotopes to the one estimated from our experiments. At the end of the 1990 decade, microscopical approaches replaced the macroscopical.

The predictions of the theoretical studies are very interesting. Microscopical calculations by, e.g., Paar *et al.* [26] and by Vretenar *et al.* [27] predict that the dynamics of the pygmy resonance and of the GEDR, both being $E1$ resonances, are completely different. The transition densities of the proton and the neutrons in the GEDR peak oscillate with opposite phases (characteristic for a isovector dipole mode). The dynamics of the pygmy resonance states is, however, that the proton and neutron densities are in phase (isoscalar) in the nucleus core, whereas only neutron excitations contribute to the transition density in the surface region. Thus, the pygmy resonance is indeed a separate mode not belonging to the tail of the GEDR. The neutron skin oscillates against the proton/neutron core, and it is the neutron skin that basically determines the properties of the pygmy resonance (see Ref. [23] and references therein). The presence of both isoscalar and isovector states in the pygmy resonance in Sn seems to have been experimentally confirmed. Recent measurements using the $(\alpha,\alpha'\gamma)$ coincidence method on ^{124}Sn compared to photon-scattering experiments shows a splitting into its isoscalar and isovector components [28].

There exists many theoretical studies of the evolution with increasing neutron number of the resonance's integrated strength and centroid energy. Most theoretical calculations predict a systematic increase of the strength. This is of course due to the increase of the neutron number in the skin. The predicted increase of integrated strength is often significant. Studies predicting such an increase in the Sn isotopes are, e.g., Paar [23], Daoutidis [29], Tsoneva and Lenske [30], Litvinova *et al.* [31], as well as Terasaki and Engel [32].

It is commented that the study of Daoutidis [29] predicts a relatively smaller increase of the integrated strength (thus a strength being relatively stable) in the atomic mass region $A = 120-126$, compared to other mass regions. Paar [23] predicts an overall increase, but with a local decrease with a local minimum in integrated strength around $A = 128-132$, caused by a combination of shell effects and reduced pairing correlations.

Most theoretical studies predict a decrease in the centroid energy of the pygmy resonance as the neutron number is increased. Examples are the investigations on Sn isotopes by Daoutidis [29], Tsoneva and Lenske [30], and Paar [23], as well

as on Ca isotopes by Tertychny *et al.* [33]. Daoutidis [29] predicts also a centroid energy that is relatively stable in the atomic mass region $A = 120 - 126$.

Experimental estimates of the centroid energy of the pygmy resonance exist for several Sn isotopes: $E_\gamma \approx 8.5$ MeV for ^{116,117}Sn from Utsunomiya [34], $E_\gamma \approx 7.8$ MeV for ^{117,119}Sn from Winhold *et al.* [35], and $E_\gamma = 10.1(7)$ MeV for ^{130}Sn and 9.8(7) MeV for ^{132}Sn from Adrich *et al.* [36]. The centroid energies of Ca isotopes determined from (γ,γ') experiments increase with increasing neutron number, which is a finding in contradiction to theoretical predictions (see Ref. [33] and references therein).

The classical Thomas-Reiche-Kuhn (TRK) sum rule gives the energy-weighted integrated strength of the pygmy resonance with respect to the GEDR, assuming that the pygmy resonance is built up by $E1$ radiation. TRK values of the pygmy resonance in Sn have been estimated from several types of experiments. Data on ^{116,117}Sn(γ,n) experiments from Utsunomiya *et al.* [34] indicate a TRK value of $\approx 1\%$. From ^{116,124}Sn(γ,γ') experiments by Govaert *et al.* [37], the value is calculated to $0.4 - 0.6\%$. Taking into account unresolved strength in the quasi continuum of typically a factor of $2 - 3$, the estimate from the measurements of Govaert is compatible to that of Utsunomiya.

The pygmy resonance in Sn has a relatively small integrated strength compared to the GEDR. Still, the pygmy resonance is expected to have a large impact in nuclear astrophysics. Its existence and its location close to the neutron separation energy may cause a large increase of the radiative neutron-capture cross sections of neutron-rich nuclei. This means that the neutron-capture rates in the so-called *r*-process nucleosynthesis are increased accordingly. Since the *r*-process nucleosynthesis produces neutron-rich nuclei heavier than Fe, the existence of the pygmy resonance may have important impacts on the calculated distribution of elemental abundance, as shown in calculations by Goriely *et al.* [38, 39].

If the resonance is caused by the predicted neutron-skin oscillation, its radiation will be of $E1$ character. Another electromagnetic character or multipolarity would have shown that the radiation is due to another mechanism. However, measurements confirming an $E1$ character do not automatically verify a neutron-skin oscillation origin.

A large number of experiments have indeed measured an $E1$ character in this energy region. Amongst these are several experiments on Sn isotopes: The nuclear resonance fluorescence experiments (NRF) performed on ^{116,124}Sn [37] and on ^{112,124}Sn [40], and the Coulomb dissociation experiments performed on $^{129-132}$Sn [36, 41].

It should be mentioned that an $M1$ character has been indicated in a proton inelastic-scattering experiment on ^{120,124}Sn [42], but that the experiments measuring an $E1$ character are in majority. Both $E1$ and $M1$ strength is expected to be present in this γ-ray energy region due to the tail of the GEDR and to the

magnetic spin-flip transitions building up the giant magnetic dipole resonance (GMDR), respectively. The GMDR is observed in many nuclei around the energy region of the pygmy resonance. Therefore, both $E1$ and $M1$ strength will anyway be present in the energy region of the pygmy resonance, and the strength of the tail of the GEDR is much larger than the strength from the GMDR.

Another possibility not ruled out is that the pygmy resonance in the Sn isotopes might instead be due to an enhanced GMDR. As shown in Article 1, the Sn isotopes have their proton Fermi level located right in between the $g_{7/2}$ and $g_{9/2}$ orbitals, and similarly their neutron Fermi level between $h_{11/2}$ and $h_{9/2}$. This may cause proton $g_{7/2} \leftrightarrow g_{9/2}$ and neutron $h_{11/2} \leftrightarrow h_{9/2}$ magnetic spin-flip transitions. To summarise, clarification of the electromagnetic character of the Sn pygmy resonance is of utmost importance.

Chapter 7

Articles

The following articles are included in this thesis:

1. H. K. Toft, A. C. Larsen, U. Agvaanluvsan, A. Bürger, M. Guttormsen, G. E. Mitchell, H. T. Nyhus, A. Schiller, S. Siem, N. U. H. Syed, and A. Voinov, *Level densities and γ-ray strength functions in Sn isotopes*, Phys. Rev. C **81**, 064311 (2010).

2. H. K. Toft, A. C. Larsen, A. Bürger, M. Guttormsen, A. Görgen, H. T. Nyhus, T. Renstrøm, S. Siem, G. M. Tveten, and A. Voinov, *Evolution of the pygmy dipole resonance in Sn isotopes*, accepted for publication in Phys. Rev. C.

3. A. C. Larsen, M. Guttormsen, M. Krtička, E. Běták, A. Bürger, A. Görgen, H. T. Nyhus, J. Rekstad, A. Schiller, S. Siem, H. K. Toft, G. M. Tveten, A. V. Voinov, and K. Wikan, *Analysis of possible systematic errors in the Oslo method*, accepted for publication in Phys. Rev. C.

7.1 Article 1: Level densities and γ-ray strength functions in Sn isotopes

The experimental level densities of ^{118,119}Sn and the γ-ray strength functions of ^{116,118,119}Sn below the neutron separation energy are extracted with the Oslo method using the (^{3}He,$\alpha\gamma$) and (^{3}He,^{3}He$'\gamma$) reactions.

The level density function of ^{119}Sn displays step-like structures. The experimental microcanonical entropies are deduced from the level densities, and the single neutron entropy of ^{119}Sn is determined to be $\Delta S = 1.7 \pm 0.2\, k_B$. Results from a simple microscopic model [43, 44, 45] support the interpretation that some of the low-energy steps in the level density function are caused by neutron pair breaking.

An enhancement in the experimental ^{116,118,119}Sn γ-ray strength functions, compared to the generalised Lorentzian (GLO) [46] model for radiative strength, is observed for the γ-ray energy region of $4.5 \lesssim E_\gamma \lesssim 11$ MeV. These small resonances all have a centroid energy of $E_\gamma = 8.0(1)$ MeV and an integrated strength corresponding to $1.7(9)\%$ of the classical Thomas-Reiche-Kuhn (TRK) sum rule.

Level densities and γ-ray strength functions in Sn isotopes

H. K. Toft,[1,*] A. C. Larsen,[1] U. Agvaanluvsan,[2,3] A. Bürger,[1] M. Guttormsen,[1] G. E. Mitchell,[4,5] H. T. Nyhus,[1] A. Schiller,[6] S. Siem,[1] N. U. H. Syed,[1] and A. Voinov[6]

[1]*Department of Physics, University of Oslo, N-0316 Oslo, Norway*
[2]*Stanford University, Palo Alto, California 94305, USA*
[3]*MonAme Scientific Research Center, Ulaanbaatar, Mongolia*
[4]*Department of Physics, North Carolina State University, Raleigh, North Carolina 27695, USA*
[5]*Triangle Universities Nuclear Laboratory, Durham, North Carolina 27708, USA*
[6]*Department of Physics, Ohio University, Athens, Ohio 45701, USA*

(Received 30 March 2010; published 16 June 2010)

The nuclear level densities of ^{118,119}Sn and the γ-ray strength functions of ^{116,118,119}Sn below the neutron separation energy are extracted with the Oslo method using the (^{3}He,$\alpha\gamma$) and (^{3}He,^{3}He$'\gamma$) reactions. The level-density function of ^{119}Sn displays steplike structures. The microcanonical entropies are deduced from the level densities, and the single neutron entropy of ^{119}Sn is determined to be $1.7 \pm 0.2\ k_B$. Results from a combinatorial model support the interpretation that some of the low-energy steps in the level density function are caused by neutron pair breaking. An enhancement in all the γ-ray strength functions of $^{116-119}$Sn, compared to standard models for radiative strength, is observed for the γ-ray energy region of $\simeq$4–11 MeV. These small resonances all have a centroid energy of 8.0(1) MeV and an integrated strength corresponding to 1.7(9)% of the classical Thomas-Reiche-Kuhn sum rule. The Sn resonances may be due to electric dipole neutron skin oscillations or to an enhancement of the giant magnetic dipole resonance.

DOI: 10.1103/PhysRevC.81.064311 PACS number(s): 21.10.Ma, 24.10.Pa, 24.30.Gd, 27.60.+j

I. INTRODUCTION

The level-density and the γ-ray strength function are average quantities describing atomic nuclei. They are important for many aspects of fundamental and applied nuclear physics, including calculations of nuclear properties, like reaction cross sections. Such cross sections are used for calculations in, e.g., reactor physics and nuclear waste management, and of nuclear reaction rates in astrophysics for modeling of nucleosynthesis in stars.

The nuclear level density of nuclei is defined as the number of levels per unit of excitation energy. The entropy and other thermodynamic properties may also be determined from the level density. Structures in the level density are expected to be due to shell gaps, breaking of nucleon Cooper pairs, and/or changes in the nuclear shape. In the majority of previous experiments, the level density is measured either only at low energy by direct counting (conventional spectroscopy) or at higher energy around the neutron/proton separation energies (nuclear resonance measurements).

The γ-ray strength function may be defined as the reduced average transition probability as a function of γ-ray energy. This quantity characterizes average electromagnetic properties of excited nuclei. The strength function reveals essential information about the nuclear structure. Electric transitions are mostly influenced by the proton charge distribution, while magnetic transitions are also affected by the neutron distribution due to the magnetic dipole moment of the neutron. The shape and softness of the nuclear surface are other important factors for the nuclear response to electromagnetic radiation.

The large number of stable isotopes in Sn makes the element suitable for systematic studies. This article presents the level densities of ^{118,119}Sn and the γ-ray strength functions of ^{116,118,119}Sn for energies in the quasicontinuum below the neutron separation energy. The measurements have been performed at the Oslo Cyclotron Laboratory (OCL). The ^{118,119}Sn results are compared with earlier OCL studies on other isotopes. In Ref. [1], the level-density functions of ^{116,117}Sn were shown to display steps that are much more distinctive than previously measured for other mass regions. The steps were interpreted as neutron pair breaking. In Ref. [2], a resonance-like structure in the γ-ray strength function was measured below the neutron threshold in ^{117}Sn. A combinatorial model is also used in this article to study, e.g., the origin of the level-density steps and the impact of collective effects.

The experimental setup and the data analysis are briefly described in Sec. II. The normalized experimental results for level density and entropy are presented in Sec. III. Section IV discusses the nuclear properties extracted from the level density with the combinatorial model. Section V presents the normalized experimental γ-ray strength functions. Conclusions are drawn in Sec. VI.

II. EXPERIMENTAL SETUP AND DATA ANALYSIS

The self-supporting ^{119}Sn target was enriched to 93.2% and had a mass thickness of 1.6 mg/cm^2. For three days the target was exposed to a 38-MeV ^{3}He beam with an average current of $\sim$1.5 nA. The reaction channels studied were ^{119}Sn(^{3}He,^{3}He$'\gamma$)^{119}Sn and ^{119}Sn(^{3}He,$\alpha\gamma$)^{118}Sn.

Particle-γ coincidences were recorded with seven collimated Si particle ΔE-E telescopes and 26 collimated NaI(Tl) γ-ray detectors. The ΔE and E detector thicknesses were about 140 and 1500 μm, respectively. These detectors were

*h.k.toft@fys.uio.no

placed at 45° with respect to the beam axis. The NaI detectors are distributed on a sphere and constitute the CACTUS multidetector system [3]. The total solid-angle coverages out of 4π were approximately 1.3% for the particle detectors and 16% for the γ-ray detectors.

In the data analysis, the measured ejectile's energy is transformed into excitation energy of the residual nucleus using reaction kinematics. The γ-ray spectra for various initial excitation energies are unfolded with the known response functions of CACTUS and the Compton subtraction method [3]. The Compton subtraction method preserves the fluctuations in the original spectra without introducing further, spurious fluctuations.

The first-generation γ-ray spectra are extracted from the unfolded total γ-ray spectra by the subtraction procedure described in Ref. [4]. The main assumption is that the γ decay from any excitation energy bin is independent of the method of formation—whether it is directly formed by a nuclear reaction or indirectly by γ decay from higher lying states following the initial reaction.

The first-generation γ-ray spectra are arranged in a two-dimensional matrix $P(E,E_\gamma)$. The entries of P are the probabilities $P(E,E_\gamma)$ that a γ ray of energy E_γ is emitted from an energy bin of excitation energy E. This matrix is used for the simultaneous extraction of the γ-ray strength function and the level-density function.

The first-generation matrix P is factored into the level-density function ρ and the radiative transmission coefficient $\mathcal{T}$ [5]:

$$P(E,E_\gamma) \propto \mathcal{T}(E_\gamma)\rho(E-E_\gamma). \tag{1}$$

The factorization of P into two components is justified for nuclear reactions leading to a compound state prior to a subsequent γ decay [6]. Equation (1) may also be regarded as a variant of Fermi's golden rule: The decay rate is proportional to the density of the final state and the square of the matrix element between the initial and final state. The factorization is performed by an iterative procedure where the independent functions ρ and $\mathcal{T}$ are adjusted until a global χ^2 minimum with the experimental $P(E,E_\gamma)$ is reached.

As shown in Eq. (1), the transmission coefficient is assumed to be a function of only E_γ, in accordance with the generalized form of the Brink-Axel hypothesis [7,8]. This hypothesis states that a giant electric dipole resonance, and all other collective excitation modes, may be built on any excited state and still have the same properties as the one built on the ground state. Hence, the transmission coefficient is independent of excitation energy.

Equation (1) determines only the functional forms of ρ and $\mathcal{T}$. The entries of P are invariant under the following transformations [5]:

$$\tilde{\rho}(E-E_\gamma) = A\exp[\alpha(E-E_\gamma)]\rho(E-E_\gamma), \tag{2}$$

$$\tilde{\mathcal{T}}(E_\gamma) = B\exp(\alpha E_\gamma)\mathcal{T}(E_\gamma). \tag{3}$$

The final step of the Oslo method is to determine the normalization parameters. The parameters A and B will define the absolute values of ρ and $\mathcal{T}$, respectively, while α will define their common slope.

III. LEVEL DENSITIES

A. Normalization and experimental results

The constants A and α in Eq. (2), which are needed to normalize the experimental level density ρ, are determined using literature values of the known discrete energy levels at low energy and of the level spacing D at the neutron separation energy S_n, obtained from neutron resonance experiments.

The normalization value $\rho(S_n)$ is calculated either from the s-wave level spacing $D_0(S_n)$ or from the p-wave level spacing $D_1(S_n)$. The level spacings are taken from Refs. [9,10]. To establish an expression for the value of $\rho(S_n)$, it is necessary to assume models for the spin distribution $g(E,I)$ and the spin cut-off parameter σ. We choose the back-shifted Fermi gas (BSFG) model with the original parametrization of von Egidy *et al.* [11], because this parametrization gives the most appropriate normalization of these nuclei when comparing to other experimental measurements (see also Ref. [1]).

Here, these functions are kept as the original Gilbert and Cameron expressions [12], but with a redefined parametrization of the nucleus' intrinsic excitation energy U and the level-density parameter a. The spin distribution is expressed as [11]:

$$g(E,I) \simeq \frac{2I+1}{2\sigma^2}\exp[-(I+1/2)^2/2\sigma^2], \tag{4}$$

where I is the spin and where the spin cut-off parameter $\sigma(E)$ is given by:

$$\sigma^2 = 0.0888A^{2/3}aT, \tag{5}$$

where A is the mass number of the isotope and T is the nuclear temperature given by $T=\sqrt{U/a}$. Here, the level-density parameter is defined as $a = 0.21A^{0.87}\mathrm{MeV}^{-1}$, while the shifted excitation energy U is defined as $U = E - E_{\mathrm{pair}} - C_1$. The back-shift parameter is defined as $C_1 = -6.6A^{-0.32}$ MeV. The pairing energy E_{pair} is calculated from the proton and neutron pair-gap parameters: $E_{\mathrm{pair}} = \Delta_p + \Delta_n$. The pair-gap parameters are evaluated from the even-odd mass differences found in Ref. [13] according to the method of Ref. [14].

Assuming this spin distribution and equal numbers of levels with positive and negative parity, the level density at S_n may be expressed as, for s-wave neutron resonances [5,15]:

$$\rho_0(S_n) = \frac{2\sigma^2}{D_0}\left\{(I_t+1)\exp\left[\frac{-(I_t+1)^2}{2\sigma^2}\right] + I_t\exp\left[\frac{-{I_t}^2}{2\sigma^2}\right]\right\}^{-1}, \tag{6}$$

and for p-wave resonances [15]:

$$\rho_1(S_n) = \frac{2\sigma^2}{D_1}\left\{(I_t-1)\exp\left[\frac{-(I_t-1)^2}{2\sigma^2}\right] + I_t\exp\left[\frac{-{I_t}^2}{2\sigma^2}\right] + (I_t+1)\exp\left[\frac{-(I_t+1)^2}{2\sigma^2}\right] + (I_t+2)\exp\left[\frac{-(I_t+2)^2}{2\sigma^2}\right]\right\}^{-1}, \tag{7}$$

where the spin cut-off parameter is evaluated at S_n and where I_t is the spin of the target.

TABLE I. Input parameters and the resulting values for the calculation of the normalization value $\rho(S_n)$ and the input parameters for the BSFG interpolation and the required values of the scaling parameter η.

Nucleus	S_n (MeV)	$D_0(S_n)$ (eV)	a (MeV^{-1})	C_1 (MeV)	Δ_n (MeV)	Δ_p (MeV)	$\sigma(S_n)$	$\rho(S_n)$ (10^4 MeV^{-1})	η
^{119}Sn	6.485	700(150)	13.43	−1.43	0	1.02	4.55	6.05(175)	0.44
^{118}Sn	9.326	61(7)	13.33	−1.43	1.19	1.24	4.74	38.4(86)	0.59

A higher $\rho(S_n)$ is obtained from the level spacing of D_0 than of D_1, according to calculations on both isotopes. As the highest value of the level density is presumed to be the best estimate, D_0 is chosen in the following. The input parameters and the resulting values of the normalization data $\rho(S_n)$ are given in Table I.

The experimental data for the level densities are not obtained up to the excitation energy of S_n. There is a gap, and the level density in the gap and below is estimated according to the level-density prediction of the BSFG model with the parametrization of von Egidy *et al.* [11]. This is a consistency choice in order to keep the spin distribution and the spin cut-off parameter the same as the ones used during the calculation of $\rho(S_n)$ based on the neutron resonance data. The BSFG level density, for all spins and as a function of excitation energy, is given by

$$\rho(E)_{\mathrm{BSFG}} = \frac{\exp\left(2\sqrt{aU}\right)}{12\sqrt{2}a^{1/4}U^{5/4}\sigma}. \tag{8}$$

A scaling parameter η is applied to the BSFG formula,

$$\rho(E)_{\mathrm{BSFG}} \rightarrow \eta\rho(E)_{\mathrm{BSFG}}, \tag{9}$$

in order to make its absolute value at S_n agree with the normalization value $\rho(S_n)$. We then get a level-density interpolation that overlaps with the measurements, and to which the measurements are normalized. The values of η are shown in Table I.

Figure 1 shows the normalized level densities in ^{118,119}Sn. The arrows indicate the regions used for normalization. As expected, the level densities of ^{119}Sn and ^{118}Sn are very similar to those of ^{117}Sn and ^{116}Sn [1], respectively. The figure also shows that the known discrete levels [16] seem to be complete up to ∼2 MeV in ^{119}Sn and up to ∼3 MeV in ^{118}Sn. Hence, our experiment has filled a region of unknown level density from the discrete region and to the gap, approximately at S_n − 1 MeV. Unlike ^{119}Sn, the ground state of the even-even nucleus ^{118}Sn has no unpaired neutron, and accordingly it has fewer available states than ^{119}Sn. Therefore, measuring all levels to higher excitation energies by conventional methods is easier in ^{118}Sn.

An alternative interpolation method to describe the gap between our measured data and the neutron-resonance-data–based $\rho(S_n)$ is the constant temperature (CT) model [12]. This approximation gives

$$\rho(E) = \frac{1}{T}\exp\left[(E - E_0)/T\right], \tag{10}$$

where the "temperature" T and the energy shift E_0 are treated as free parameters. Figure 2 shows a comparison of the CT model and the BSFG model as interpolation methods for ^{118}Sn. The small difference in the region of interpolation is negligible for the normalization procedure.

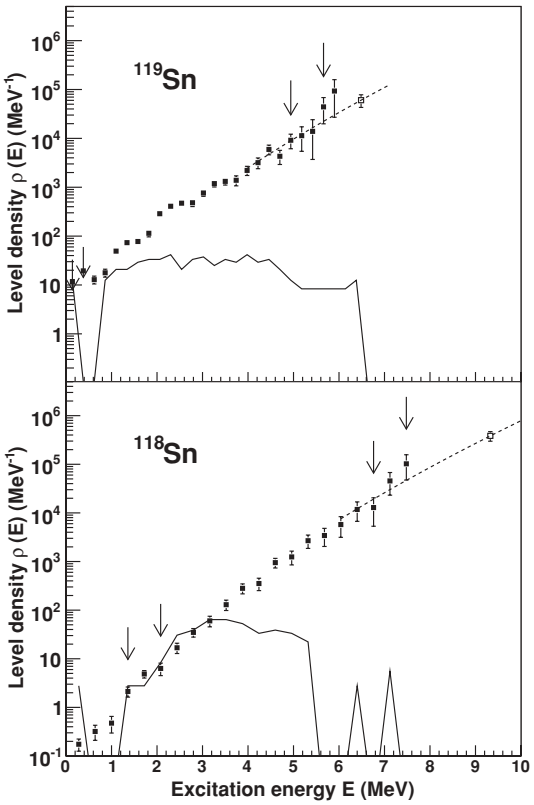

FIG. 1. Normalized level densities of ^{119}Sn (upper panel) and ^{118}Sn (lower panel) as a function of excitation energy. Our experimental data are marked with filled squares. The dashed lines are the BSFG predictions that are used for interpolation, scaled to coincide with $\rho(S_n)$ (open squares), which are calculated from neutron resonance data. The solid lines represent the discrete level densities obtained from counting the known levels. The arrows indicate the regions used to normalize the absolute values and the slope. The energy bins are 360 and 240 keV/ch for ^{118,119}Sn, respectively.

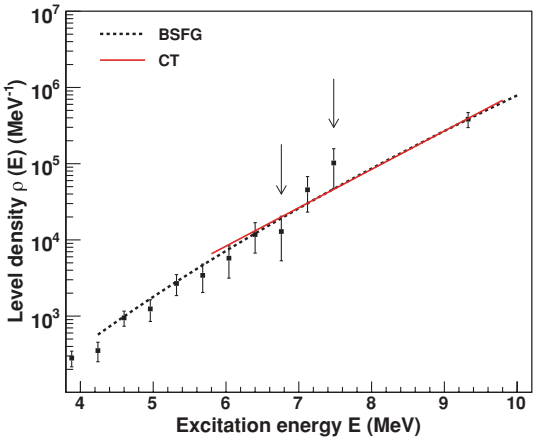

FIG. 2. (Color online) Comparison of the BSFG model (dashed line) and the CT model (solid line) as interpolation means for the level density of ^{118}Sn. The arrows indicate the region of normalization. The parameters in the CT model ($T = 0.86$ MeV and $E_0 = -1.7$ MeV) have been found from a least χ^2 fit to the data points in this region and from matching $\rho(S_n)$, and the parametrization is not intended to be appropriate elsewhere.

B. Steplike structures

In Fig. 1, the level density of ^{119}Sn shows a steplike structure superimposed on the general level density, which is smoothly increasing as a function of excitation energy. A step is characterized by an abrupt increase of level density within a small energy interval. The phenomenon of steps was also seen in ^{116,117}Sn [1].

Distinctive steps in ^{119}Sn are seen below ∼4 MeV. They are, together with the steps of ^{116,117}Sn [1], the most distinctive steps measured so far at OCL. This may be explained by Sn having a magic number of protons, $Z = 50$. As long as the excitation energy is less than the energy of the proton shell gap, only neutron pairs are broken. The steps are distinctive since no proton pair breaking smears the level-density function.

The steps are less pronounced for ^{118}Sn than for ^{119}Sn. This is in contradiction to what is expected, as ^{118}Sn is an even-even nucleus without the unpaired neutron reducing the clearness of the steps in ^{119}Sn. The explanation probably lies in poorer statistics for the (^{3}He,α) reaction channel than for (^{3}He, ^{3}He′). To reduce the error bars, a larger energy bin is chosen for ^{118}Sn, leading to smearing the data and less clear structures.

Two steps in ^{119}Sn are particularly distinctive: one at ∼1.0 MeV and another at ∼2.0 MeV, leading to bumps in the region around 1.2–1.4 MeV and around ∼2.2–2.6 MeV, respectively. The steps in ^{119}Sn are found at approximately the same locations as in ^{117}Sn [1].

Also for ^{116}Sn, two steps were clearly seen for low excitation energy [1]. The first of these is probably connected to the isotope's first excited state, at 1.29 MeV [16]. A similar step in ^{118}Sn would probably also had been found connected to the first excited state, at 1.23 MeV [16], if the measured data had had better statistics.

Microscopic calculations based on the seniority model indicate that step structures in level-density functions may be explained by the consecutive breaking of nucleon Cooper pairs [17]. The steps for ^{119}Sn in Fig. 1 are probable candidates for the neutron pair-breaking process. The neutron pair-breaking energy of ^{119}Sn is estimated[1] to be $2\Delta_n = 2.5$ MeV, which supports neutron pair breaking as the origin of the pronounced bump around ∼2.2–2.6 MeV.

However, if the applied values of the neutron pair-gap parameters are accurate, the pronounced step at ∼1.0 MeV in ^{119}Sn and other steps below this energy are probably not due to pure neutron pair breaking. They might be due to more complex structures, involving collective effects such as vibrations and/or rotations. In subsection IV C, the pair breaking in our isotopes will be investigated further.

C. Entropy

In many fields of natural science, the entropy is used to reveal the degree of order/disorder of a system. In nuclear physics, the entropy may describe the number of ways the nucleus can arrange for a certain excitation energy. Various thermodynamic quantities may be deduced from the entropy, e.g., temperature, heat capacity, and chemical potential. The study of nuclear entropy also exhibits the amount of entropy gained from the breaking of Cooper pairs. We would like to study the entropy difference between odd-A and even-even Sn isotopes.

The microcanonical entropy is defined as

$$S_s(E) = k_B \ln \Omega_s(E), \tag{11}$$

where k_B is the Boltzmann constant, which is set to unity to make the entropy dimensionless, and where $\Omega_s(E)$ is the state density (multiplicity of accessible states). The state density is proportional to the experimental level density $\rho(E)$ by

$$\Omega_s(E) \propto \rho(E)\,[2\langle I(E)\rangle + 1]\,, \tag{12}$$

where $\langle I(E)\rangle$ is the average spin within an energy bin of excitation energy E. The factor $2\langle I(E)\rangle + 1$ is the spin degeneracy of magnetic substates.

The spin distribution is not well known, so we assume the spin degeneracy factor to be constant and omit it. Omitting this factor is first grounded by the spin being averaged over each energy bin, leading to only the absolute value of the state density at high excitation energies being altered, and not the structure.

Second, the average spin $\langle I(E)\rangle$ is expected to be a slowly varying function of energy (see Sec. IV). Hence, a "pseudo"

[1]The values of the neutron pair-breaking $2\Delta_n$ and the proton pair-breaking $2\Delta_p$ for ^{118,119}Sn are estimated from the $\Delta_{n/p}$ values in Table I, except for Δ_n of ^{119}Sn. We estimate the energy for breaking a neutron pair in ^{119}Sn as the mean value of $2\Delta_n$ of the neighboring even-even nuclei, redefining its value to be $2\Delta_n = 2.5$ MeV.

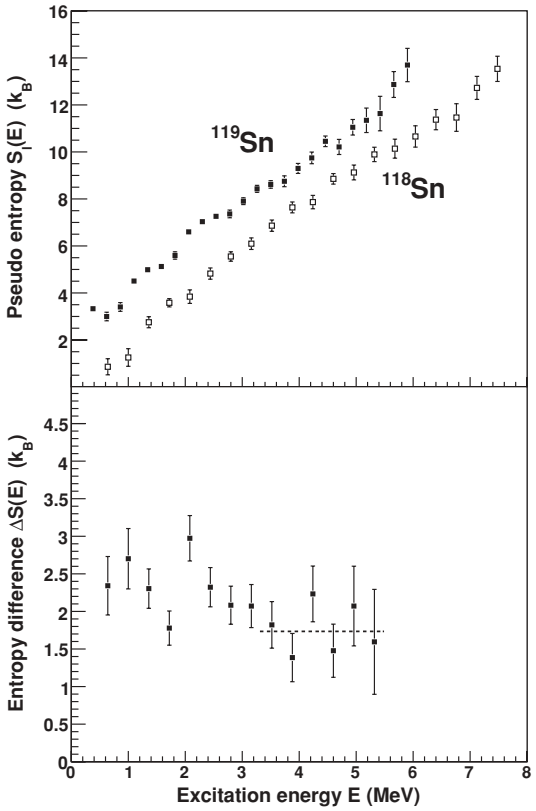

FIG. 3. (Upper panel) Experimental pseudo entropies S_l of ^{119}Sn (filled squares) and ^{118}Sn (open squares) as a function of excitation energy. (Lower panel) The respective experimental entropy difference, $\Delta S = S_l{}^{119} - S_l{}^{118}$, as a function of excitation energy. An average value of $\overline{\Delta S}(E) = 1.7 \pm 0.2\ k_B$ is obtained from a χ^2 fit (dashed line) to the experimental data above $\sim$3 MeV.

entropy S_l may be defined based only on the level density $\rho(E)$:

$$S_l(E) = k_B \ln\left[\frac{\rho(E)}{\rho_0}\right]. \tag{13}$$

The constant ρ_0 is chosen so that $S_l = 0$ in the ground state of the even-even nucleus ^{118}Sn. This is satisfied for $\rho_0 = 0.135\ \text{MeV}^{-1}$. The same value of ρ_0 is used for ^{119}Sn.

Figure 3 shows the experimental results for the pseudo entropies of ^{118,119}Sn. These pseudo entropy functions are very similar to those of ^{116,117}Sn [1], which is as expected from the general similarity of the level-density functions of these isotopes.

We define the entropy difference as

$$\Delta S(E) = S_l{}^A - S_l{}^{A-1}, \tag{14}$$

where the superscript denotes the mass number of the isotope. Assuming that entropy is an extensive quantity, the entropy difference will be equal to the entropy of the valence neutron, i.e., the experimental single neutron entropy of ^{A}Sn.

For midshell nuclei in the rare-earth region, a semiempirical study [18] has shown that the average single nucleon entropy is $\overline{\Delta S} \simeq 1.7\ k_B$. This is true for a wide range of excitation energies, e.g., both for 1 and 7 MeV. Hence for these nuclei, the entropy simply scales with the number of nucleons not coupled in Cooper pairs, and the entropy difference is merely a simple shift with origin from the pairing energy.

Figure 3 also shows the entropy difference ΔS of ^{118,119}Sn, which are midshell in the neutrons only. Above $\sim$3 MeV, the entropy difference may seem to approach a constant value. In the energy region where the entropy difference might be constant (shown as the dashed line in Fig. 3), we have calculated its mean value as $\overline{\Delta S} = 1.7 \pm 0.2\ k_B$. Within the uncertainty, this limit is in good agreement with the general conclusion of the above-mentioned semiempirical study [18] and with the findings for ^{116,117}Sn [1]. For lower excitation energy, however, Fig. 3 shows that the entropy difference of ^{118,119}Sn is not a constant, unlike the rare-earth midshell nuclei. Hence, the ^{118,119}Sn isotopes have an entropy difference that is more complicated than a simple excitation energy shift of the level-density functions.

IV. NUCLEAR PROPERTIES EXTRACTED WITH A COMBINATORIAL BCS MODEL

A simple microscopic model [19–21] has been developed for further investigation of the underlying nuclear structure resulting in the measured level-density functions. The model distributes Bardeen-Cooper-Schrieffer (BCS) quasiparticles on single-particle orbitals to make all possible proton and neutron configurations for a given excitation energy E. On each configuration, collective energy terms from rotation and vibration are schematically added. Even though this is a very simple representation of the physical phenomena, this combinatorial BCS model reproduces rather well the experimental level densities. As a consequence, the model is therefore assumed to be able to predict also other nuclear properties of the system. We are first and foremost interested in investigating the level-density steps and in investigating the assumption of parity symmetry used in the normalization processes of the Oslo method.

A. The model

The single-particle energies e_{sp} are calculated from the Nilsson model for a nucleus with an axially deformed core of quadrupole deformation parameter ϵ_2. The values of the deformation parameters are $\epsilon_2 = 0.111$ and $\epsilon_2 = 0.109$ [22] for ^{118,119}Sn, respectively. Also needed for the calculation of the Nilsson energy scheme are the Nilsson parameters κ and μ and the oscillator quantum energy between the main oscillator shells: $\hbar\omega_0 = 41A^{-1/3}$. The adopted values are $\kappa = 0.070$ and $\mu = 0.48$ for both neutrons and protons and for both nuclei, in agreement with the suggestion of Ref. [23]. All input parameters are listed in Table II. The resulting Nilsson scheme for ^{118}Sn is shown in Fig. 4.

The parameter λ represents the quasiparticle Fermi level. It is iteratively determined by reproducing the right numbers of

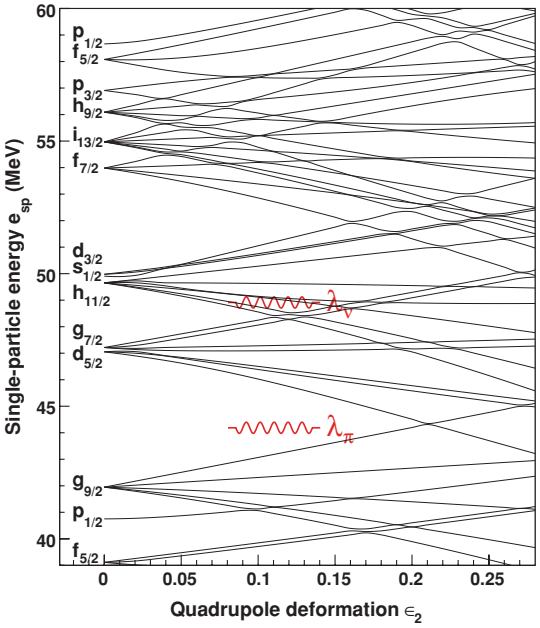

FIG. 4. (Color online) The Nilsson level scheme, showing single-particle energies as functions of quadrupole deformation ϵ_2, for ^{118}Sn, which has $\epsilon_2 = 0.111$. The Nilsson parameters are set to $\kappa = 0.070$ and $\mu = 0.48$. The Fermi levels are illustrated as curled lines (λ_π for protons and λ_ν for neutrons).

neutrons and protons in the system. The resulting Fermi levels for our nuclei are listed in Table II and illustrated for ^{118}Sn in Fig. 4.

The microscopic model uses the concept of BCS quasiparticles [24]. Here, the single quasiparticle energies $e_{\rm qp}$ are defined by the transformation of:

$$e_{\rm qp} = \sqrt{(e_{\rm sp} - \lambda)^2 + \Delta^2}. \tag{15}$$

The pair-gap parameter Δ is treated as a constant, as before, and with the same values.

The proton and neutron quasiparticle orbitals are characterized by their spin projections on the symmetry axes Ω_π and Ω_ν, respectively. The energy due to quasiparticle excitations is given by the sum of the proton and neutron energies and of a residual interaction V:

$$E_{\rm qp}(\Omega_\pi, \Omega_\nu) = \sum_{\{\Omega'_\pi, \Omega'_\nu\}} e_{\rm qp}(\Omega'_\pi) + e_{\rm qp}(\Omega'_\nu) + V(\Omega'_\pi, \Omega'_\nu). \tag{16}$$

In the model, quasiparticles having Ω's of different sign will have the same energy, i.e., one has a level degeneracy. Since no such degeneracy is expected, a Gaussian random distribution V is introduced to compensate for a residual interaction apparently not taken into account by the Hamiltonian of the model. The maximum allowed number of broken Cooper pairs in our system is three, giving a total of seven quasiparticles for the even-odd nucleus ^{119}Sn. Technically, all configurations are found from systematic combinations.

On each configuration, both a vibrational band and rotations are built. The energy of each level is found by adding the energy of the configuration and the vibrational and rotational terms:

$$E = E_{\rm qp}(\Omega_\pi, \Omega_\nu) + \hbar\omega_{\rm vib}\nu + A_{\rm rot} R\,(R+1)\,. \tag{17}$$

The vibrational term is described by the oscillator quantum energy $\hbar\omega_{\rm vib}$ and the phonon quantum number $\nu = 0, 1, 2, \ldots$ The values of $\hbar\omega_{\rm vib}$ are found from the 2^+ and 3^- vibrational states of the even-even nucleus and are shown in Table II. The last term of Eq. (17) represents the rotational energy. The quantity $A_{\rm rot} = \hbar^2/2\mathcal{J}$ is the rotational parameter with $\mathcal{J}$ being the moment of inertia, and R is the rotational quantum number. The rotational quantum number has the values of $R = 0, 1, 2, 3\ldots$ for the even-odd nucleus ^{119}Sn, and $R = 0, 2, 4\ldots$ for the even-even nucleus ^{118}Sn.

For low excitation energy, the value of the rotational parameter $A_{\rm rot}$ is determined around the ground state $A_{\rm gs}$. At high energy, the rotation parameter is found from a rigid, elliptical body, which is [25]:

$$A_{\rm rigid} = \frac{5\hbar^2}{4MR_A^2\,(1 + 0.31\epsilon_2)}. \tag{18}$$

Here, M is the mass and R_A the radius of the nucleus. For nuclei in the medium mass region, $A \sim 50 - 70$, the rotational parameter $A_{\rm rigid}$ is obtained at the neutron separation energy, according to a theoretical prediction [26]. We assume that $A_{\rm rigid}$ is obtained at the neutron separation energy also for our nuclei. The applied values of $A_{\rm gs}$ and $A_{\rm rigid}$ are listed in Table II. The function $A_{\rm rot}$ as a function of energy is estimated from a linear interpolation between these.

TABLE II. Input parameters used in the combinatorial BCS model and the resulting values for the Fermi levels λ_ν (neutrons) and λ_π (protons).

Nucleus	ϵ_2	κ	μ	$\hbar\omega_0$ (MeV)	$A_{\rm gs}$ (MeV)	$A_{\rm rigid}$ (MeV)	$\hbar\omega_{\rm vib,e-e}$ (MeV)	λ_ν (MeV)	λ_π (MeV)
^{119}Sn	0.109	0.070	0.48	8.34	0.200	0.0122	1.23; 2.32	48.9	44.1
^{118}Sn	0.111	0.070	0.48	8.36	0.205	0.0124	1.23; 2.32	48.9	44.2

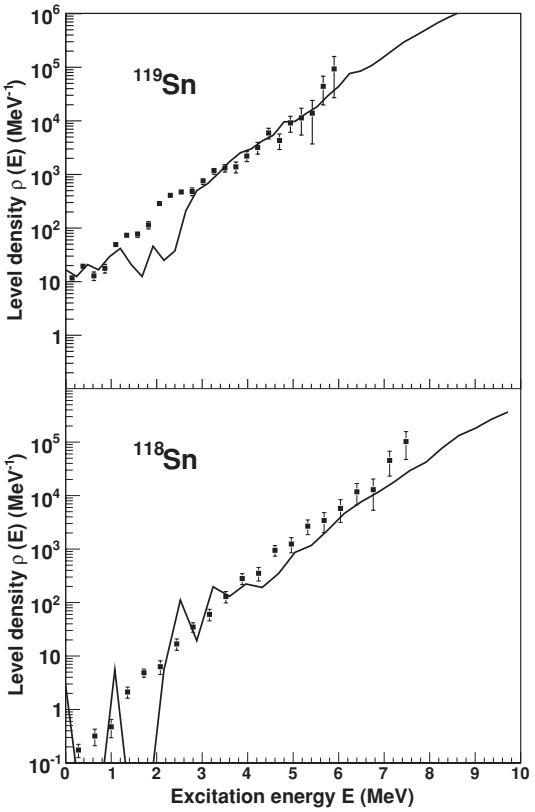

FIG. 5. Level densities of ^{119}Sn (upper panel) and ^{118}Sn (lower panel) as a function of excitation energy. The solid lines are the theoretical predictions of the combinatorial BCS model. The squares are our experimental data.

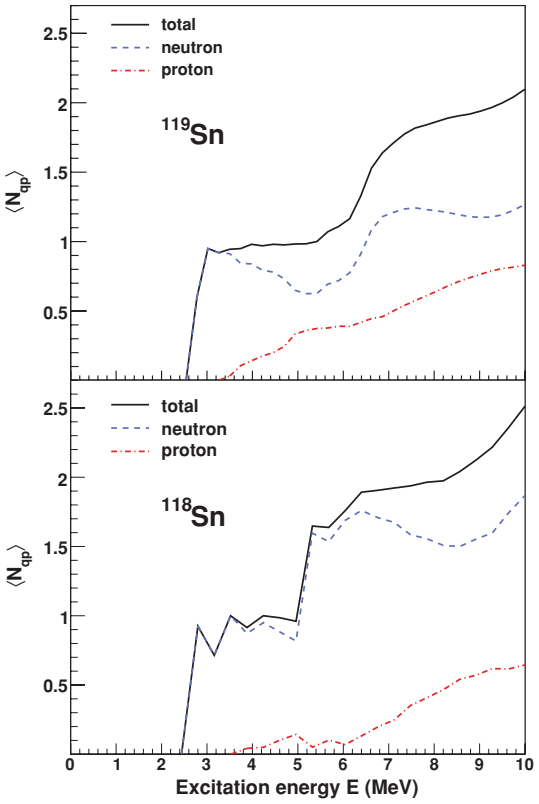

FIG. 6. (Color online) The average number of broken quasiparticle pairs $\langle N_{qp} \rangle$ (solid line) as a function of excitation enegy for ^{119}Sn (upper panel) and ^{118}Sn (lower panel), according to the combinatorial BCS model. Also shown is how this quantity breaks down into neutron pairs (dashed line) and proton pairs (dashed-dotted line).

B. Level density

In Fig. 5, the level-density functions calculated by our model are compared with the experimental ones. We see that the model gives a very good representation of the level densities in the statistical area above 3 MeV for both isotopes. Not taking into account all collective bands known from literature, the model is not intended to reproduce the discrete level structure below the pair-breaking energy. The model also succeeds in reproducing the bump around ∼2.2–2.6 MeV for both isotopes, even though the onset of this bump in ^{119}Sn appears to be slightly delayed. Above ∼2.6 MeV, the step brings the level density to the same order of magnitude as the experimental values.

According to Eq. (8) and the relation between the intrinsic excitation energy U and the pair-gap parameters Δ_p and Δ_n, the log-scale slope of the level-density function is dependent on the pair-gap parameters. Figure 5 shows that the model reproduces well the slopes of the level densities for both isotopes. This supports the applied values of the pair-gap parameters.

C. Pair breaking

The pair-breaking process produces a strong increase in the level density. Typically, a single nucleon entropy of 1.6–1.7 k_B represents a factor of ∼5 more levels due to the valence neutron. Thus, the breaking of a Cooper pair represents about 25 more levels. Pair breaking is the most important mechanism for creating entropy in nuclei as function of excitation energy.

The average number of broken Cooper pairs per energy bin, $\langle N_{qp} \rangle$, is calculated as a function of excitation energy by the model, using the adopted pair-gap parameters as input values. All configurations obtained for each energy bin are traced, and their respective numbers of broken pairs are counted. The average number of broken pairs is also calculated separately for proton and neutron pairs. The result for ^{118,119}Sn is shown in Fig. 6.

Figure 6 shows that the first pair breaking for both ^{118,119}Sn is at an excitation energy around 2.2–2.6 MeV. That energy corresponds to the pair-breaking energy plus the extra energy needed to form the new configuration. The figure also shows

that, according to the model, the pair breakings here are only due to neutrons. The step in the average number of broken pairs is abrupt, and this number increases from 0 to almost 1. This means that there is a very high probability for the nucleus to undergo a neutron pair breaking at this energy. Provided that our values of the pair-gap parameters are reasonable, so this intense step in the number of broken neutron pairs in the model corresponds to the distinctive step in level density at ∼2.0 MeV in ^{119}Sn (see Sec. III); that step in level density is probably purely due to neutron pair breaking.

The increases in the average number of broken pairs are abrupt also for certain other excitation energies, namely around 5–6 MeV and 8–9 MeV, as shown in Fig. 6. Here, we predict increases of the number of levels caused by pair breaking, even though they are not necessarily visible with the applied experimental resolution. In between the abrupt pair breakings, the number of broken pairs is almost constant and close to integers. Saturation has been reached, and significantly more energy is needed for the next pair breaking.

Neutron pair breaking dominates over proton pair breaking for the energies studied. Even though there is a large shell gap for the protons, breaking of proton pairs also occurs, but then only for energies above the proton pair-breaking energy of $2\Delta_p$ plus the shell-gap energy. According to Fig. 6, proton pair-breaking contributes for excitation energies above 3.5 MeV in both isotopes. An increased number of broken proton pairs at higher energies is expected to lead to the level-density steps at high excitation energy being smeared out and becoming less distinctive, in accordance with the experimental findings of subsection III B.

Two effects due to the Pauli principle are notable in Fig. 6. In ^{119}Sn compared to ^{118}Sn, (i) the increases of the total average number of broken pairs occur at higher energies and (ii) the average number of broken proton pairs is generally higher. The explanation probably is that the valence neutron in ^{119}Sn to some extent hinders the neutron pair breaking. The presence of the valence neutron makes fewer states available for other neutrons, due to the Pauli principle. Therefore, in ^{119}Sn compared to ^{118}Sn, more energy is needed to break neutron pairs, and for a certain energy, proton pair breaking is more probable. Of course, an increase in the number of broken proton pairs leads to a corresponding decrease in the number of broken neutron pairs.

D. Collective effects

We have made use of the model to make a simple estimate of the relative impact on the level density of collective effects, i.e., rotations and vibrations, compared to that of the pair-breaking process. The enhancement factor of the collective effects is defined as

$$F_{\text{coll}}(E) = \frac{\rho(E)}{\rho_{\text{non-coll}}(E)}, \tag{19}$$

where $\rho_{\text{non-coll}}$ is the level-density function excluding collective effects.

Figure 7 shows the calculated level density with and without collective contributions from vibrations and from rotational bands for ^{119}Sn. The model prediction is assumed to be reasonably valid above ∼3 MeV of excitation energy. According to these simplistic calculations, the enhancement factor of collective effects F sharply decreases at the energies of the steps in the average number of broken quasiparticle pairs (see Fig. 6). For ^{119}Sn, we find that F decreases for excitation energies of approximately 2.5 and 6 MeV, where the average number of broken quasiparticle pairs increases from ∼0 to ∼1 and from ∼1 to ∼2, respectively. For the energies studied, the maximum value of F is about 10, found at $E \simeq 6$ MeV. For ^{118}Sn, the enhancement factor would be less than for ^{119}Sn, since this nucleus does not have unpaired valence neutrons.

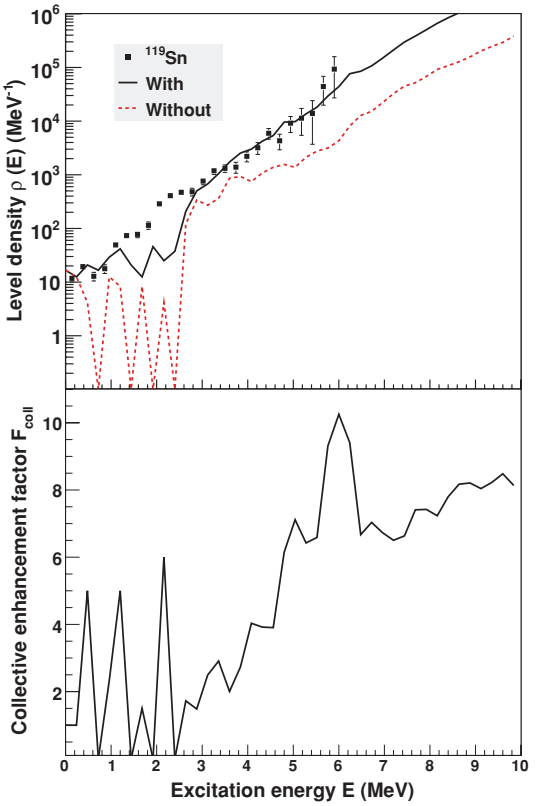

FIG. 7. (Color online) The impact of collective effects on the level density of ^{119}Sn according to the combinatorial BCS model. The upper panel shows experimental level density (data points) compared with model calculations with collective effects (solid line) and without collective effects (dashed line). The lower panel shows the corresponding enhancement factor of the collective effects, F_{coll} (linear scale).

As a conclusion, the collective phenomena of vibrations and rotations seem to have a significantly smaller impact on the creation of new levels than the nucleon pair-breaking process, which has an enhancement factor of typically about 25 for each broken pair.

E. Parity asymmetry

The parity asymmetry function α is defined as

$$\alpha = \frac{\rho_+ - \rho_-}{\rho_+ + \rho_-}, \tag{20}$$

where ρ_+ is the level density of positive-parity states, and ρ_- is the level density of the negative-parity states. The values of α range from -1 to $+1$. A system with $\alpha = -1$ is obtained for $\rho_+ = 0$, implying that all states have a negative parity. A system with $\alpha = 0$ has equally many states with positive as negative parity and is obtained for $\rho_- = \rho_+$.

The Nilsson scheme in Fig. 4 shows that the single-particle orbitals both above and below the neutron Fermi level are a mixture of positive and negative parities. In addition, each of these states may be the head of vibrational bands, for which the parity of the band may be opposite of that of the band head.

The parity asymmetry functions of ^{118,119}Sn are drawn in Fig. 8. For energies below the neutron pair-breaking energy approximately at 2.5 MeV, the even-odd isotope has a parity asymmetry function with large fluctuations between positive and negative values, while the even-even isotope has positive parities. This is as expected when vibrational bands of opposite parity are not introduced. (The zero parity of ^{118}Sn for certain low-energy regions is explained by the nonexistence of energy levels.)

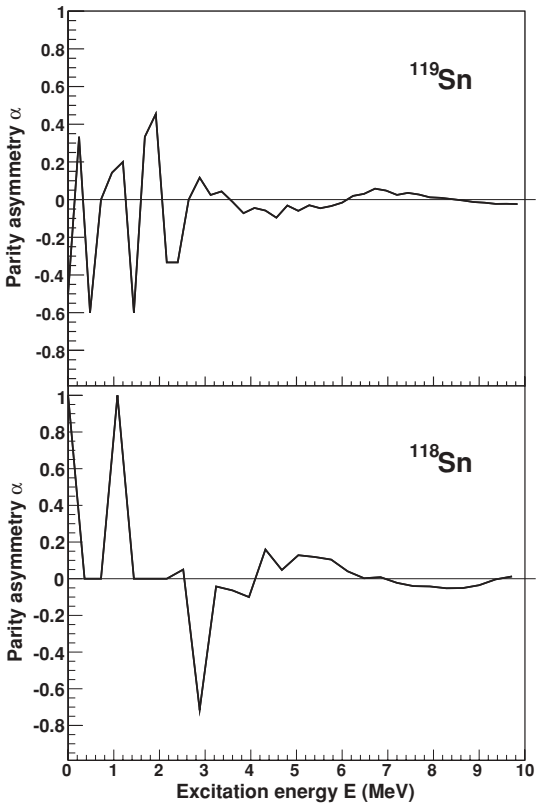

FIG. 8. The parity asymmetry function α, according to the combinatorial BCS model, shown as a function of excitation energy for ^{119}Sn (upper panel) and ^{118}Sn (lower panel).

Above the pair-breaking energies, the asymmetry functions begin to approach zero for both isotopes. This is also as expected, since we then have a group of valence nucleons that will randomly occupy orbitals of positive and negative parity and on average give an α close to zero. Above $\sim$4 MeV, the parity distributions of ^{118,119}Sn are symmetric with $\rho_+ \simeq \rho_-$. This is a gratifying property, since parity symmetry is an assumption in the Oslo method normalization procedure for both the level density and the γ-ray strength function (see Sec. V).

F. Spin distribution

The combinatorial BCS model determines the total spin I for each level from the relation:

$$I\,(I+1) = R\,(R+1) + \sum_{\Omega_\pi,\Omega_\nu} \Omega_\pi + \Omega_\nu, \tag{21}$$

from which the spin distribution of the level density ρ may be estimated.

The resulting spin distribution is compared with the theoretical spin distribution of Gilbert and Cameron in Eq. (4), using the same parametrization of the spin cut-off parameter as Eq. (5). Figure 9 shows the comparison for four different excitation energies: 5, 6, 7, and 8 MeV. The agreement is generally good. Hence, the spin calculation in Eq. (21), and the assumption of the rigid rotational parameter $A_{\rm rigid}$ obtained at S_n, are indicated to be reasonable assumptions. We also note from the figure that the average spin, $\langle I(E)\rangle$, is only slowly increasing with excitation energy, justifying the pseudo entropy definition introduced in Eq. (13).

V. γ-RAY STRENGTH FUNCTIONS

A. Normalization and experimental results

The γ-ray transmission coefficient $\mathcal{T}$, which is deduced from the experimental data, is related to the γ-ray strength function f by

$$\mathcal{T}(E_\gamma) = 2\pi \sum_{XL} E_\gamma^{2L+1} f_{XL}(E_\gamma), \tag{22}$$

where X denotes the electromagnetic character and L the multipolariy of the γ ray. The transmission coefficient $\mathcal{T}$ is normalized in slope α and in absolute value B according to Eq. (3). The slope was determined in Sec. III in the case of ^{118,119}Sn and in Ref. [1] in the case of ^{116}Sn. The absolute value normalization is yet to be determined. This is done using the literature values of the average total radiative width at the neutron separation energy, $\langle\Gamma_\gamma(S_n)\rangle$, which are measured for neutron capture reactions (n,γ).

The γ-ray transmission coefficient $\mathcal{T}$ is related to the average total radiative width $\langle\Gamma_\gamma(E, I, \pi)\rangle$ of levels with

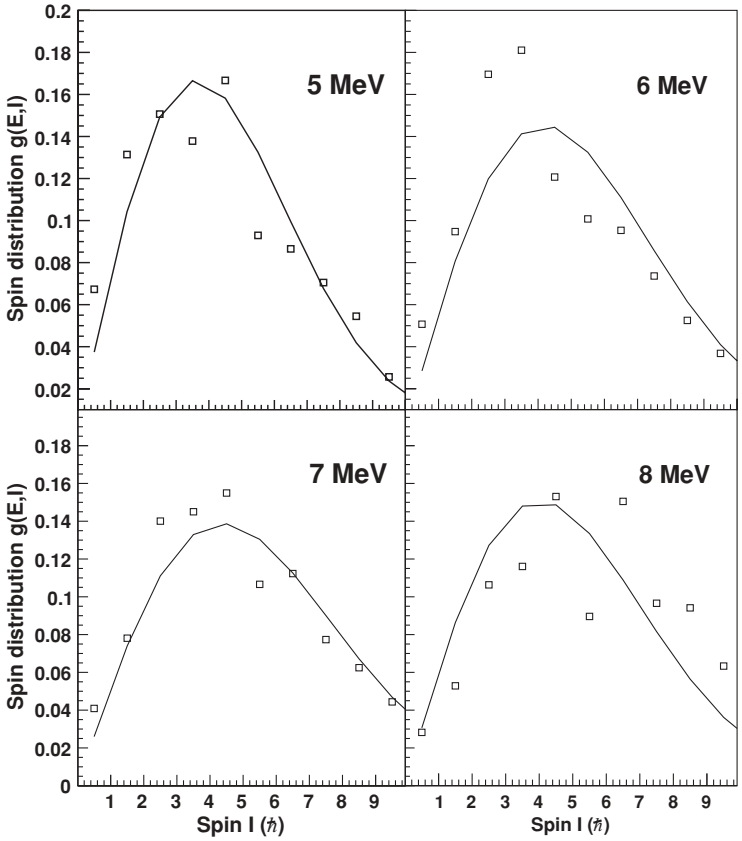

FIG. 9. Comparison of spin distributions in ^{118}Sn at different excitation energies. The open squares are calculated from the combinatorial BCS model in Eq. (21), while the solid lines are the predictions of Gilbert and Cameron in Eq. (4). The spin distributions are normalized to 1.

energy E, spin I, and parity π by [27]:

$$\langle \Gamma_\gamma(E,I,\pi)\rangle = \frac{1}{2\pi\rho(E,I,\pi)} \sum_{XL} \sum_{I_f,\pi_f} \int_{E_\gamma}^{E} dE_\gamma \mathcal{T}_{XL}(E_\gamma) \times \rho(E-E_\gamma, I_f, \pi_f). \quad (23)$$

The summations and integration are over all final levels of spin I_f and parity π_f that are accessible through a γ-ray transition categorized by the energy E_γ, electromagnetic character X, and multipolarity L.

For s-wave neutron resonances and assuming a major contribution from dipole radiation and parity symmetry for all excitation energies, the general expression in Eq. (23) will at S_n reduce to

$$\langle \Gamma_\gamma(S_n, I_t \pm 1/2, \pi_t)\rangle = \frac{B}{4\pi\rho(S_n, I_t \pm 1/2, \pi_t)} \times \int_0^{S_n} dE_\gamma \mathcal{T}(E_\gamma)\rho(S_n - E_\gamma) \times \sum_{J=-1}^{1} g(S_n - E_\gamma, I_t \pm 1/2 + J). \quad (24)$$

Here, I_t and π_t are the spin and parity of the target nucleus in the (n,γ) reaction. Indeed, the results from the combinatorial BCS model in Sec. IV supports the symmetry assumption of the parity distribution. The normalization constant B in Eq. (24) is determined [28] by replacing $\mathcal{T}$ with the experimental transmission coefficient, ρ with the experimental level density, g with the spin distribution given in Eq. (4), and $\langle \Gamma_\gamma(S_n)\rangle$ with its literature value.

The input parameters needed for determining the normalization constant B for ^{118,119}Sn are shown in Table III and taken from Ref. [10]. For ^{116}Sn, the level spacing $D_0(S_n)$ is not available in the literature. Therefore, $\rho(S_n)$ was estimated from systematics for the normalization of α in Ref. [1]. The value of D_0 in Table III is estimated from $\rho(S_n)$. Note that there was an error in the spin cut-off parameters $\sigma(S_n)$ of ^{116,117}Sn in Refs. [1,2]. The impact of this correction on the normalization of level densities and strength functions is very small. Moreover, updated values of $D_0(S_n)$ and $\langle \Gamma_\gamma(S_n)\rangle$ are now available for ^{117}Sn [10]. All the new normalization parameters for ^{116,117}Sn are presented in Table IV. The value of $\langle \Gamma_\gamma(S_n)\rangle$ of ^{116}Sn is taken from the indicated value in Ref. [10].

The resulting γ-ray strength functions of $^{116-119}$Sn are shown in Fig. 10. For all isotopes, it is clear that there is a

TABLE III. Input parameters for normalization of the γ-ray transmission coefficient $\mathcal{T}$ for ^{118,119}Sn.

Nucleus	I_t ($\hbar$)	$D_0(S_n)$ (eV)	$\langle\Gamma_\gamma(S_n)\rangle$ (meV)
^{119}Sn	0	700	45
^{118}Sn	1/2	61	117

change of the log-scale derivate at $E_\gamma \sim 4$ MeV, leading to a sudden increase of strength. Such an increase may indicate the onset of a resonance. The comparison in Fig. 10 of the new ^{117}Sn strength function with the earlier published one [2] confirms that correcting the $\sigma(S_n)$ and the $D_0(S_n)$ had only a minor impact on the normalization.

Figure 11 shows the four normalized strength functions of $^{116-119}$Sn together. They are all approximately equal except for ^{118}Sn, which has a lower absolute normalization than the others. This is surprising considering the quadrupole deformation parameter of ^{118}Sn ($\varepsilon_2 = 0.111$) being almost identical to that of ^{116}Sn ($\varepsilon_2 = 0.112$) [22]. In the following, we therefore multiply the strength of ^{118}Sn with a factor of 1.8 to get it on the same footing as the others. The values of $\rho(S_n)$ and the scaling parameter η (see also subsection III A) of these Sn isotopes are collected in Table V. For ^{118}Sn, the $\rho(S_n)$ may be expected to be larger, while η may be expected to be smaller. It would be desirable to remeasure both $D_0(S_n)$ and $\langle\Gamma_\gamma\rangle$ for this isotope, since the apparent wrong normalization of the strength function of ^{118}Sn depends on these parameters.

B. Pygmy resonance

Comparing our measurements with other experimental data makes potential resonances easier to localize. Experimental cross-section data $\sigma(E_\gamma)$ are converted to γ-ray strength $f(E_\gamma)$ through the relation:

$$f(E_\gamma) = \frac{1}{3\pi^2\hbar^2c^2}\left[\frac{\sigma(E_\gamma)}{E_\gamma}\right]. \tag{25}$$

Figure 12 shows the comparison of the Oslo strength functions of $^{116-119}$Sn with those of the photoneutron cross-section reactions ^{116,117}Sn(γ,n) from Utsunomiya *et al.* [29] and ^{119}Sn(γ,n) from Varlamov *et al.* [30], photoabsorption reactions $^{116-119}$Sn(γ,x) from Fultz *et al.* [31], $^{116-118}$Sn(γ,x) from Varlamov *et al.* [32], and $^{116-118}$Sn(γ,x) from Leprêtre *et al.* [33]. Clearly, the measurements on ^{117,119}Sn both from Oslo and from Utsunomiya *et al.* [29] independently indicate a resonance from the changes of slopes. For ^{116,118}Sn, the Oslo data clearly shows the presence of resonances. Hence, the resonance earlier observed in ^{117}Sn [2] is confirmed also in

TABLE IV. New normalization parameters for ^{116,117}Sn.

Nucleus	$\sigma(S_n)$	$D_0(S_n)$ (eV)	$\rho(S_n)$ (10^4 MeV^{-1})	$\langle\Gamma_\gamma(S_n)\rangle$ (meV)	η
^{117}Sn	4.58	450(50)	9.09(2.68)	52	0.43
^{116}Sn	4.76	59	40(20)	120	0.45

TABLE V. The Fermigas approximation for $\rho(S_n)_{\mathrm{BSFG}}$, the calculated $\rho(S_n)$, and the resulting scaling parameter η for $^{116-119}$Sn.

Nucleus	$\rho(S_n)_{\mathrm{BSFG}}$ (10^4 MeV^{-1})	$\rho(S_n)$ (10^4 MeV^{-1})	η
^{119}Sn	14	6.05(175)	0.44
^{118}Sn	65	38.4(86)	0.59
^{117}Sn	22	9.09(2.68)	0.43
^{116}Sn	89	40.0(20.0)	0.45

^{116,118,119}Sn. This resonance will be referred to as the pygmy resonance.

In order to investigate the experimental strength functions further, and in particular the pygmies, we have applied commonly used models for the giant electric dipole resonance (GEDR) and for the magnetic spin-flip resonance, also known as the giant magnetic dipole resonance (GMDR).

For the GEDR resonance, the generalized Lorentzian (GLO) model [34] is used. The GLO model is known to agree well both for low γ-ray energies, where we measure, and for the GEDR centroid at about 16 MeV. The strength function approaching a nonzero value for low E_γ is not a property specific for the Sn isotopes but has been the case for all nuclei studied at the OCL so far.

In the GLO model, the $E1$ strength function is given by [34]:

$$f_{E1}^{\mathrm{GLO}}(E_\gamma) = \frac{1}{3\pi^2\hbar^2c^2}\sigma_{E1}\Gamma_{E1} \times \left\{ E_\gamma \frac{\Gamma_{\mathrm{KMF}}(E_\gamma, T_f)}{\left({E_\gamma}^2 - {E_{E1}}^2\right)^2 + {E_\gamma}^2[\Gamma_{\mathrm{KMF}}(E_\gamma, T_f)]^2} + 0.7\frac{\Gamma_{\mathrm{KMF}}(E_\gamma = 0, T_f)}{{E_{E1}}^3}\right\} \tag{26}$$

in units of MeV^{-3}, where the Lorentzian parameters are the GEDR's centroid energy E_{E1}, width Γ_{E1} and cross section σ_{E1}. We use the experimental parameters of Fultz [31], shown in Table VI. The GLO model is temperature dependent from the incorporation of a temperature-dependent width Γ_{KMF}. This width is the term responsible for ensuring the nonvanishing GEDR at low excitation energy. It has been adopted from the Kadmenskii, Markushev, and Furman (KMF) model [35] and is given by:

$$\Gamma_{\mathrm{KMF}}(E_\gamma, T_f) = \frac{\Gamma_r}{{E_r}^2}\left({E_\gamma}^2 + 4\pi^2{T_f}^2\right), \tag{27}$$

in units of MeV.

Usually, T_f is interpreted as the nuclear temperature of the final state, with the commonly applied expression $T_f = \sqrt{U/a}$. On the other hand, we are assuming a constant temperature, i.e., the γ-ray strength function is independent of excitation energy. This approach is adopted for consistency with the Brink-Axel hypothesis (see Sec. II), where the strength function was assumed to be temperature independent. Moreover, we treat T_f as a free parameter in order to fit in the best possible way the theoretical strength prediction to the low energy measurements. The applied values of T_f are listed in Table VI.

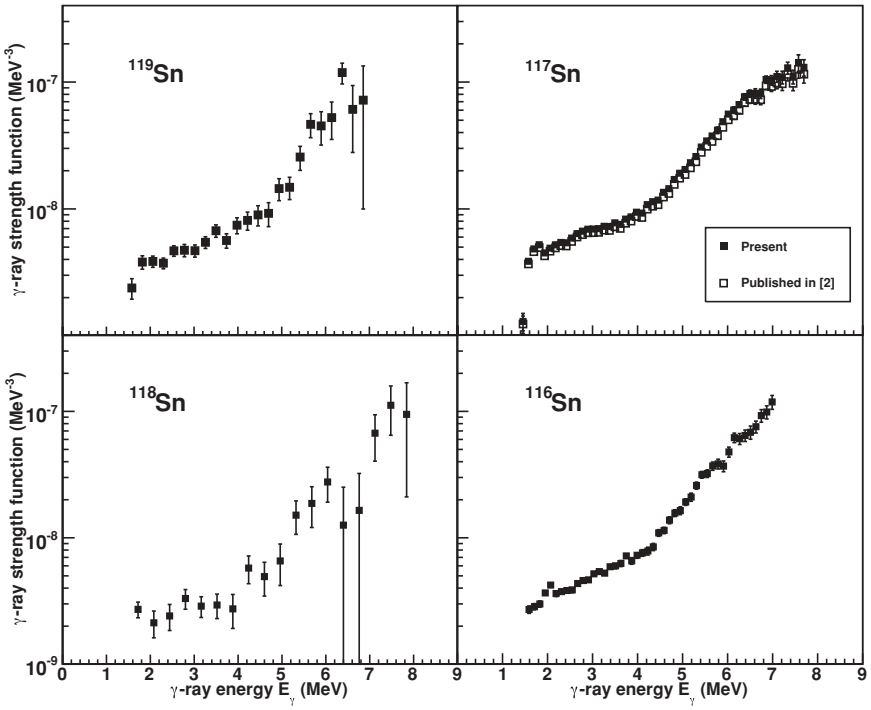

FIG. 10. Normalized γ-ray strength functions as functions of γ-ray energy. The upper panels show ^{119}Sn (left) and both present and previously published versions of ^{117}Sn (right). The energy bins 120 and 240 keV/ch for ^{117,119}Sn, respectively. The lower panels show ^{118}Sn (left) and ^{116}Sn (right) with the energy bins of 360 and 120 keV/ch, respectively.

The $M1$ spin-flip resonance is modeled with the functional form of a standard Lorentzian (SLO) [22]:

$$f_{M1}^{\mathrm{SLO}}(E_\gamma) = \frac{1}{3\pi^2\hbar^2c^2}\frac{\sigma_{M1}{\Gamma_{M1}}^2E_\gamma}{\left({E_\gamma}^2-{E_{M1}}^2\right)^2+{E_\gamma}^2{\Gamma_{M1}}^2}, \qquad (28)$$

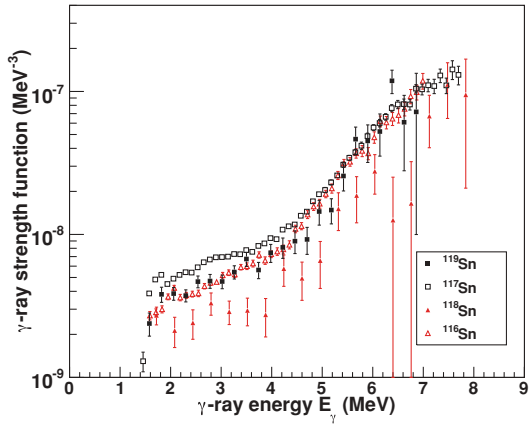

FIG. 11. (Color online) The four normalized strength functions of $^{116-119}$Sn shown together.

where the parameter E_{M1} is the centroid energy, Γ_{M1} the width, and σ_{M1} the cross section, of the GMDR. These Lorentzian parameters are predicted from the expressions in Ref. [22], with the results as shown in Table VI.

In the absence of any established theoretical prediction about the pygmy resonance, we found that the pygmy is satisfactorily reproduced by a Gaussian distribution [2]:

$$f_{\mathrm{pyg}}(E_\gamma) = C_{\mathrm{pyg}}\frac{1}{\sqrt{2\pi}\sigma_{\mathrm{pyg}}}\exp\left[\frac{-(E_\gamma-E_{\mathrm{pyg}})^2}{2{\sigma_{\mathrm{pyg}}}^2}\right], \qquad (29)$$

where C_{pyg} is the pygmy's normalization constant, E_{pyg} the energy centroid, and σ_{pyg} is the standard deviation. These parameters are treated as free. The total model prediction of the γ-ray strength function is then given by:

$$f_{\mathrm{total}} = f_{E1} + f_{M1} + f_{\mathrm{pyg}}. \qquad (30)$$

By adjusting the Gaussian pygmy parameters to make the best fit to the experimental data of $^{116-119}$Sn, we obtained the values as presented in Table VII. The pygmy fit of ^{117}Sn is updated and corresponds to the present normalization of the strength function. This pygmy fit also gave an excellent fit for ^{116}Sn. For ^{118,119}Sn, it was necessary to slightly reduce the values of T_f and σ_{pyg}. The similarity of the sets of parameters

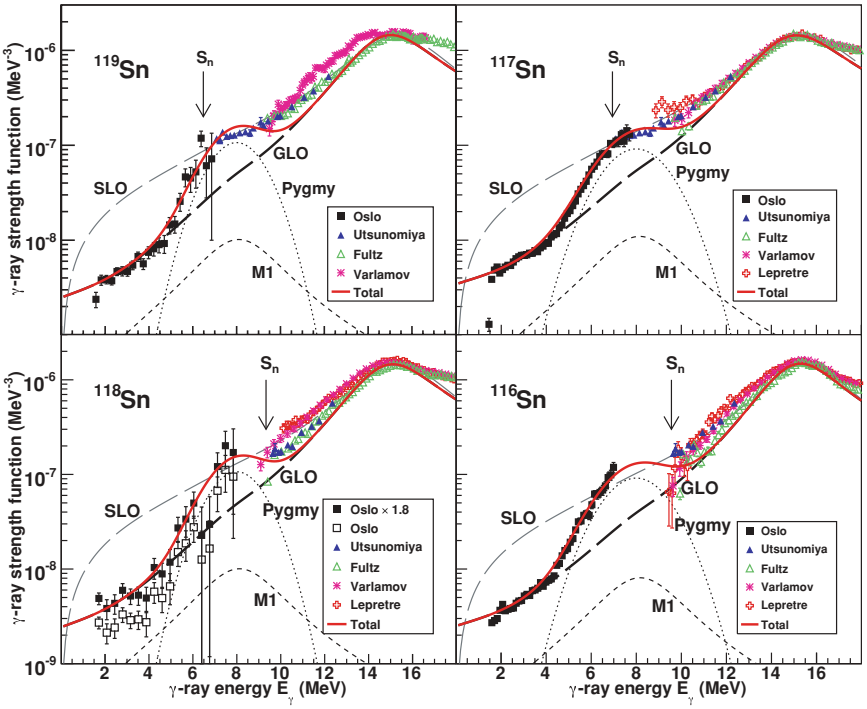

FIG. 12. (Color online) Comparison of theoretical predictions including pygmy fits with experimental measurements for $^{116-119}$Sn. The total strengths (solid lines) are modeled as Gaussian pygmy additions to the GLO ($E1+M1$) baselines. The SLO ($E1+M1$) baselines are also shown, failing to reproduce the measurements for low E_γ. The arrows indicate the neutron separation energies S_n. (Upper left panel) Comparison of theoretical predictions of ^{119}Sn with the Oslo measurements, ^{117}Sn(γ,n) from Utsunomiya *et al.* [29], ^{119}Sn(γ,x) from Fultz *et al.* [31], and ^{119}Sn(γ,n) from Varlamov *et al.* [30]. (Upper right panel) Comparison of theoretical predictions of ^{117}Sn with the Oslo measurements, ^{117}Sn(γ,n) from Utsunomiya *et al.* [29], ^{117}Sn(γ,x) from Fultz *et al.* [31], ^{117}Sn(γ,x) from Varlamov *et al.* [32], and ^{117}Sn(γ,x) from Leprêtre *et al.* [33]. (Lower left panel) Comparison of theoretical predictions of ^{118}Sn with the Oslo measurements multiplied with 1.8 (filled squares) (the measurements with the original normalization are also included as open squares), ^{116}Sn(γ,n) from Utsunomiya *et al.* [29], ^{118}Sn(γ,x) from Fultz *et al.* [31], ^{118}Sn(γ,x) from Varlamov *et al.* [32], and ^{118}Sn(γ,x) from Leprêtre *et al.* [33]. (Lower right panel) Comparison of theoretical predictions of ^{116}Sn with the Oslo measurements, ^{116}Sn(γ,n) from Utsunomiya *et al.* [29], ^{116}Sn(γ,x) from Fultz *et al.* [31], ^{116}Sn(γ,x) from Varlamov *et al.* [32], and ^{116}Sn(γ,x) from Leprêtre *et al.* [33].

for the different nuclei is gratifying. As is seen in Fig. 12, these theoretical predictions describe the measurements rather well.

The pygmy centroids of all the isotopes are estimated to be around 8.0(1) MeV. It is noted that an earlier experiment by Winhold *et al.* [36] using the (γ,n) reactions determined the pygmy centroids for ^{117,119}Sn to approximately 7.8 MeV, in agreement with our measurements. Extra strength has been added in the energy region of ∼4–11 MeV. The total integrated pygmy strengths are 30(15) MeV mb for all four isotopes. This constitutes 1.7(9)% of the classical Thomas-Reiche-Kuhn (TRK) sum rule, assuming all pygmy strength is $E1$. Even though these resonances are rather small compared

TABLE VI. Parameters used for the theoretical γ-ray strength functions of $^{116-119}$Sn. The value of T_f in ^{118}Sn has been found for the measured strength function multiplied by 1.8.

Nucleus	E_{E1} (MeV)	Γ_{E1} (MeV)	σ_{E1} (mb)	E_{M1} (MeV)	Γ_{M1} (MeV)	σ_{M1} (mb)	T_f (MeV)
^{119}Sn	15.53	4.81	253.0	8.34	4.00	0.963	0.40(1)
^{118}Sn	15.59	4.77	256.0	8.36	4.00	0.956	0.40(1)
^{117}Sn	15.66	5.02	254.0	8.38	4.00	1.04	0.46(1)
^{116}Sn	15.68	4.19	266.0	8.41	4.00	0.773	0.46(1)

TABLE VII. Empirical values of $^{116-119}$Sn pygmies Gaussian parameters, the integrated pygmy strengths, and the TRK values. For ^{118}Sn, the values have been found from fitting to the measured strength function multiplied by 1.8.

Nucleus	$C_{\rm pyg}$ (10^{-7}MeV^{-2})	$E_{\rm pyg}$ (MeV)	$\sigma_{\rm pyg}$ (MeV)	Integrated strength (MeV mb)	TRK value (%)
^{119}Sn	3.2(3)	8.0(1)	1.2(1)	30(15)	1.7(9)
^{118}Sn	3.2(3)	8.0(1)	1.2(1)	30(15)	1.7(9)
^{117}Sn	3.2(3)	8.0(1)	1.4(1)	30(15)	1.7(9)
^{116}Sn	3.2(3)	8.0(1)	1.4(1)	30(15)	1.7(9)

to the GEDR, they may have a non-negligible impact on nucleosynthesis in supernovas [37].

If one does not multiply the strength function of ^{118}Sn by 1.8 for the footing equality, then the pygmy of ^{118}Sn differs significantly from those of the other isotopes, and the total prediction is not able to follow as well the measurements for low E_γ. A pygmy fit of the original normalization does, however, give: $T_f = 0.28(2)$ MeV, $C_{\rm pyg} = 1.8(6) \times 10^{-7}$ MeV^{-2}, $E_{\rm pyg} = 8.0(2)$ MeV, and $\sigma_{\rm pyg} = 1.0(1)$ MeV. This represents a smaller pygmy, giving an integrated strength of 17(8) MeV mb and a TRK value of 1.0(5)%.

The commonly applied SLO was also tested as a model of the baseline and is included in Fig. 12. The SLO succeeds in reproducing the (γ, x) data but clearly fails for the low-energy strength measurements, both when it comes to absolute value and to shape. The same has been the case also for many other nuclei measured at the OCL. Therefore, we deem the SLO to be inadequate below the neutron threshold. Most likely, the pygmies of all the Sn isotopes are caused by the same phenomenon. It is still indefinite whether the Sn pygmy is of $E1$ or $M1$ character. Clarification would be of utmost importance.

Earlier studies indicate an $E1$ character of the Sn pygmy. Among these studies are the nuclear resonance fluorescence experiments (NRF) performed on ^{116,124}Sn [38] and ^{112,124}Sn [39] and the Coulomb dissociation experiments performed on $^{129-132}$Sn [40,41]. If the Sn pygmy is of $E1$ character, it may be consistent with the so-called $E1$ neutron skin oscillation mode, discussed in Refs. [42–44].

However, the possibility of an $M1$ character cannot be ruled out. Figure 4 shows that the Sn isotopes have their proton Fermi level located right in between the $g_{7/2}$ and $g_{9/2}$ orbitals, and their neutron Fermi level between $h_{11/2}$ and $h_{9/2}$. Thus, an enhanced $M1$ resonance may be due to proton $g_{7/2} \leftrightarrow g_{9/2}$ and neutron $h_{11/2} \leftrightarrow h_{9/2}$ magnetic spin-flip transitions. The existence of an $M1$ resonance in this energy region has been indicated in an earlier experimental study via the proton inelastic scattering experiment on ^{120,124}Sn [45].

VI. CONCLUSIONS

The level-density functions of ^{118,119}Sn and the γ-ray strength functions of ^{116,118,119}Sn have been measured using the (^{3}He, $\alpha\gamma$) and (^{3}He,^{3}He$'\gamma$) reactions and the Oslo method.

The level-density function of ^{119}Sn shows pronounced steps for excitation energies below ∼4 MeV. This may be explained by the fact that Sn has a closed proton shell so only neutron pairs are broken at low energy. Without any proton pair breaking smearing out the level-density function, the steps from neutron pair breaking remain distinctive. The entropy has been deduced from the experimental level-density functions, with a mean value of the single neutron entropy in ^{119}Sn determined to $1.7 \pm 0.2\ k_B$. These findings are in good agreement with those of ^{116,117}Sn.

A combinatorial BCS model has been used to extract nuclear properties from the experimental level density. The number of broken proton and neutron pairs as a function of excitation energy is deduced, showing that neutron pair breaking is the most dominant pair-breaking process for the entire energy region studied. The enhancement factor of collective effects on level density contributes a maximum factor of about 10, which is small compared to that of pair breaking. The parity distributions are found to be symmetric above ∼4 MeV of excitation energy.

In all the $^{116-119}$Sn strength functions, a significant enhancement is observed in the energy region of $E_\gamma \simeq$ 4–11 MeV. The integrated strength of the resonances correspond to 1.7(9)% of the TRK sum rule. These findings are in agreement with the conclusions of earlier studies.

ACKNOWLEDGMENTS

The authors thank E. A. Olsen, J. Wikne, and A. Semchenkov for excellent experimental conditions. The funding of this research from The Research Council of Norway (Norges forskningsråd) is gratefully acknowledged. This work was supported in part by the US Department of Energy Grant Nos. DE-FG52-09-NA29640 and DE-FG02-97-ER41042.

[1] U. Agvaanluvsan, A. C. Larsen, M. Guttormsen, R. Chankova, G. E. Mitchell, A. Schiller, S. Siem, and A. Voinov, Phys. Rev. C **79**, 014320 (2009).
[2] U. Agvaanluvsan, A. C. Larsen, R. Chankova, M. Guttormsen, G. E. Mitchell, A. Schiller, S. Siem, and A. Voinov, Phys. Rev. Lett. **102**, 162504 (2009).
[3] M. Guttormsen, T. S. Tveter, L. Bergholt, F. Ingebretsen, and J. Rekstad, Nucl. Instrum. Methods A **374**, 371 (1996).
[4] M. Guttormsen, T. Ramsøy, and J. Rekstad, Nucl. Instrum. Methods A **255**, 518 (1987).
[5] A. Schiller, L. Bergholt, M. Guttormsen, E. Melby, J. Rekstad, and S. Siem, Nucl. Instrum. Methods A **447**, 498 (2000).
[6] A. Bohr and B. Mottelson, *Nuclear Structure* (Benjamin, New York, 1969), Vol. I.
[7] D. M. Brink, Ph.D. thesis, Oxford University (1955).
[8] P. Axel, Phys. Rev. **126**, 671 (1962).

[9] S. F. Mughabghab, *Atlas of Neutron Resonances*, 5th ed. (Elsevier Science, Amsterdam, 2006).
[10] R. Capote *et al.*, *RIPL-3—Reference Input Parameter Library for Calculation of Nuclear Reactions and Nuclear Data Evaluations*, Nucl. Data Sheets **110**, 3107 (2009). Available online at [http://www-nds.iaea.org/RIPL-3/].
[11] T. von Egidy, H. H. Schmidt, and A. N. Behkami, Nucl. Phys. A **481**, 189 (1988).
[12] A. Gilbert and A. G. W. Cameron, Can. J. Phys. **43**, 1446 (1965).
[13] G. Audi and A. H. Wapstra, Nucl. Phys. A **595**, 409 (1995).
[14] J. Dobaczewski, P. Magierski, W. Nazarewicz, W. Satuła, and Z. Szymański, Phys. Rev. C **63**, 024308 (2001).
[15] N. U. H. Syed, M. Guttormsen, F. Ingebretsen, A. C. Larsen, T. Lönnroth, J. Rekstad, A. Schiller, S. Siem, and A. Voinov, Phys. Rev. C **79**, 024316 (2009).
[16] R. Firestone and V. S. Shirley, *Table of Isotopes*, 8th ed. (Wiley, New York, 1996), Vol. II.
[17] A. Schiller *et al.*, Phys. Rev. C **68**, 054326 (2003).
[18] M. Guttormsen, M. Hjorth-Jensen, E. Melby, J. Rekstad, A. Schiller, and S. Siem, Phys. Rev. C **63**, 044301 (2001).
[19] A. C. Larsen *et al.*, Phys. Rev. C **76**, 044303 (2007).
[20] N. U. H. Syed *et al.*, Phys. Rev. C **80**, 044309 (2009).
[21] M. Guttormsen, U. Agvaanluvsan, E. Algin, A. Bürger, A. C. Larsen, G. E. Mitchell, H. T. Nyhus, S. Siem, H. K. Toft, and A. Voinov, EPJ Web of Conferences **2**, 04001 (2010).
[22] T. Belgya *et al.*, *Handbook for Calculations of Nuclear Reaction Data, RIPL-2* (IAEA, Vienna, 2006). Available online at [http://www-nds.iaea.org/RIPL-2/].
[23] J. Y. Zhang, N. Xu, D. B. Fossan, Y. Liang, R. Ma, and E. S. Paul, Phys. Rev. C **39**, 714 (1989).
[24] J. Bardeen, L. N. Cooper, and J. R. Schrieffer, Phys. Rev. **108**, 1175 (1957).
[25] K. S. Krane, *Introductory Nuclear Physics* (John Wiley & Sons, 1988).
[26] Y. Alhassid, S. Liu, and H. Nakada, Phys. Rev. Lett. **99**, 162504 (2007).
[27] J. Kopecky and M. Uhl, Phys. Rev. C **41**, 1941 (1990).
[28] A. Voinov, M. Guttormsen, E. Melby, J. Rekstad, A. Schiller, and S. Siem, Phys. Rev. C **63**, 044313 (2001).
[29] H. Utsunomiya *et al.*, Phys. Rev. C **80**, 055806 (2009).
[30] V. V. Varlamov, B. S. Ishkhanov, V. N. Orlin, and V. A. Tchetvertkova, Moscow State Univ. Inst. of Nucl. Phys. Reports No. 2009, p. 3/847 (2009).
[31] S. C. Fultz, B. L. Berman, J. T. Coldwell, R. L. Bramblett, and M. A. Kelly, Phys. Rev. **186**, 1255 (1969).
[32] V. V. Varlamov, N. N. Peskov, D. S. Rudenko, and M. E. Stepanov, Vop. At. Nauki i Tekhn., Ser. Yadernye Konstanty 1–2 (2003).
[33] A. Leprêtre, H. Beil, R. Bergere, P. Carlos, A. De Miniac, A. Veyssiere, and K. Kernbach, Nucl. Phys. A **219**, 39 (1974).
[34] J. Kopecky and R. E. Chrien, Nucl. Phys. A **468**, 285 (1987).
[35] S. G. Kadmenskii, V. P. Markushev, and V. I. Furman, Yad. Fiz. **37**, 277 (1983) [Sov. J. Nucl. Phys. **37**, 165 (1983)].
[36] E. J. Winhold, E. M. Bowey, D. B. Gayther, and B. H. Patrick, Phys. Lett. B **32**, 607 (1970).
[37] S. Goriely, Phys. Lett. B **436**, 10 (1998).
[38] K. Govaert, F. Bauwens, J. Bryssinck, D. De Frenne, E. Jacobs, W. Mondelaers, L. Govor, and V. Y. Ponomarev, Phys. Rev. C **57**, 2229 (1998).
[39] A. Tonchev (private communication).
[40] P. Adrich *et al.*, Phys. Rev. Lett. **95**, 132501 (2005).
[41] Klimkiewicz *et al.*, Phys. Rev. C **76**, 051603(R) (2007).
[42] P. Van Isacker, M. A. Nagarajan, and D. D. Warner, Phys. Rev. C **45**, R13 (1992).
[43] N. Paar, P. Ring, T. Niksic, and D. Vretenar, Phys. Rev. C **67**, 034312 (2003).
[44] D. Sarchi *et al.*, Phys. Lett. B **601**, 27 (2004).
[45] C. Djalali, N. Marty, M. Morlet, A. Willis, J. C. Jourdain, N. Anantaraman, G. M. Crawley, A. Galonsky, and P. Kitching, Nucl. Phys. A **388**, 1 (1982).

7.2 Article 2: Evolution of the pygmy dipole resonance in Sn isotopes

The experimental level density and the γ-ray strength function of ^{121,122}Sn are extracted with the Oslo method using the (^{3}He,$\alpha\gamma$) and (^{3}He,^{3}He$'\gamma$) reactions. The level densities of ^{121,122}Sn display step-like structures, interpreted as due to neutron pair breaking.

An enhancement in both strength functions, compared to the GLO, is observed in our measurements for $E_\gamma \gtrsim 5.2$ MeV. This enhancement is compatible with a resonance centered at $E_\gamma = 8.4(1)$ and $8.6(2)$ MeV for ^{121,122}Sn, respectively, and with an integrated strength corresponding to 1.8^{+1}_{-5}% of the TRK sum rule for both isotopes. Similar pygmy resonances were also found in $^{116-119}$Sn (see Ref. [6] and Article 1). The centroid energies of the resonances earlier found in ^{118,119}Sn (in Article 1) are corrected from $E_\gamma = 8.0(1)$ MeV for both isotopes to $8.2(1)$ MeV.

Experimental (n,γ) cross sections are well reproduced when including the pygmy resonance. Including the pygmy resonance gives significantly better agreement than standard models of radiative strength (the GLO and the standard Lorentzian (SLO) model [47]).

The evolution of the pygmy resonance as a function of neutron number in the isotopes $^{116-122}$Sn is discussed. The findings are that the centroid energy of the resonance increases from $E_\gamma = 8.0(1)$ in ^{116}Sn to 8.6(2) MeV in ^{122}Sn, while no significant difference in integrated strength can be seen. These observations are in contradiction to theoretical predictions.

Evolution of the pygmy dipole resonance in Sn isotopes

H. K. Toft[1*], A. C. Larsen[1], A. Bürger[1], M. Guttormsen[1], A. Görgen[1], H. T. Nyhus[1], T. Renstrøm[1], S. Siem[1], G. M. Tveten[1], and A. Voinov[2].
[1]*Department of Physics, University of Oslo, N-0316 Oslo, Norway, and*
[2]*Department of Physics and Astronomy, Ohio University, Athens, Ohio 45701, USA*
(Dated: February 17, 2011)

Nuclear level density and γ-ray strength functions of ^{121,122}Sn below the neutron separation energy are extracted with the Oslo method using the (^{3}He,^{3}He$'\gamma$) and (^{3}He,$\alpha\gamma$) reactions. The level densities of ^{121,122}Sn display step-like structures, interpreted as signatures of neutron pair breaking. An enhancement in both strength functions, compared to standard models for radiative strength, is observed in our measurements for $E_\gamma \gtrsim 5.2$ MeV. This enhancement is compatible with pygmy resonances centered at $\approx 8.4(1)$ and $\approx 8.6(2)$ MeV, respectively, and with integrated strengths corresponding to $\approx 1.8^{+1}_{-5}$% of the classical Thomas-Reiche-Kuhn sum rule. Similar resonances were also seen in $^{116-119}$Sn. Experimental neutron-capture cross reactions are well reproduced by our pygmy resonance predictions, while standard strength models are less successful. The evolution as a function of neutron number of the pygmy resonance in $^{116-122}$Sn is described as a clear increase of centroid energy from 8.0(1) to 8.6(2) MeV, but with no observable difference in integrated strengths.

PACS numbers: 21.10.Ma, 24.10.Pa, 24.30.Gd, 27.60.+j

I. INTRODUCTION

The level density and the γ-ray strength function are average quantities describing properties of atomic nuclei. The nuclear level density is defined as the number of energy levels per unit of excitation energy, while the γ-ray strength function may be defined as the reduced average transition probability as a function of γ-ray energy. The strength function characterizes average electromagnetic properties of excited nuclei.

The level density and the strength function are important for many aspects of fundamental and applied nuclear physics. They are used for the calculation of cross sections and neutron-capture (n,γ) reactions rates, which are input parameters in, e.g., reactor physics, nuclear waste management, and astrophysical models describing the nucleosynthesis in stars.

Tin and other heavier neutron-rich nuclei are often found display a smaller resonance for γ-ray energies below the Giant Electric Dipole Resonance (GEDR). The existence of even a small resonance close to the neutron separation energy may have large consequences in nuclear astrophysics on the calculated distribution of elemental abundance.

This article presents the measurements of the level densities and γ-ray strength functions in ^{121,122}Sn for energies below the neutron separation energy, as well as a systematic study of the evolution of the pygmy resonances in $^{116-119,121,122}$Sn. The experimental results on $^{116-119}$Sn are published in Refs. [1–3]. All experiments have been performed at the Oslo Cyclotron Laboratory (OCL).

The experimental set-up is described in Sec. II and the data analysis in Sec. III. The level densities of ^{121,122}Sn are presented in Sec. IV and the strength functions in Sec. V. Section VI discusses the pygmy resonance evolution and the impacts from the pygmy resonances on the (γ,n) cross sections. Conclusions are drawn in Sec. VII.

II. EXPERIMENTAL SET-UP

The self-supporting ^{122}Sn target was enriched to 94% and had a mass thickness of 1.43 mg/cm^2. For five days the target was exposed to a 38-MeV ^{3}He beam with an average current of $\approx$ 0.2 nA. The reaction channels studied were ^{122}Sn(^{3}He,^{3}He$'\gamma$)^{122}Sn and ^{122}Sn(^{3}He,$\alpha\gamma$)^{121}Sn.

Particle-γ coincidences were recorded with 64 Si particle $\Delta E - E$ telescopes and 28 collimated NaI(Tl) γ-ray detectors. The ΔE and E detector thicknesses are approximately 130 μm and 1550 μm, respectively. These detectors cover the angles of $40-54^\circ$ with respect to the beam axis, and they have a total solid-angle coverage of $\approx$ 9% out of 4π. The NaI detectors are distributed on a sphere and constitute the CACTUS multidetector system [4]. The detection efficiency is 15.2%, and the resolution of a single NaI detector is $\approx$ 6% FWHM, at the γ energy of 1332 keV.

III. DATA ANALYSIS

The measured energy of the ejectile is calculated into excitation energy of the residual nucleus. The γ-ray spectra are unfolded with the known response functions of CACTUS and by the use of the Compton subtraction method [5]. The first generation γ-ray spectra are extracted by the subtraction procedure described in Ref. [6].

The first-generation γ-ray spectra are arranged in a two-dimensional matrix $P(E,E_\gamma)$, shown for ^{122}Sn in Fig. 1. The entries of the matrix give the probabilities $P(E,E_\gamma)$ that a γ-ray of energy E_γ is emitted from a bin of excitation energy E.

The empty region for low γ energy and higher excitation energies in Fig. 1 is explained by too strong subtraction caused by the strongly populated states (yellow/red spots) found for

*h.k.toft@fys.uio.no

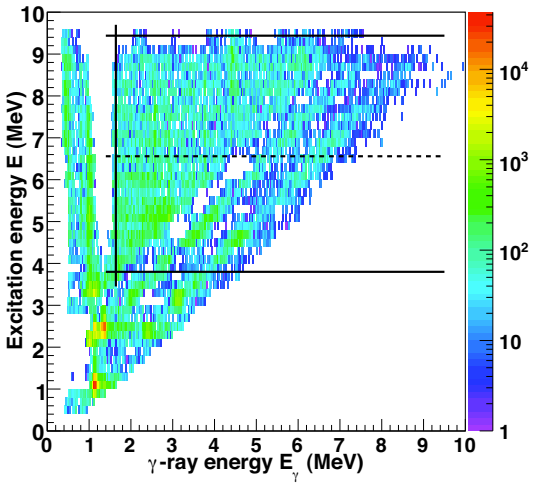

FIG. 1: (Color online) The first-generation matrix P of ^{122}Sn. The solid lines indicate the region for the data used in the Oslo method ($E_\gamma > 1.6$ MeV, $3.8 < E < 9.4$ MeV). The dashed line ($E = 6.6$ MeV) is the middle between the upper and lower ranges in excitation energy.

low γ-energy and lower excitation energies. Too few first-generation γ's remain for low γ energy and higher excitation energies, which has made the first-generation method not work very well (see Ref. [7]). We select and proceed with the region between the solid lines. It is commented that the diagonal valleys and ridges are made up by strong first-generation transitions to the ground and first-excited states.

The selected region of the first generation matrix P is factorized into the level density ρ and the radiative transmission coefficient $\mathcal{T}$ [8]:

$$P(E, E_\gamma) \propto \rho(E - E_\gamma)\mathcal{T}(E_\gamma). \quad (1)$$

The factorization into two independent components is justified for nuclear reactions leading to a compound state prior to a subsequent γ decay [9]. The factorization is performed by an iterative procedure [8] where the independent functions ρ and $\mathcal{T}$ are adjusted until a global χ^2 minimum with the experimental $P(E, E_\gamma)$ is reached.

The quality of the factorization of level density and strength function is illustrated for ^{122}Sn in Fig. 2. At example excitation energies (indicated on the panels), the entries of the P matrix obtained from the χ^2-fitted output functions ρ and $\mathcal{T}$ using Eq. (1) are compared to those of the experimental P matrix. The fitted output (solid line) agrees well with experimental data. It is noted that in some of the panels, the fitted curves are significantly lower than the experimental data points (For $E = 4.1$ MeV: the transition to the ground state; for $E = 4.8$ MeV: the transition to the first-excited state). This is probably explained by the fit adjusting the entire matrix, and not just these example excitation energies.

The Brink-Axel hypothesis [10, 11] states that the GEDR and any other collective excitation mode built on excited states have the same properties as those built on the ground state. Equation 1 shows that the transmission coefficient is assumed to be independent of excitation energy E, which is a consequence of the Brink-Axel hypothesis.

Figure 3 shows an investigation of this assumption for ^{122}Sn, which is of special concern due to some clear structures in the strength function. We divide the selected region of the P matrix into two parts (separated by the dashed line in Fig. 1), which are two independent data sets. Figure 3 displays the strength functions derived from the lower and upper part, as well as from the total region. The strength functions, proportional to $\mathcal{T}/{E_\gamma}^3$, are not normalized and are shown in arbitrary units. As the clear structures are found at the same locations for the two independent data sets, the $\mathcal{T}$ is indeed found to be approximately independent of excitation energy.

The adjustment to Eq. (1) determines only the functional forms of ρ and $\mathcal{T}$. These two functions are invariant under the following transformations [8]:

$$\tilde{\rho}(E - E_\gamma) = A \exp\left[\alpha\left(E - E_\gamma\right)\right] \rho(E - E_\gamma), \quad (2)$$

$$\tilde{\mathcal{T}}(E_\gamma) = B \exp\left(\alpha E_\gamma\right) \mathcal{T}(E_\gamma). \quad (3)$$

The parameters A and B define the correction to the absolute values of the functions ρ and $\mathcal{T}$, respectively, while the parameter α defines their common correction to the log-scale slope. These parameters will be determined in Secs. IV and V.

IV. LEVEL DENSITIES

The constants A and α needed to normalize the experimental level density ρ, are determined using literature values of the known discrete energy levels at low energy and of the level spacing D at the neutron separation energy S_n. We use the same normalization procedure as in Refs. [1–3], in order to have a common ground for comparison.

The chosen model is the back-shifted Fermi gas (BSFG) model, published by von Egidy *et al.* in 1988 [12]. The level density at the neutron separation energy $\rho(S_n)$ is calculated from known values of the s-wave level spacing D_0 [8]:

$$\rho(S_n) = \frac{2\sigma^2}{D_0} \cdot \left\{(I_t + 1)\exp\left[\frac{-(I_t + 1)^2}{2\sigma^2}\right] + I_t \exp\left[\frac{-{I_t}^2}{2\sigma^2}\right]\right\}^{-1}, \quad (4)$$

where I_t is the target spin, and where the spin-cutoff parameter σ is also evaluated at S_n. The spin-cutoff parameter is defined as $\sigma^2 = 0.0888\, A^{2/3} aT$, where A is the mass number of the isotope, and T is the nuclear temperature given by $T = \sqrt{U/a}$. Here, U is the nucleus intrinsic excitation energy, and a is the level-density parameter. The parameterization used for a is $a = 0.21\, A^{0.87}$ MeV^{-1}. The parameterization of U is $U = E - E_{\rm pair} - C_1$, where the pairing energy $E_{\rm pair}$ is calculated

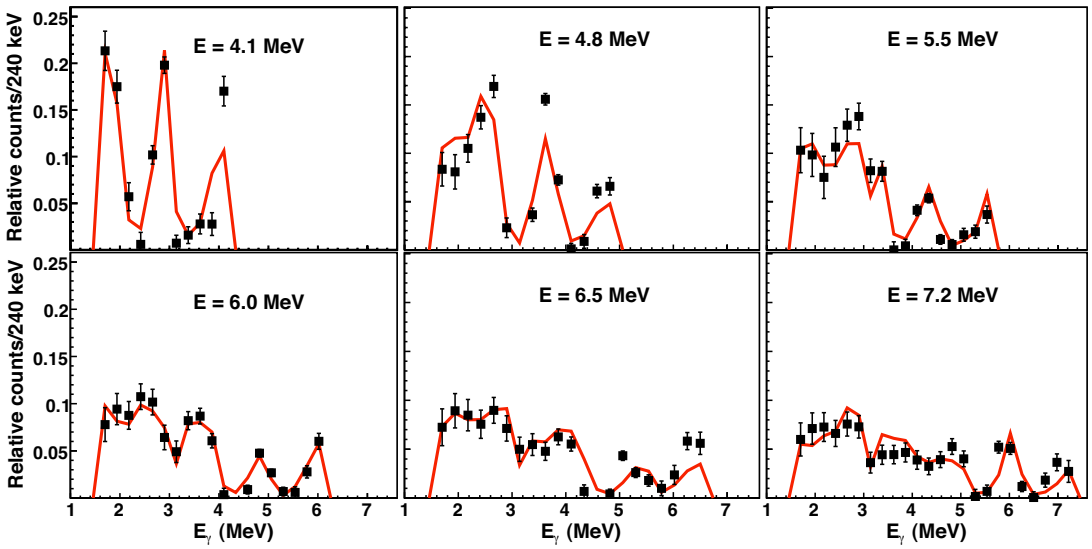

FIG. 2: (Color online) Comparison between experimental (squares) and χ^2 fitted (solid lines) P matrix for ^{122}Sn. The energy bins have been compressed to 240 keV/ch in E and in E_γ. While the panels show the results for the indicated example excitation energies, the fit has been performed globally for the entire region of the P matrix that has been selected for the analysis (see Fig. 1).

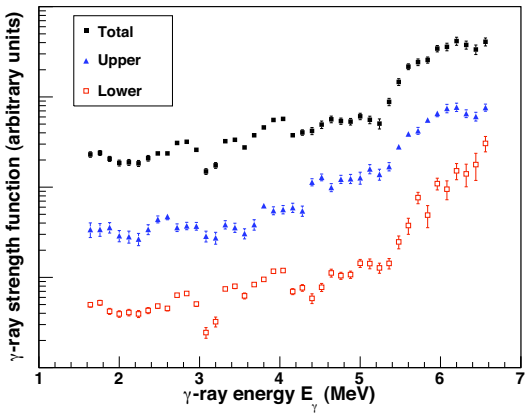

FIG. 3: (Color online) Comparison of unnormalized γ-ray strength functions (arbitrary units) for ^{122}Sn. The shown strength functions are derived from the independent data sets of the upper and lower part of the selected region of the P matrix, as well as from the total selected region for comparison.

from the proton and neutron pair-gap parameters: $E_{\rm pair} = \Delta_{\rm p} + \Delta_{\rm n}$, and where the back-shift parameter C_1 is defined as $C_1 = -6.6\,A^{-0.32}$.

The experimental value of D_0 for ^{121}Sn is found in Ref. [13] and is used to calculate $\rho(S_n)$ using the input parameters listed in Tab. I. The pair-gap parameters are evaluated from even-odd mass differences [14] according to the method of Ref. [15].

No experimental value exists for D_0 of ^{122}Sn, and we estimate $\rho(S_n)$ for this isotope from systematics. Figure 4 shows $\rho(S_n)$ calculated from the experimental values of D_0 according to Eq. (4) for all available Sn isotopes as a function of S_n. The values of D_0 have been taken from Ref. [13]. We have also calculated $\rho(S_n)$ according to the prediction of the BSFG model [16]:

$$\rho(E)_{\rm BSFG} = \frac{\exp\left(2\sqrt{aU}\right)}{12\sqrt{2}\,a^{1/4}\,U^{5/4}\,\sigma}\,, \qquad (5)$$

with the above-listed parameterizations. The theoretical value of $\rho(S_n)$, multiplied with a common factor of 0.4, are shown in Fig. 4 together with the experimental values. From the trends appearing in the figure, we estimate $\rho(S_n)$ for ^{122}Sn to 2.0(10)$\cdot 10^5$ MeV^{-1} (50% uncertainty assumed, see Tab. I).

While we would like to normalize to $\rho(S_n)$, our experimental data only cover the excitation energy region from 0 to S_n-2 MeV, due to methodical limitations. We therefore make an interpolation from our measurements to S_n using the BSFG prediction in Eq. (5). The prediction is multiplied by a scaling parameter η (see Tab. I) in order to agree with the normaliza-

TABLE I: Input parameters and the resulting values for the calculation of the normalization value $\rho(S_n)$.

Nucleus	S_n (MeV)	D_0 (eV)	a (MeV^{-1})	C_1 (MeV)	Δ_n (MeV)	Δ_p (MeV)	$\sigma(S_n)$	$\rho(S_n)$ (10^4 MeV^{-1})	η
^{121}Sn	6.17	1250(200)	13.62	-1.42	0	0.82	4.57	3.42(86)	0.25
^{122}Sn	8.81	62(31)[a]	13.72	-1.42	1.32	1.12	4.75	20(10)[a]	0.42

[a] Estimated from systematics.

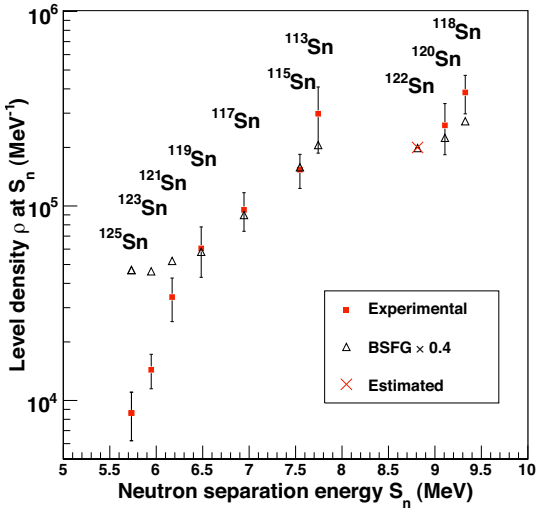

FIG. 4: (Color online) Estimation (cross) of the experimental value of $\rho(S_n)$ for ^{122}Sn from systematics. Experimental values (squares) and global BSFG predictions (triangles) for $\rho(S_n)$ are shown for various Sn isotopes as function of S_n. (See text.)

tion value $\rho(S_n)$:

$$\rho(E)_{\mathrm{BSFG}} \rightarrow \eta\,\rho(E)_{\mathrm{BSFG}}\,. \qquad (6)$$

Figure 5 shows the normalized level densities of ^{121,122}Sn. The arrows indicate the two regions that have been used for normalization to the discrete level density and to the normalization value $\rho(S_n)$. As expected, the level density function of ^{121}Sn is very similar to those of the other even-odd nuclei ^{117,119}Sn, while the level density function of ^{122}Sn is very similar to those of the even-even nuclei ^{116,118}Sn [1, 3].

The level densities of ^{121,122}Sn in Fig. 5 show step-like structures, a feature also seen in $^{116-119}$Sn [1, 3]. In ^{121,122}Sn, two pronounced bumps are seen in the region of $\approx 0.8 - 1.4$ MeV and $\approx 1.8 - 2.4$ MeV. The corresponding steps are located at ≈ 1.0 and ≈ 2.0 MeV, respectively. The second step is very abrupt, especially in the even-even nucleus, and the step is followed by a significantly higher level density. The second step is therefore a candidate for the neutron pair-breaking process in ^{121,122}Sn. Such neutron pair-breaking bumps are especially distinctive in Sn isotopes since the proton number

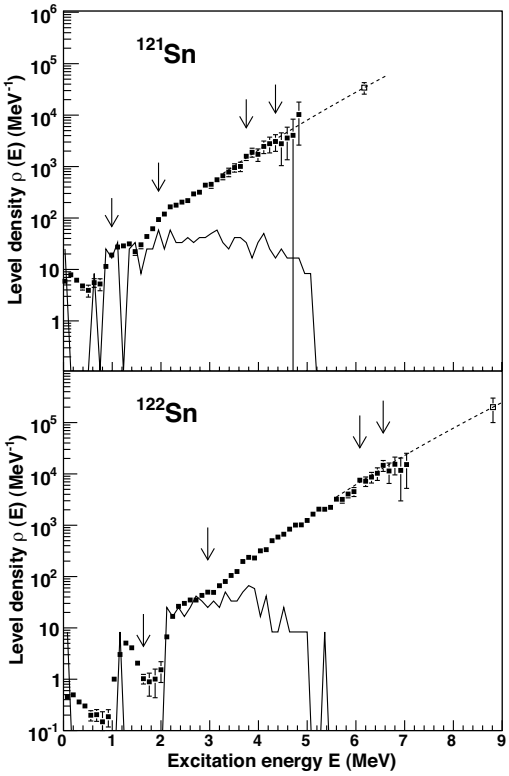

FIG. 5: Normalized level densities of ^{121,122}Sn (filled squares) as a function of excitation energy with energy bins of 120 keV/ch. The solid lines represent the discrete level densities obtained from spectroscopy. The dashed line in both panels is the BSFG prediction, which is used for interpolation, scaled with η to coincide with $\rho(S_n)$ (open square). The value of $\rho(S_n)$ has been calculated from neutron resonance data. The arrows indicate the two regions used for normalization.

is magic (Z = 50), making proton pair breaking occur only at relatively higher excitation energies. A detailed discussion of the pair-breaking process has been given in Refs. [1, 3].

V. GAMMA-RAY STRENGTH FUNCTIONS

The γ-ray transmission coefficient $\mathcal{T}$, which is deduced from the experimental data, is related to the γ-ray strength function f by

$$\mathcal{T}(E_\gamma) = 2\pi \sum_{XL} E_\gamma^{2L+1} f_{XL}(E_\gamma)\,, \tag{7}$$

where X denotes the electromagnetic character and L the multipolarity of the γ ray. The transmission coefficient $\mathcal{T}$ is normalized in log-scale slope (α) and in absolute value (B) (see Eq. (3)).

For s-wave neutron resonances and assuming a major contribution from dipole radiation and parity symmetry for all excitation energies, the expression for the average radiative width $\left\langle \Gamma_\gamma(E, I, \pi) \right\rangle$ will at S_n reduce to [17]:

$$\begin{aligned} &\left\langle \Gamma_\gamma(S_n, I_t \pm 1/2, \pi_t) \right\rangle \\ &= \frac{B}{4\pi\rho(S_n, I_t \pm 1/2, \pi_t)} \int_0^{S_n} \mathrm{d}E_\gamma\, \mathcal{T}(E_\gamma)\rho(S_n - E_\gamma) \\ &\quad \times \sum_{J=-1}^{1} g(S_n - E_\gamma, I_t \pm 1/2 + J)\,. \end{aligned} \tag{8}$$

Here, I_t and π_t are the spin and parity of the target nucleus in the neutron capture (n, γ) reaction. We determine B by using the BSFG model for the spin distribution g given in Ref. [12] and the experimental value of $\left\langle \Gamma_\gamma(S_n) \right\rangle$.

For ^{121}Sn, the radiative width at the neutron separation energy is available in literature. For ^{122}Sn, we estimated it from systematics. Figure 6 shows the $\left\langle \Gamma_\gamma(S_n) \right\rangle$ plotted against S_n for Sn isotopes where this quantity is known (taken from Ref. [13]). From the appearing trend of the even-even nuclei, we estimate $\left\langle \Gamma_\gamma(S_n) \right\rangle$ to 85(42) meV for ^{122}Sn. The applied input parameters needed for determining the normalization constant B for ^{121,122}Sn are shown in Tab. II. The values for ^{121}Sn have been taken from Ref. [13].

TABLE II: Input parameters for normalization of the γ-ray transmission coefficient $\mathcal{T}$ of ^{121,122}Sn.

Nucleus	I_t ($\hbar$)	D_0 (eV)	$\left\langle \Gamma_\gamma(S_n) \right\rangle$ (meV)
^{121}Sn	0	1250(200)	40(5)
^{122}Sn	3/2	62(31)[a]	85(42)[a]

[a] Estimated from systematics.

The normalized γ-ray strength functions of ^{121,122}Sn are shown in Fig. 7. The error bars show the statistical uncertainties. While the strength function of ^{121}Sn is smooth, just like those of $^{116-119}$Sn [2, 3], the strength function of ^{122}Sn displays clear structures in the entire E_γ region. As discussed in Sec. III, these structures also appear using different, independent data sets.

A change of the log-scale slope in the strength functions, leading to a sudden increase of strength, is seen in ^{121,122}Sn for $E_\gamma > 5.2$ MeV. The change of log-scale slope represents the onset of a small resonance, commonly related to as the pygmy dipole resonance. A comparison of our ^{121,122}Sn measurements compared with photonuclear cross section data from Refs. [18–22] is shown in the two upper panels in Fig. 8. Similar strength increases were also seen in $^{116-119}$Sn [3], and this figure will be further discussed for those isotopes when discussing the evolution of the pygmy resonance in the next section.

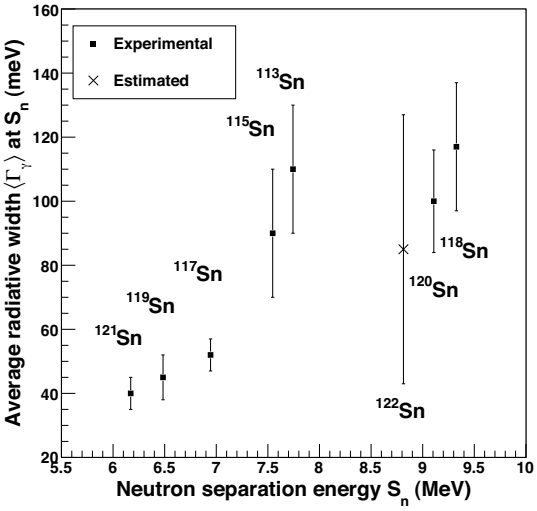

FIG. 6: Estimation of the average radiative width at S_n, $\left\langle \Gamma_\gamma(S_n) \right\rangle$, for ^{122}Sn. The respective values of other Sn isotopes are plotted (squares) as a function of S_n. (See text.)

In order to investigate the experimental strength functions of ^{121,122}Sn, we have applied commonly used models for the GEDR resonance and for the magnetic spin-flip resonance, also known as the Giant Magnetic Dipole Resonance (GMDR).

The Generalized Lorentzian (GLO) model [23] is used for the GEDR resonance. The GLO model is known to agree rather well both for low γ-ray energies and for the GEDR centroid at about 15 MeV. The strength function approaching a non-zero value for low E_γ is not a property specific for the Sn isotopes, but has been seen for all nuclei studied at the OCL so far.

In the GLO model, the $E1$ strength function is given by

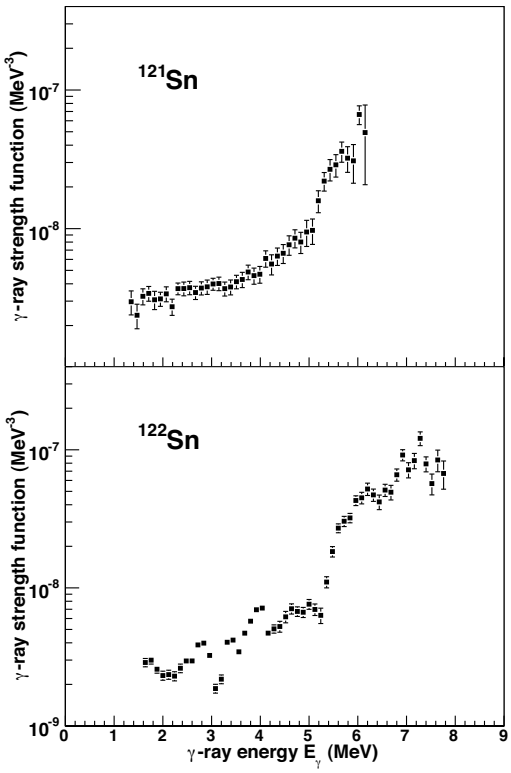

FIG. 7: Normalized γ-ray strength functions of ^{121,122}Sn as functions of γ-ray energy. The energy bins are 120 keV/ch.

[23]:

$$f_{E1}^{\mathrm{GLO}}(E_\gamma) = \frac{1}{3\pi^2\hbar^2c^2}\sigma_{E1}\,\Gamma_{E1} \times \left[E_\gamma \frac{\Gamma_{KMF}(E_\gamma, T_f)}{\left({E_\gamma}^2 - {E_{E1}}^2\right)^2 + {E_\gamma}^2\left(\Gamma_{KMF}(E_\gamma, T_f)\right)^2} + 0.7\,\frac{\Gamma_{KMF}(E_\gamma = 0, T_f)}{{E_{E1}}^3}\right], \quad (9)$$

in units of MeV^{-3}, where the Lorentzian parameters are the GEDR's centroid energy E_{E1}, width Γ_{E1} and cross section σ_{E1}. These experimental parameters are not available for ^{121,122}Sn. We instead apply the one measured for ^{120}Sn to ^{121}Sn, and the one measured for ^{124}Sn to ^{122}Sn, from Fultz [18] (see Tab. III).

The GLO model is temperature dependent from the incorporation of a temperature dependent width Γ_{KMF}. This width is the term responsible for the non-vanishing $E1$ strength at low excitation energy. It has been adopted from the Kadmenskiĭ, Markushev and Furman (KMF) model [24] and is given by:

$$\Gamma_{KMF}(E_\gamma, T_f) = \frac{\Gamma_r}{{E_r}^2}\left({E_\gamma}^2 + 4\pi^2{T_f}^2\right), \quad (10)$$

in units of MeV, and where T_f is the temperature.

Usually, T_f is interpreted as the nuclear temperature of the final state, with the commonly applied expression $T_f = \sqrt{U/a}$. In this work and in Refs. [1–3], we assume a constant temperature, i.e., the γ-ray strength function is independent of excitation energy. This approach is adopted for consistency with the Brink-Axel hypothesis (see Sec. III).

Moreover, we treat T_f as a free parameter. This is necessary to adjust the theoretical strength prediction to our low-energy measurements. The applied values of the T_f parameters are listed in Tab. III.

TABLE III: Applied parameters for the parameterization of the GEDR and the GMDR contributions for ^{121,122}Sn.

Nucleus	E_{E1} (MeV)	Γ_{E1} (MeV)	σ_{E1} (mb)	E_{M1} (MeV)	Γ_{M1} (MeV)	σ_{M1} (mb)	T_f (MeV)
^{121}Sn	15.53	4.81	253.0	8.29	4.00	1.11	0.25(5)
^{122}Sn	15.59	4.77	256.0	8.27	4.00	1.09	0.25(5)

The $M1$ spin-flip resonance is modeled with the functional form of a Standard Lorentzian (SLO) model [25]:

$$f_{M1}^{\mathrm{SLO}}(E_\gamma) = \frac{1}{3\pi^2\hbar^2c^2}\frac{\sigma_{M1}{\Gamma_{M1}}^2 E_\gamma}{\left({E_\gamma}^2 - {E_{M1}}^2\right)^2 + {E_\gamma}^2{\Gamma_{M1}}^2}, \quad (11)$$

where the parameter E_{M1} is the centroid energy, Γ_{M1} the width and σ_{M1} the cross section of the GMDR. These Lorentzian parameters are for ^{121,122}Sn predicted from the theoretical expressions in Ref. [25] and shown in Tab. III. The predictions for the GEDR using the GLO model and for the GMDR for $^{116-119,121,122}$Sn nuclei are shown as dashed lines in Fig. 8.

The Standard Lorentzian (SLO) model was also tested and is included in Fig. 8 (the $M1$ spin-flip resonance contribution is added to it). The SLO succeeds in reproducing the (γ, x) data, but clearly fails for the low-energy strength measurements, both when it comes to absolute value and shape. The same has been the case also for many other nuclei measured at the OCL and elsewhere. Therefore, we consider the SLO not to be adequate below the neutron threshold.

At present, it is unclear how these resonances should be modeled properly, although many theoretical predictions exist. We have found [2, 3] that the Sn pygmy resonance is satisfactorily reproduced by a Gaussian distribution [2]:

$$f_{\mathrm{pyg}}(E_\gamma) = C_{\mathrm{pyg}} \cdot \frac{1}{\sqrt{2\pi}\,\sigma_{\mathrm{pyg}}}\exp\left[\frac{-\left(E_\gamma - E_{\mathrm{pyg}}\right)^2}{2{\sigma_{\mathrm{pyg}}}^2}\right], \quad (12)$$

superimposed on the GLO prediction. Here, C_{pyg} is the resonance's absolute value normalization constant, E_{pyg} the centroid energy and σ_{pyg} the width. These parameters are treated as free.

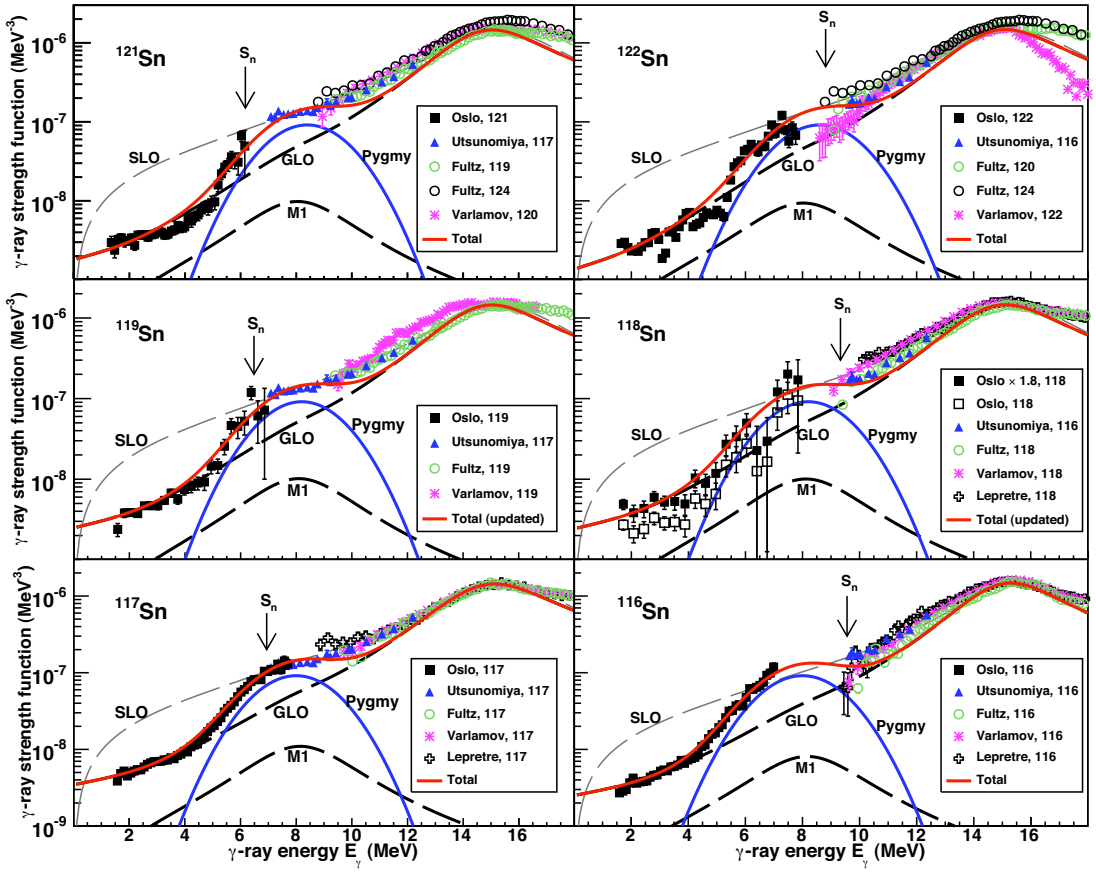

FIG. 8: (Color online) Comparison of the prediction of the total strength functions with the OCL experimental measurements for $^{116-119,121,122}$Sn. The strength function of ^{118}Sn is shown both as multiplied with 1.8 (filled squares) and as the original normalization (open squares). The arrows indicate S_n. The total strength predictions (solid lines) are modeled as Gaussian pygmy resonance additions to the GLO (E1 + M1) baselines. The SLO (E1 + M1) baselines are also shown.
Upper, left panel: ^{117}Sn(γ, n) from Utsunomiya *et al.* [19], ^{119,124}Sn(γ, x) from Fultz *et al.* [18], and ^{120}Sn(γ, x) from Varlamov *et al.* [21].
Upper, right panel: ^{116}Sn(γ, n) [19], ^{120,124}Sn(γ, x) [18], and ^{122}Sn(γ, n) from Varlamov *et al.* [20].
Middle, left panel: ^{117}Sn(γ, n) [19], ^{119}Sn(γ, x) [18], and ^{119}Sn(γ, n) [20].
Middle, right panel: ^{116}Sn(γ, n) [19], ^{118}Sn(γ, x) [18], ^{118}Sn(γ, x) from Varlamov *et al.* [21], and ^{118}Sn(γ, x) from Leprêtre *et al.* [22].
Lower, left panel: ^{117}Sn(γ, n) [19], ^{117}Sn(γ, x) [18], ^{117}Sn(γ, x) [21], and ^{117}Sn(γ, x) [22].
Lower, right panel: ^{116}Sn(γ, n) [19], ^{116}Sn(γ, x) [18], ^{116}Sn(γ, x) [21], and ^{116}Sn(γ, x) [22].

By adding the discussed theoretical strength contributions, the prediction of the total γ-ray strength function is given by:

$$f_{\text{total}} = f_{E1} + f_{M1} + f_{\text{pyg}} \,. \tag{13}$$

We determined the Gaussian pygmy parameters of ^{121,122}Sn from fitting to our measurements. The centroid energies of the pygmy resonances are 8.4(1) and 8.6(2) MeV, respectively. We found that the same width σ_{pyg} and strength C_{pyg} as in ^{116,117}Sn [3] gave a very good agreement also in ^{121,122}Sn, so the width and strength are kept unchanged. The pygmy parameters are listed in Tab. IV. The estimated error bars given in the table take into account systematic uncertainties in the normalization values and in the choice of baseline of the pygmy resonance, including the fact that the GLO does not perfectly follow the (γ, n) measurements for higher E_γ values.

The predictions for ^{121,122}Sn are shown as solid lines in the upper panels of Fig. 8. We see that the predictions of the total strength describe the measurements rather well, in the sense that the Gaussian pygmy resonances fill a very large fraction of the missing strength. Still, the Gaussian distribution does

TABLE IV: Empirical values of Gaussian pygmy parameters, and the corresponding integrated strengths and TRK values of the pygmy resonances, in ^{121,122}Sn.

Nucleus	E_{pyg} (MeV)	σ_{pyg} (MeV)	C_{pyg} (10^{-7}MeV^{-2})	Integrated strength (MeV·mb)	TRK value (%)
^{121}Sn	8.4(1)	1.4(1)	3.2^{+3}_{-9}	31^{+3}_{-8}	1.8^{+1}_{-5}
^{122}Sn	8.6(2)	1.4(1)	3.2^{+3}_{-9}	32^{+2}_{-9}	1.8^{+1}_{-5}

not completely follow neither the left flank nor the right flank of the pygmy resonances in ^{121,122}Sn. In the case of ^{116,117}Sn [2, 3], having a larger T_f of T_f = 0.46(1) MeV, the left flank was followed very well. However, in all Sn isotopes, there is a gap on the right flank between measured data and the GLO. A better pygmy resonance representation than the Gaussian or a better model for the baseline may be found in the future.

Strength from the resonances in ^{121,122}Sn have been added in the energy region of $\approx 5-8$ MeV according to our measurements, and in the region of $\approx 5-11$ MeV when comparing to photonuclear data as well. The total integrated strengths of the pygmy resonances, based on the total predictions, are estimated to 32^{+3}_{-9} MeV·mb. This constitutes 1.8^{+1}_{-5}% of the classical Thomas-Reiche-Kuhn (TRK) sum rule, assuming all pygmy resonance strength being $E1$, see Tab. IV.

Even though uncertainties in the choice of baseline have been considered in the uncertainty estimates, another prediction of the GEDR than the GLO or another function for the pygmy resonance than the Gaussian may be found in the future. This will consequently influence the estimates on the pygmy resonance. Lack of data, i.e., the gaps between our measurements and the (γ, n) measurements in resonance region, and also the lack of (γ, n) measurements for ^{121,122}Sn, adds to the uncertainties in the estimates of the pygmy resonances.

Measurements from other reactions and using other methods have also been used to estimate the TRK value of the Sn pygmy, and these estimates deviate from each other. Data from ^{116,117}Sn(γ,n) experiments [19] indicate an integrated strength which constitutes $\approx$ 1% of the TRK sum rule, which agrees within the uncertainty with our value. From ^{116,124}Sn(γ,γ') experiments [26], the TRK value is calculated to 0.4 – 0.6%. This may seem to deviate from our result. However, taking into account unresolved strength in the quasi-continuum of typically a factor of 2 – 3, the (γ,γ') results are compatible within the uncertainty with the other data.

VI. EVOLUTION OF THE PYGMY RESONANCE

Studying the neutron dependency is important and may help in determining the origin of the Sn pygmy resonance. Figure 9 shows the present and previously analyzed normalized strength functions for the Sn isotopes. The measurements of ^{118}Sn have been multiplied by 1.8 in order to agree with those of ^{116}Sn (see Ref. [3]).

First, it may seem like a trend that the tail of the strength function decreases in strength as the neutron number N increases. Second, it is noticeable from Fig. 9 that the change of log-scale slope, which represents the onset of the pygmy resonance, occurs at an higher E_γ value in ^{121,122}Sn than for ^{116,117}Sn. The changes of slope are clearest for the even-even nuclei. They are found at $\approx$ 4.5 MeV in ^{116}Sn and at $\approx$ 5.2 MeV in ^{122}Sn.

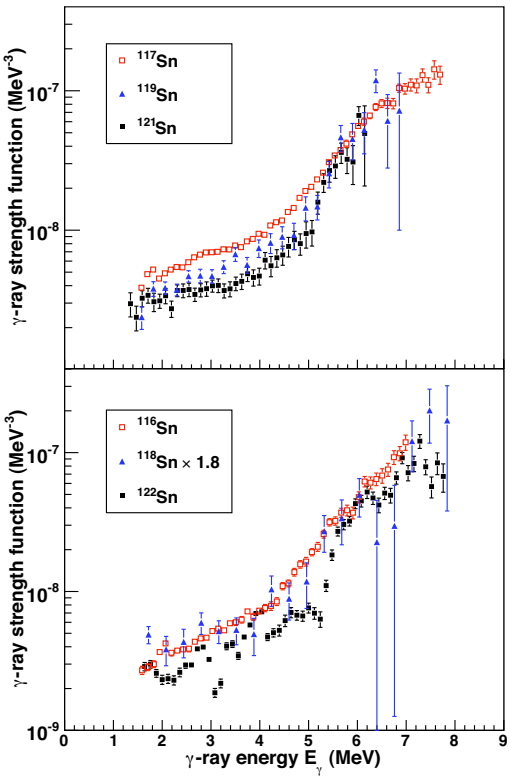

FIG. 9: (Color online) Normalized γ-ray strength functions as functions of γ-ray energy for the Sn isotopes measured at the OCL. The even-odd isotopes, ^{117,119,121}Sn, are shown in the upper panel, while the even-even isotopes, ^{116,118,122}Sn, are shown in the lower. The measured strength of ^{118}Sn has been multiplied by 1.8 (see Ref. [3]). The energy bins are 120 keV/ch for ^{116,117,121,122}Sn, 240 keV/ch for ^{119}Sn and 360 keV/ch for ^{118}Sn.

The values of T_f for ^{121,122}Sn are lower than for $^{116-119}$Sn. There is no physical reason for different nuclear temperatures. Lowering the parameter T_f is instead necessary in order to get the lowest-energy part of the GLO comparable in magnitude with the measurements.

The centroid energy E_{pyg} of the pygmy resonances in ^{121,122}Sn has larger values than those of earlier studies in ^{116,117}Sn [2, 3]. For ^{121,122}Sn, the pygmy centroids ire 8.4(1) and 8.6(2) MeV (see Tab. IV), respectively, while 8.0(1) MeV is found for ^{116,117}Sn [2, 3]. During the pygmy resonance fit-

TABLE V: Empirical values of $^{116-119}$Sn Gaussian pygmy parameters, and the corresponding pygmies' integrated strengths and TRK values. For ^{118}Sn, the values have been found from fitting to the measured strength function multiplied by 1.8.

Nucleus	$E_{\rm pyg}$ (MeV)	$\sigma_{\rm pyg}$ (MeV)	$C_{\rm pyg}$ (10^{-7}MeV^{-2})	Integrated strength (MeV·mb)	TRK value (%)
^{116}Sn	8.0(1)	1.4(1)	3.2^{+3}_{-9}	30^{+0}_{-8}	1.7^{+0}_{-4}
^{117}Sn	8.0(1)	1.4(1)	3.2^{+3}_{-9}	30^{+0}_{-8}	1.7^{+0}_{-4}
^{118}Sn	8.2(1)	1.4(1)	3.2^{+0}_{-9}	30^{+0}_{-8}	1.8^{+0}_{-5}
^{119}Sn	8.2(1)	1.4(1)	3.2^{+0}_{-9}	30^{+0}_{-8}	1.7^{+0}_{-4}

TABLE VI: Applied parameters for the parameterization of the GEDR and the GMDR contributions for $^{116-119}$Sn.

Nucleus	E_{E1} (MeV)	Γ_{E1} (MeV)	σ_{E1} (mb)	E_{M1} (MeV)	Γ_{M1} (MeV)	σ_{M1} (mb)	T_f (MeV)
^{116}Sn	15.68	4.19	266.0	8.41	4.00	0.773	0.46(1)
^{117}Sn	15.66	5.02	254.0	8.38	4.00	1.04	0.46(1)
^{118}Sn	15.59	4.77	256.0	8.36	4.00	0.956	0.40(1)
^{119}Sn	15.53	4.81	253.0	8.34	4.00	0.963	0.40(1)

ting, it was clear that the centroid energies had to be significantly increased for the heavier isotopes. The significant increases are also apparent from studying the energies for which there is a change of log-scale slope in the strength functions. Moreover, keeping the centroid energy constant has as a consequence that the same pygmy width $\sigma_{\rm pyg}$ and pygmy strength $C_{\rm pyg}$ as in ^{116,117}Sn [3] also give the best fit in ^{121,122}Sn.

In the earlier study of ^{118,119}Sn [3], the data have large error bars. This means that the pattern of an increasing centroid energy was not so clear, and the choice then was to keep the centroid energy constant while compensating with an increase of the resonance width. We have updated the resonance prediction of ^{118,119}Sn by following the same pattern. The estimated centroid energy of the pygmies in ^{118,119}Sn is then 8.2(1) MeV, while the width and strength are kept constant. Updated parameter values are listed in Tab. V and displayed in Fig. 8. The parameters for the GEDR and GMDR contributions are listed in Tab. VI.

We would like to investigate for several isotopes the effect of our predicted pygmy resonances on the (n,γ) cross sections and compare these with available experimental measurements. This has been done for $^{117-119,121}$Sn using the reaction code TALYS [27]. For the level density, we have applied the spin- and parity-dependent calculations of Goriely, Hilaire and Koning [28], which are in good agreement with our level-density data, as demonstrated for ^{117}Sn in Fig. 10. Also, we have used the neutron optical potential of Koning and Delaroche [29].

The results of the comparisons are shown in Fig. 11. Our modeled strength function with a Gaussian pygmy resonance (denoted GLO2) leads to a calculated cross section that generally agrees very well with the measurements. Assuming the GLO model with constant temperature but without the pygmy resonance (GLO1), clearly gives a lower cross section in all cases, as expected. This may be taken as a support of the finding of an enhanced strength function in the E_γ region of

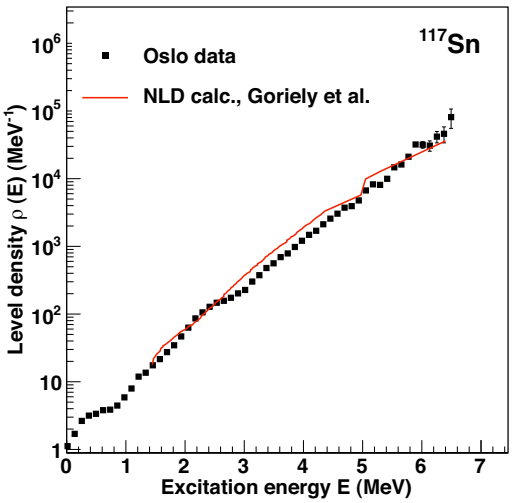

FIG. 10: (Color online) Level-density measurements on ^{117}Sn compared with microscopic calculations from Ref. [28].

$\approx 5-11$ MeV. The SLO model gives an overall too high cross section, which is not surprising considering the large overshoot in γ-ray strength compared to our measurements and also to $\langle\Gamma_\gamma\rangle$ data. We note that our calculated cross section for ^{116}Sn$(n,\gamma)^{117}$Sn using the GLO2 model is in very good agreement with the one in the work of Utsunomiya *et al.* [19].

For the ^{117}Sn$(n,\gamma)^{118}$Sn case, we have applied the model parameters that correspond to our scaled data (with a factor of 1.8). The resulting excellent agreement with the experimental (n,γ) data further supports our choice of renormalization in Ref. [3]. We have in addition tested the strength prediction using parameters that fit with the original normalization, which results in calculated cross section that are clearly underpredictive compared to the experimental data (not shown here).

The reproduction of the ^{120}Sn$(n,\gamma)^{121}$Sn cross section is not as good as for the other nuclei, as this calculation seems to be somewhat more underpredictive. However, the calculation is certainly an improvement compared to that of the GLO1, which is a standard strength model without the pygmy resonance. The underprediction might be explained by too low experimental value of $\langle\Gamma_\gamma\rangle$ in the normalization procedure of the measurements. If the value had been higher, the pygmy resonance would had produced more strength, leading to a general increase of the calculated cross section.

We would also like to study the evolution of the resonances' centroid energy $E_{\rm pyg}$ with neutron number N. Figure 12 shows $E_{\rm pyg}$ as a function of N for the isotopes studied at the OCL. A χ^2 fit has been performed on these data, resulting in the linear

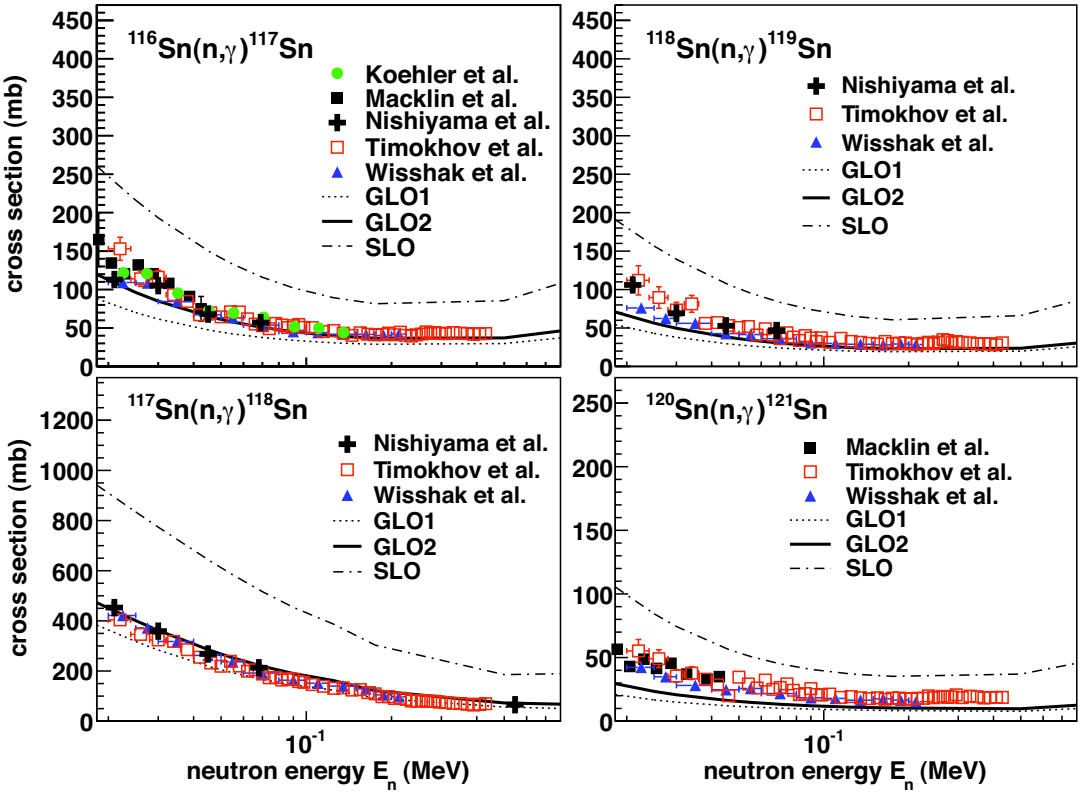

FIG. 11: (Color online) Data on neutron-capture cross sections for the target nuclei $^{116-118,120}$Sn compared with calculations, for neutron energies $\gtrsim$ 20 keV. GLO1 (dotted line) is the GLO model assuming constant temperatures (given in Tabs. IV and VI), and GLO2 (solid line) is the GLO1 model plus the prediction of the pygmy resonance. Measurements from Koehler *et al.* [30], Macklin *et al.* [31], Nishiyama *et al.* [32], Wisshak *et al.* [33], and Timokhov *et al.* [34].

relation $E_{\mathrm{pyg}} = 2.0(16) + 0.090(23) \cdot N$ in units of MeV.

The estimates on E_{pyg} from others' experimental data on Sn are in agreement within the uncertainties with the observed pattern: $\approx$ 8.5 MeV for ^{116,117}Sn [19], $\approx$ 7.8 MeV for ^{117,119}Sn [35], and 10.1(7) and 9.8(7) MeV for ^{130,132}Sn [36], respectively. It is commented that an increase of the resonances' centroid energies with increasing neutron number was also found in experimental data on Ca [37].

The observation of an increase of the centroid energy with increasing neutron number is not in agreement with common theoretical predictions. On the contrary, studies on Sn isotopes instead predict a decrease of centroid energy with increasing neutron number. These studies include the Hartree-Fock-Bogoljubov (HFB) and multiphonon quasiparticle-phonon (QPM) models by Tsoneva and Lenske [38], the RHB+RQRPA (DD-ME2) model by Paar [39], and the Continuum QRPA model by Daoutidis [40]. Also a theoretical study on Ca isotopes, using the Extended Theory of Finite Fermi Systems (ETFFS) by Tertychny [37], results in a decrease of centroid energy with neutron number (in contrary to experimental results on Ca, see Ref. [37] and references therein). However, it is commented that Daoutidis [40] predicts a relatively stable centroid energy in the atomic mass region $A = 120 - 126$ compared to other mass regions. Hence, the increase of centroid energy in the isotopes that we have compared, may be less than would had been observed in another mass region.

Recent measurements using the $(\alpha, \alpha'\gamma)$ coincidence method on ^{124}Sn compared to photon-scattering experiments show a splitting into its isoscalar and isovector components [41]. Hence, both components seem to be present, in agreement with theoretical predictions.

The nature, origin, and integrated strength of the Sn pygmy resonance are issues that are heavily debated. The $E1$ neutron-

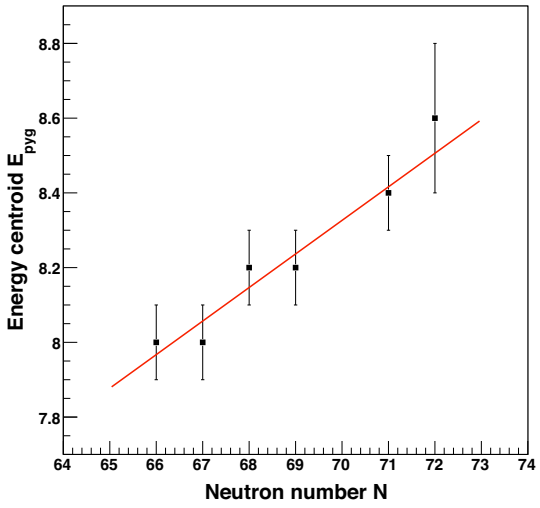

FIG. 12: (Color online) Estimated centroid energies $E_{\rm pyg}$ (squares) as a function of neutron number N, deduced from our measurements on $^{116-119,121,122}$Sn. The solid line is a linear χ^2 fit to the measurements.

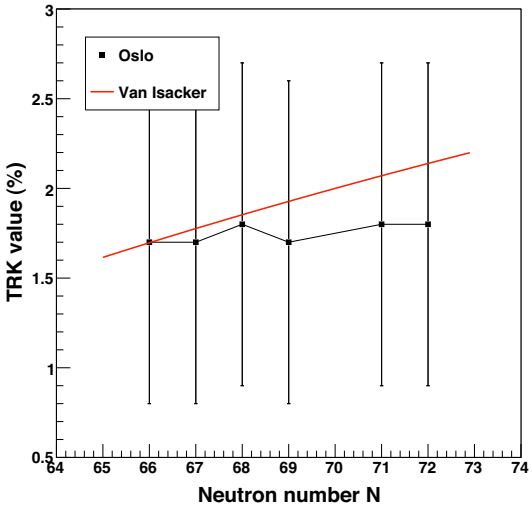

FIG. 13: (Color online) TRK values for Sn estimated from our measurements (squares) compared to the theoretical prediction from Van Isacker *et al.* [42] (multiplied by a factor 14) (solid line) as a function of neutron number N.

skin oscillation mode, discussed in Refs. [39, 42, 43], is assumed as the underlying physical phenomenon in most of the theoretical predictions, both in macroscopic (e.g., Van Isacker *et al.* [42]) and microscopic approaches (e.g., Daoutidis [40], Tsoneva and Lenske [38], Paar [39], Sarchi *et al.* [43]). Most theoretical calculations predict a systematic increase of the resonances' strength as the number of neutrons increase, due to the increase of the number of neutrons in the skin. Another prediction is the increase by neutron number up to ^{120}Sn followed by a decrease (Paar [39]). Several of the predicted increases of integrated strength concerning the isotopes that we have performed measurements on, are significant (e.g., Tsoneva and Lenske [38], Van Isacker *et al.* [42], Litvinova *et al.* [44]). It is commented that the study by Daoutidis [40] predicts that also the integrated strength is relatively stable in the mass region $A = 120 - 126$.

However for our measurements on the pygmy resonances in $^{116-119,121,122}$Sn, we cannot see any dependency on neutron number in the integrated strengths. The same resonance prediction has on the contrary been applied for all isotopes. (The total integrated strengths and the TRK values of ^{121,122}Sn being slightly larger than those of ^{116,117}Sn, see Tabs. IV and IV, is explained by differences in the GLO models of those isotopes.) Figure 13 shows our TRK values together with those of Van Isacker *et al.* [42] (multiplied by a factor of 14 in absolute value). The experimental result does not follow the predicted increase. Still, the uncertainties in our estimated resonance strengths are large. More experimental information is therefore needed in order to answer the question if the integrated strength in Sn increases with neutron number.

The experimental TRK values based on our and others' measurements are relatively large, compared to general excitations. This might indicate that the pygmy resonance is due to a collective phenomenon. However, its origin is unknown, and single-particle excitations are not excluded. Various theoretical predictions disagree on whether the neutron skin-oscillation is collective or not [39].

A clarification of the electromagnetic character of the pygmy resonance in Sn would be of utmost importance. Present theoretical predictions assumes an $E1$ strength, modeling the resonance as a neutron-skin oscillation. Experimental studies have indicated an $E1$ character. Amongst these are the nuclear resonance fluorescence (NRF) experiments performed on ^{116,124}Sn [26] and on ^{112,124}Sn [45], and the Coulomb dissociation experiments performed on $^{129-132}$Sn [36, 46]. In addition comes the polarized photon beams experiments on ^{138}Ba [47]. However, the existence of an $M1$ component of the resonance strength cannot be ruled out, as was discussed in Ref. [3].

VII. CONCLUSIONS

The level density and γ-ray strength functions of ^{121,122}Sn have been measured using the (^{3}He,^{3}He$'\gamma$) and (^{3}He,$\alpha\gamma$) reactions and the Oslo method. The level densities of ^{121,122}Sn display step-like structures for excitation energies below $\approx$ 4 MeV. One of the bumps is interpreted as a signature of neutron pair breaking, in accordance with the findings in $^{116-119}$Sn.

A significant enhancement in the γ-ray strength is observed in the ^{121,122}Sn measurements for $E_\gamma \gtrsim 5.2$ MeV. The integrated strength of the resonances correspond to $\approx 1.8^{+1}_{-5}$% of the TRK sum rule. These enhancements are compatible with pygmy resonances centered at $\approx$ 8.4(1) and $\approx$ 8.6(2) MeV, respectively.

Neutron-capture cross-section calculations using our pygmy resonance predictions give significantly better reproduction of experimental (n,γ) cross sections than standard strength models without any pygmy resonance.

The pygmy resonances are compared to those observed in $^{116-119}$Sn. The evolution with increasing neutron number of the pygmy resonances observed in $^{116-119,121,122}$Sn is a clear increase of centroid energy from 8.0(1) MeV in ^{116}Sn to 8.6(2) MeV in ^{122}Sn, while no difference in integrated strength is observed. This finding is not in agreement with most theoretical predictions. However, the experimental uncertainties are large, and more experimental information is needed in order to determine the nature of the pygmy resonances in the Sn isotopes.

Acknowledgments

The authors would like to thank H. Utsunomiya for giving us access to yet unpublished experimental results from photoneutron cross-section reactions ^{120,122}Sn(γ,n). The Department of Physics at the University of Jyväskylä (JYFL) is thanked for kindly lending us the ^{122}Sn target. Last but not least, thanks to E. A. Olsen, J. Wikne, and A. Semchenkov for excellent experimental conditions. The funding of this research from The Research Council of Norway (Norges forskningsråd) is gratefully acknowledged.

[1] U. Agvaanluvsan, A. C. Larsen, M. Guttormsen, R. Chankova, G. E. Mitchell, A. Schiller, S. Siem, and A. Voinov, Phys. Rev. C **79**, 014320 (2009).

[2] U. Agvaanluvsan, A. C. Larsen, R. Chankova, M. Guttormsen, G. E. Mitchell, A. Schiller, S. Siem, and A. Voinov, Phys. Rev. Lett. **102**, 162504 (2009).

[3] H. K. Toft, A. C. Larsen, U. Agvaanluvsan, A. Bürger, M. Guttormsen, G. E. Mitchell, H. T. Nyhus, A. Schiller, S. Siem, N. U. H. Syed, A. Voinov, Phys. Rev. C **81**, 064311 (2010).

[4] M. Guttormsen, A. Atac, G. Løvhøiden, S. Messelt, T. Ramsøy, J. Rekstad, T. F. Thorsteinsen, T. S. Tveter, and Z. Zelazny, Phys. Scr. **T 32**, 54 (1990).

[5] M. Guttormsen, T. S. Tveter, L. Bergholt, F. Ingebretsen, and J. Rekstad, Nucl. Instrum. Methods Phys. Res. A **374**, 371 (1996).

[6] M. Guttormsen, T. Ramsøy, and J. Rekstad, Nucl. Instrum. Methods Phys. Res. A **255**, 518 (1987).

[7] A. C. Larsen, M. Guttormsen, E. Bětàk, A. Bürger, A. Görgen, M. Krtička, H. T. Nyhus, J. Rekstad, A. Schiller, S. Siem, H. K. Toft, G. M. Tveten, A. Voinov, and K. Wikan, *A review of the Oslo method*, submitted to Phys. Rev. C. (2010).

[8] A. Schiller, L. Bergholt, M. Guttormsen, E. Melby, J. Rekstad, and S. Siem, Nucl. Instrum. Methods Phys. Res. A **447**, 498 (2000).

[9] A. Bohr and B. Mottelson, Nuclear Structure (Benjamin, New York, 1969), Vol. I.

[10] D. M. Brink, Ph.D. thesis, Oxford University, 1955.

[11] P. Axel, Phys. Rev. **126**, 671 (1962).

[12] T. von Egidy, H. H. Schmidt, and A. N. Behkami, Nucl. Phys. **A481**, 189 (1988).

[13] R. Capote *et al.*, *RIPL-3 – Reference Input Parameter Library for Calculation of Nuclear Reactions and Nuclear Data Evaluations*, Nucl. Data Sheets **110**, 3107 (2009). Available online at [http://www-nds.iaea.org/RIPL-3/].

[14] G. Audi and A. H. Wapstra, Nucl. Phys. **A595**, 409 (1995).

[15] J. Dobaczewski, P. Magierski, W. Nazarewicz, W. Satuła, and Z. Szymański, Phys. Rev. C **63**, 024308 (2001).

[16] A. Gilbert and A. G. W. Cameron, Can. J. Phys. **43**, 1446 (1965).

[17] A. Voinov, M. Guttormsen, E. Melby, J. Rekstad, A. Schiller, and S. Siem, Phys. Rev. C **63**, 044313 (2001).

[18] S. C. Fultz, B. L. Berman, J. T. Caldwell, R. L. Bramblett, and M. A. Kelly, Phys. Rev. **186**, 1255 (1969).

[19] H. Utsunomiya, S. Goriely, M. Kamata, T. Kondo, O. Itoh, H. Akimune, T. Yamagata, H. Toyokawa, Y.-W. Lui, S. Hilaire, and A. J. Koning, Phys. Rev. C **80**, 055806 (2009).

[20] V. V. Varlamov, B. S. Ishkhanov, V. N. Orlin, V. A. Tchetvertkova, Moscow State Univ. Inst. of Nucl. Phys. Reports No. 2009, p. 3/847 (2009).

[21] V. V. Varlamov, N. N. Peskov, D. S. Rudenko, and M. E. Stepanov, Vop. At. Nauki i Tekhn., Ser. Yadernye Konstanty 1-2 (2003).

[22] A. Leprêtre, H. Beil, R. Bergere, P. Carlos, A. De Miniac, A. Veyssiere, and K. Kernbach, Nucl. Phys. **A 219**, 39 (1974).

[23] J. Kopecky and R. E. Chrien, Nucl. Phys. **A 468**, 285 (1987).

[24] S. G. Kadmenskii, V. P. Markushev, and V. I. Furman, Yad. Fiz. **37**, 277 (1983) [Sov. J. Nucl Phys. **37**, 165 (1983)].

[25] T. Belgya *et al.*, *Handbook for calculations of nuclear reaction data*, RIPL-2, (IAEA, Vienna, 2006). Available online at [http://www-nds.iaea.org/RIPL-2/].

[26] K. Govaert, F. Bauwens, J. Bryssinck, D. De Frenne, E. Jacobs, W. Mondelaers, L. Govor, and V. Y. Ponomarev, Phys. Rev. C bf 57, 2229 (1998).

[27] A. J. Koning, S. Hilaire, and M. C. Duijvestijn, *"TALYS-1.2"*, in *Proceedings of the International Conference on Nuclear Data for Science and Technology*, April 22-27, 2007, Nice, France. Editors: O. Bersillon, F. Gunsing, E. Bauge, R. Jacqmin, and S. Leray, EDP Sciences, 211 (2008). Available online at [http://www.talys.eu/].

[28] S. Goriely, S. Hilaire, and A.J. Koning, Phys. Rev. C **78**, 064307 (2008).

[29] A. J. Koning and J. P. Delaroche, Nucl. Phys. **A 713**, 231 (2003).

[30] P. E. Koehler, R. R. Spencer, K. H. Guber, J. A. Harvey, N. W. Hill, and R. R. Winters, in *Proceedings of the International Conference on Nuclear Data for Science and Technology*, Trieste, Italy, 1997. Editors: G. Reffo, A. Ventura, and G. Grandi (Italian Physical Society, Bologna, Italy, 1997).

[31] R. L. Macklin, T. Inada, and J. H. Gibbons, Nature (London) **194**, 1272 (1962).

[32] J. Nishiyama, M. Igashira, T. Ohsaki, G. N. Kim, W. C. Chung, and T. I. Ro, J. Nucl. Sc. Tech. (Tokyo), **45**, 352 (2008).

[33] K. Wisshak, F. Voss, Ch. Theis, F. Käppeler, K. Guber, L. Kazakov, N. Kornilov, and G. Reffo, Phys. Rev. C **54**, 1451 (1996).
[34] V. M. Timokhov, M. V. Bokhovko, M. V. Isakov, L. E. Kazakov, V. N. Kononov, G. N. Manturov, E. D. Poletaev, and V. G. Pronyaev, Yad. Fiz. **50**, 609 (1989).
[35] E. J. Winhold, E. M. Bowey, D. B. Gayther, and B. H. Patrick, Physics Letters **32B**, 7 (1970).
[36] P. Adrich *et al.*, Phys. Rev. Lett. **95**, 132501 (2005).
[37] G. Tertychny, V. Tselyaev, S. Kamerdzhiev, F. Grümmer, S. Krewald, J. Speth, A. Avdeenkov, and E. Litvinova, Phys. Lett. B **647** 104 (2007).
[38] N. Tsoneva and H. Lenske, Phys. Rev. C **77**, 024321 (2008).
[39] N. Paar, Rep. Prog. Phys. **70** (2007), p. 691–793.
[40] I. Daoutidis (private communication).
[41] J. Endres, E. Litvinova, D. Savran, P. A. Butler, M. N. Harakeh, S. Harissopulos, R.-D. Herzberg, R. Krücken, A. Lagoyannis, N. Pietralla, V. Yu. Ponomarev, L. Popescu, P. Ring, M. Scheck, K. Sonnabend, V. I. Stoica, H. J. Wörtche, and A. Zilges, Phys. Rev. Lett. **105**, 212503 (2010).
[42] P. Van Isacker, M. A. Nagarajan, and D. D. Warner, Phys. Rev. C **45**, R13 (1992).
[43] D. Sarchi, P. F. Bortignon, and G. Colo, Phys. Lett. B **601**, 27 (2004).
[44] E. Litvinova, P. Ring, and V. Tselyaev, Phys. Rev. Lett. **105**, 022502 (2010).
[45] A. Tonchev (private communication).
[46] Klimkiewicz *et al.*, Phys. Rev. C **76**, 051603(R) (2007).
[47] A. Tonchev *et al.*, Phys. Rev. Lett. **104**, 072501 (2010).

7.3 Article 3: Analysis of possible systematic errors in the Oslo method

The Oslo method enables the simultaneous extraction of experimental level density and γ-ray transmission coefficient from a set of particle-γ-ray coincidence data. The assumptions behind each step in the method are tested in this article, and possible systematic errors and uncertainties are investigated in detail. This is done using typical experimental data sets from various mass regions, as well as with simulated data.

The finding is that although the Oslo method is very robust in general, the various assumptions the method relies on must be carefully considered when it is applied in different mass regions.

The excitation energy levels are fed in different intensity from the reaction and the decay from higher-lying states. When this different feeding occurs to the levels at low excitation energy, the shapes of the γ-ray spectra may be significantly different from those of the higher excitation energies. This is connected to the few states being present at low excitation energy. As a consequence, the subtraction of higher-order γ rays from the total spectra in the first-generation method may be erroneous for low γ-ray energies. Hence for low γ-ray energies, vertical ridges and/or valleys may occur in the first-generation matrix.

It is important for the first-generation method that the populated spin distribution is, at least approximately, independent of excitation energy. Else, the energy bins at high excitation energy would contain γ decays from states with higher spins than the bins at lower excitation energy, which would disturb the extraction of the first-generation γ rays. The spin populations as a function of excitation energy have been studied for experiments on nuclei in several mass regions, and the spin distributions have been found to be constant within the uncertainties. Hence, variations in the spin distribution are assumed not to be an important concern when applying the Oslo method.

In the region of high level density, the nucleus seems to attain a compound-like system before emitting the γ rays even though the undergone nuclear reaction is a direct reaction. The considered part of the first-generation matrix is therefore constrained to the region of higher excitation energy.

Testing on simulated data gives that if there is a temperature dependence in the γ-ray strength function (i.e., a contradiction of the Brink hypothesis), the strength especially at low γ-ray energy is affected. The extracted strength is found to be an average over the considered excitation-energy range. However, there is so far no experimental evidence for any strong temperature dependence of the strength function for the excitation-energy region in question (below $E \approx 10$ MeV).

Parity symmetry is assumed in the Oslo method. Parity asymmetry would

affect the normalisation value $\rho(S_n)$ and thus the normalisation of the slope, which is common to the level density and the strength function. A large parity asymmetry may change the value of $\rho(S_n)$ with a factor of ≈ 2. The parity asymmetry is expected to be largest for the lighter nuclei. However, experimental data on lighter nuclei suggest that the parity asymmetry is small even here. It is reasonable to believe that the error in $\rho(S_n)$ and in the absolute normalisation of the strength function does not exceed 50%.

Simulations with different spin ranges on the initial levels shows that the case with the range including the highest spins may give an enhanced strength function at low γ-ray energies for light nuclei. This is understood from considering the relatively low level density and the matching of spins between the initial and final levels for dipole radiation. This could explain, at least partially, the observed enhanced low-energy strength in experimental data for light and medium-mass nuclei.

The spin distribution is one of the largest uncertainties in the normalisation procedure, since the slope of the level density and strength function strongly depends on the relative intensities of the populated spins at S_n. The variation in the normalisation value $\rho(S_n)$ may be within a factor of two or more, especially for the rare-earth nuclei.

The experimentally reached spin window consists of low spins only, which means that the measured level density represents a narrow spin range. The Oslo method solves this by normalising at S_n the measured level density to $\rho(S_n)$, which is estimated for all spins. The impact is not big for light nuclei, since they have relatively few high-spin states. Even in the case of rare-earth nuclei, calculations indicate that this scaling works well, as the main structures in the level density are indeed also present in the level density of a rather narrow spin range.

Analysis of possible systematic errors in the Oslo method

A. C. Larsen,[1,*] M. Guttormsen,[1] M. Krtička,[2] E. Běták,[3,4] A. Bürger,[1] A. Görgen,[1] H. T. Nyhus,[1] J. Rekstad,[1] A. Schiller,[5] S. Siem,[1] H. K. Toft,[1] G. M. Tveten,[1] A. V. Voinov,[5] and K. Wikan[1]

[1]*Department of Physics, University of Oslo, N-0316 Oslo, Norway*
[2]*Institute of Particle and Nuclear Physics, Charles University, Prague, Czech Republic*
[3]*Institute of Physics SAS, 84511 Bratislava, Slovakia*
[4]*Faculty of Philosophy and Science, Silesian University, 74601 Opava, Czech Republic*
[5]*Department of Physics and Astronomy, Ohio University, Athens, Ohio 45701, USA*

(Dated: February 18, 2011)

In this work, we have reviewed the Oslo method, which enables the simultaneous extraction of level density and γ-ray transmission coefficient from a set of particle-γ coincidence data. Possible errors and uncertainties have been investigated. Typical data sets from various mass regions as well as simulated data have been tested against the assumptions behind the data analysis.

PACS numbers: 21.10.Ma,25.20.Lj,25.55.Hp,25.40.Ep

I. INTRODUCTION

Nuclear level densities and γ-ray strength functions are two indispensable quantities for many nuclear structure studies and applications. The approach developed by the nuclear physics group at the Oslo Cyclotron Laboratory (OCL), was first described in 1983 [1], and has during a period of nearly 30 years been refined and extended to the sophisticated level presently referred to as the Oslo method. The method is designed to extract the nuclear level density and the γ-ray transmission coefficient (or γ-ray strength function) up to the neutron (proton) threshold from particle-γ coincidence data. Typical reactions that have been utilized are transfer reactions such as (^{3}He, $\alpha\gamma$) and (p,$t\gamma$), and inelastic scattering reactions, e.g., (^{3}He, ^{3}He$'\gamma$) and (p,p$'\gamma$).

The measurements have been very successful and have shed new light on important issues in nuclear structure, such as the $M1$ scissors mode [2–5], and the sequential breaking of Cooper pairs [6, 7]. For the Sn isotopes, a resonance-like structure that may be due to the so-called $E1$ pygmy resonance has been observed [8, 9]. Also, a new, unpredicted low-energy increase in the γ-ray strength function for $E_\gamma \leq 3$ MeV of medium-mass nuclei has been discovered by use of this method [10–15]. This enhancement may have a non-negligible impact on stellar reaction rates relevant for the nucleosynthesis [16]. At present, this structure is poorly understood.

In this work, we have investigated the possible systematic errors that can occur in the Oslo method due to experimental limitations and the assumptions made in the various steps of the method. We have studied experimental data with high statistics (and thus low statistical errors) so that systematic errors can be revealed. Also, we have used simulated data to enable better control on the input parameters (level density and γ-ray strength function). In Sec. II we give a short overview of the experiments and the various steps in the method. In Sec. III we present the possible systematic errors for each main step of the method. Finally, a summary and concluding remarks are given in Sec. IV.

*Electronic address: a.c.larsen@fys.uio.no

II. EXPERIMENTAL PROCEDURE AND THE OSLO METHOD

The Oslo method is in fact a set of methods and analysis techniques, which together make it possible to measure level density and γ-ray strength from particle-γ coincidence data. In this section, these techniques and methods will be described.

A. Experimental details

The experiments were performed at the OCL using a light-ion beam delivered by the MC-35 Scanditronix cyclotron. Typically, ^{3}He beams with energy $30-45$ MeV have been used. Recently, also proton beams with energy $15-32$ MeV have been applied. Self-supporting targets enriched to $\approx 95\%$ in the isotope of interest, and with a thickness of ≈ 2 mg/cm^2 were placed in the center of the multi-detector array CACTUS [17]. CACTUS consists of 28 collimated NaI(Tl) γ-ray detectors with a total efficiency of 15.2(1)% for $E_\gamma = 1332$ keV. Usually also a 60% Ge detector has been applied to monitor the populated spin range ($\sim 0-8\hbar$) and possible target contaminations. The experiments were typically run for a period of $1-2$ weeks with beam currents of ~ 1 nA.

Inside the CACTUS array, eight collimated Si particle detectors were used for detecting the charged ejectiles from the nuclear reactions. The particle detectors were placed at 45° relative to the beam line in forward direction. The detectors were of $\Delta E-E$ type with a thin (~ 140 μm) front detector and a thick (~ 1500 μm) end detector where the charged ejectiles stop. The particle telescopes enable a good separation between the various charged-ejectile species. The energy resolution of the particle spectra ranges from $150-300$ keV depending on the beam species, the mass of the target nucleus and the size of the collimators. Both singles and coincidence

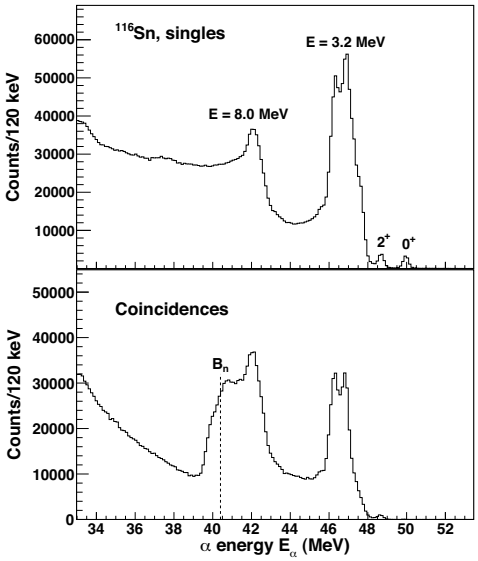

FIG. 1: Singles α-particle spectrum (upper panel), and α-γ coincidence spectrum (lower panel) from the ^{117}Sn(^{3}He, α)^{116}Sn reaction. The data are taken from the experiment presented in Ref. [7].

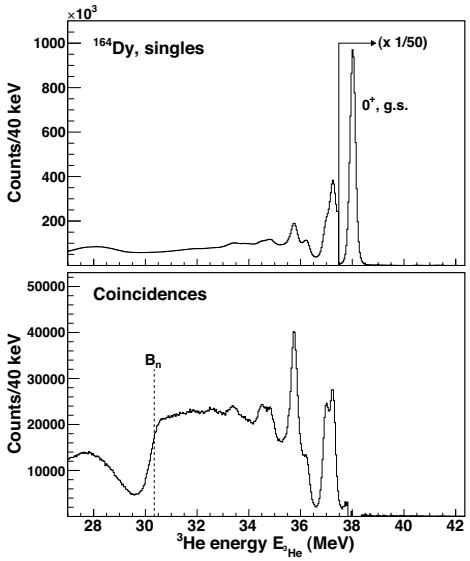

FIG. 2: Singles ^{3}He spectrum (upper panel), and ^{3}He-γ coincidence spectrum (lower panel) from the ^{164}Dy(^{3}He,^{3}He$'$)^{164}Dy reaction. The data are taken from the experiment presented in Ref. [5].

events were measured for the ejectiles. In Figs. 1, 2 and 3 the singles and particle-γ coincidence spectra are shown for the reactions ^{117}Sn(^{3}He,α)^{116}Sn, ^{164}Dy(^{3}He,^{3}He$'$)^{164}Dy and ^{46}Ti(p, p')^{46}Ti, respectively.

The ejectile energy can easily be transformed to the excitation energy of the residual nucleus using the reaction Q-values and kinematics. Thus, an excitation energy vs. γ-ray energy matrix can be built from the coincidence events. An example of such a matrix is shown in Fig. 4 (left panel), where the γ-ray spectra have been corrected for the known response functions of the CACTUS array [18]. The correction (or unfolding) method is described in detail in Ref. [18]. One of the main advantages with this method is that the fluctuations of the original spectra are preserved without introducing additional, spurious fluctuations.

B. Extracting primary γ rays

As γ decay from highly excited states often involves a cascade of transitions, it is necessary to isolate the γ rays that are emitted in the first decay step of all the possible decay routes, since information on the level density and the γ-ray strength function can be extracted from the distribution of these primary γ rays (also called first-generation γ rays). Therefore, a method has been developed in order to separate the primary γ-ray spectra from the γ rays that origin from the later steps in the decay cascades at each excitation energy. This method will hereafter be referred to as the *first-generation method* and is described in detail in Ref. [19]. This method is very important, since the correctness of the further analysis is completely dependent on correctly determined primary γ-ray spectra. The first-generation method shares several features with another subtraction technique developed by Bartholomew *et al.* [20]. The main features of the method will be outlined in the following.

From the E vs. E_γ matrix, where γ-ray spectra for each excitation energy are contained, the primary γ-ray spectra are extracted through an iterative subtraction technique. The unfolded spectra f_i are made of all generations of γ rays from all possible cascades decaying from the excited levels within the excitation-energy bin i. Now, we utilize the fact that the spectra $f_{j<i}$ for all the underlying energy bins j contain the same γ-transitions as f_i *except* the first γ rays emitted[1], since they will bring the nucleus from the states in energy bin i to underlying states in the bins j. Thus, the primary γ-ray spectrum h_i for each bin i can be found by

$$h_i = f_i - g_i, \tag{1}$$

[1] This is only true if the γ-decay pattern is the same regardless of whether the states in the bin were populated from the direct reaction, or from decay from above-lying bins. See Sec. III B.

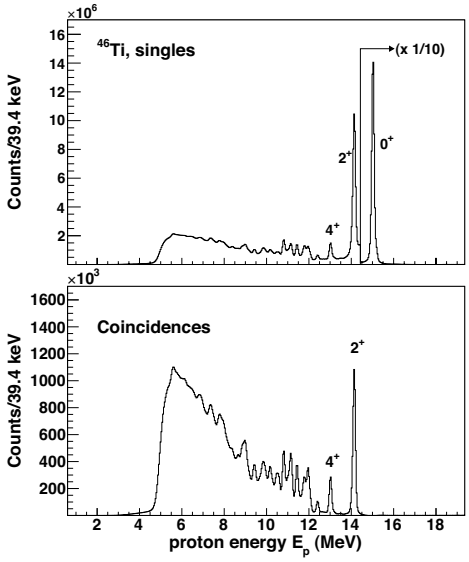

FIG. 3: Singles proton spectrum (upper panel) and p-γ coincidence spectrum (lower panel) from the ^{46}Ti(p, p')^{46}Ti reaction. The data are taken from the experiment presented in Ref. [15].

where g_i is a weighted sum of all spectra

$$g_i = n_{i1}w_{i1}f_1 + n_{i2}w_{i2}f_2 + \ldots + n_{ij}w_{ij}f_j = \sum_j n_{ij}w_{ij}f_j. \quad (2)$$

Here, the unknown coefficients w_{ij} (with the normalization $\sum_j w_{ij} = 1$) represent the probability of the decay from states in bin i to states in bin j. In other words, the w_{ij} values make up the weighting function for bin i, and contain the distribution of branching ratios as a function of γ-ray energy. Therefore, the weighting function w_i corresponds directly to the primary γ-ray spectrum h_i for bin i.

The coefficients n_{ij} are correcting factors for the different cross sections of populating levels in bin i and the underlying levels in bin j. They are determined so that the total area of each spectrum f_i multiplied by n_{ij} corresponds to the same number of cascades. This can be done in two ways [19]:

- Singles normalization. The singles-particle cross section is proportional to the number of events populating levels in a specific bin, and thus to the number of decay cascades from this bin. We denote the number of counts measured for bin i and j in the singles spectrum S_i and S_j, respectively. The normalization factor n_{ij} that should be applied to the spectrum f_j is then given by

$$n_{ij} = \frac{S_i}{S_j}. \quad (3)$$

- Multiplicity normalization. The average γ-ray multiplicity $\langle M \rangle$ can be obtained in the following way [21]: Assume an N-fold population of an excited level E. The decay from this level will result in N γ-ray cascades, where the ith cascade contains M_i γ rays. The average γ-ray energy $\langle E_\gamma \rangle$ is equal to the total energy carried by the γ rays divided by the total number of γ rays:

$$\langle E_\gamma \rangle = N \cdot \frac{E}{\sum_{i=1}^N M_i} = \frac{E}{\frac{1}{N}\sum_{i=1}^N M_i} = \frac{E}{\langle M \rangle}. \quad (4)$$

Then, the average γ-ray multiplicity is simply given by

$$\langle M \rangle = \frac{E}{\langle E_\gamma \rangle}. \quad (5)$$

The average γ-ray multiplicity $\langle M_i \rangle$ can thus easily be calculated for each excitation-energy bin i. Let the area (or total number of counts) of the γ-ray spectrum f_i be denoted by $A(f_i)$. Then the singles particle cross section S_i is proportional to the ratio $A(f_i)/\langle M_i \rangle$, and the normalization coefficient n_{ij} that should be applied to bin i when subtracting bin j is

$$n_{ij} = \frac{A(f_i)/\langle M_i \rangle}{A(f_j)/\langle M_j \rangle} = \frac{\langle M_j \rangle A(f_i)}{\langle M_i \rangle A(f_j)}. \quad (6)$$

The two normalization methods give normally the same results within the experimental error bars[2], see also Sec. III B. The resulting primary γ-ray matrix of ^{50}V is shown in Fig. 4 (right panel), using the singles normalization method.

In cases where the multiplicity is well determined, an area consistency check can be applied to Eq. (1). Assume that a small correction is introduced by substituting g_i by δg_i, where δ is close to unity. The area of the first-generation γ spectrum is then

$$A(h_i) = A(f_i) - \delta A(g_i), \quad (7)$$

and this corresponds to a γ-ray multiplicity of one unit. Since the number of primary γ rays in the spectrum f_i equals $A(f_i)/\langle M_i \rangle$, $A(h_i)$ is also given by

$$A(h_i) = A(f_i)/\langle M_i \rangle. \quad (8)$$

Combining Eqs. (7) and (8) yields

$$\delta = (1 - 1/\langle M_i \rangle)\frac{A(f_i)}{A(g_i)}. \quad (9)$$

The δ parameter can be varied to get the best agreement of the areas $A(h_i)$, $A(f_i)$ and $A(g_i)$ within the following restriction: $\delta = 1.00 \pm 0.15$; that is, the correction should not exceed 15%. If a larger correction is necessary, then improved weighting functions should be determined instead.

As mentioned before, the weighting coefficients w_{ij} correspond directly to the first-generation spectrum h_i, and this close relationship makes it possible to determine w_{ij} (and thus h_i) through a fast converging iteration procedure [19]:

[2] In case of the presence of isomeric states, the multiplicity method must be used to get the correct normalization.

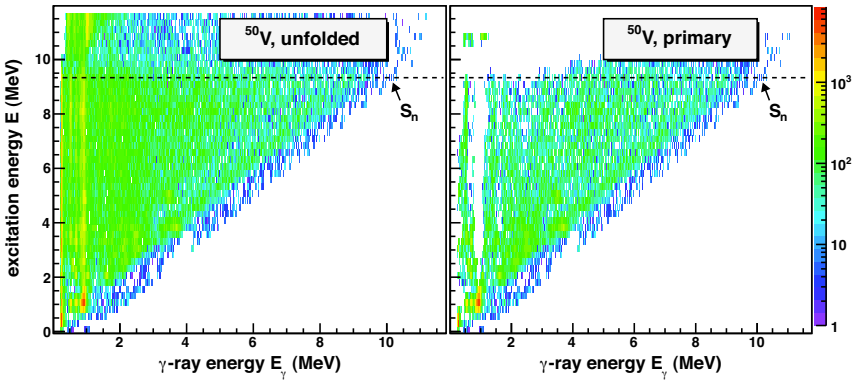

FIG. 4: (Color online). Excitation-energy vs. γ-ray energy matrix (left), and primary γ-ray matrix (right) for ^{50}V. The data are taken from the experiment presented in Ref. [13].

1. Apply a trial function for w_{ij}.

2. Deduce h_i.

3. Transform h_i to w_{ij} by giving h_i the same energy calibration as w_{ij}, and normalize the area of h_i to unity.

4. If w_{ij}(new) $\approx w_{ij}$(old), convergence is reached, and the procedure is finished. Otherwise repeat from step 2.

The first trial function could be the unfolded spectrum f_i, or a theoretical estimate based on a model for the level density and γ-ray transmission coefficient, or a constant function; it turns out that the resulting first-generation spectra are not sensitive to the starting trial function. Also, previous tests of the convergence properties of the procedure have shown that excellent agreement is achieved between the exact solution (from simulated spectra) and the trial function w_{ij} already after three iterations [19]. Usually, about $10-20$ iterations are performed on experimental spectra.

C. Determining level density and γ-ray strength

Once the primary γ-ray spectra are obtained for each excitation energy, the first-generation matrix $P(E,E_\gamma)$ is used for the determination of level density and γ-ray strength. For statistical γ-decay, the decay probability (given by $P(E,E_\gamma)$) of a γ-ray with energy E_γ decaying from a specific excitation energy E is proportional to the level density $\rho(E_\mathrm{f})$ at the final excitation energy $E_\mathrm{f} = E - E_\gamma$, and the γ-ray transmission coefficient $\mathscr{T}(E_\gamma)$:

$$P(E,E_\gamma) \propto \rho(E_\mathrm{f})\mathscr{T}(E_\gamma). \qquad (10)$$

The above relation holds for decay from *compound states*, which means that the relative probability for decay into any specific set of final states is independent on how the compound nucleus was formed. Thus, the nuclear reaction can be described as a two-stage process, where a compound state is first formed before it decays in a manner that is independent of the mode of formation [22, 23]. This is believed to be fulfilled at high excitation energy, even though direct reactions are used, as already discussed previously. Equation (10) can also be compared with Fermi's golden rule:

$$\lambda = \frac{2\pi}{\hbar}\left|\langle \mathrm{f}|\hat{H}_\mathrm{int}|\,\mathrm{i}\rangle\right|^2 \rho(E_\mathrm{f}), \qquad (11)$$

where λ is the decay rate of the initial state $|\mathrm{i}\rangle$ to the final state $|\mathrm{f}\rangle$, and $\hat{H}_\mathrm{int}$ is the transition operator. In Eq. (10), an ensemble of initial and final states within each excitation-energy bin is considered, and thus we obtain here the average decay properties of a set of initial states to a set of final states. Note, however, that in contrast to Fermi's golden rule where the matrix element is strictly dependent on the initial and final state, the transmission coefficient $\mathscr{T}$ is only dependent on the γ-ray energy and neither the initial nor the final excitation energy. This is in accordance with the Brink hypothesis [24], which states that the collective giant dipole mode built on excited states has the same properties as if built on the ground state. In its generalized form, this hypothesis includes all types of collective decay modes. Assuming that this hypothesis holds, the first-generation matrix $P(E,E_\gamma)$ is separable into two functions ρ and $\mathscr{T}$ as given in Eq. (10).

To extract the level density and the γ-ray transmission coefficient, an iterative procedure [25] is applied to the first-generation matrix $P(E,E_\gamma)$. The basic idea of this method is to minimize

$$\chi^2 = \frac{1}{N_\mathrm{free}} \sum_{E=E^\mathrm{min}}^{E^\mathrm{max}} \sum_{E_\gamma=E_\gamma^\mathrm{min}}^{E} \left(\frac{P_\mathrm{th}(E,E_\gamma) - P(E,E_\gamma)}{\Delta P(E,E_\gamma)} \right)^2, \qquad (12)$$

where N_free is the number of degrees of freedom, and

$\Delta P(E,E_\gamma)$ is the uncertainty in the experimental first-generation γ-ray matrix. The fitted first-generation γ-ray matrix $P_{\rm th}(E,E_\gamma)$ can theoretically be approximated by

$$P_{\rm th}(E,E_\gamma) = \frac{\rho(E-E_\gamma)\mathscr{T}(E_\gamma)}{\sum_{E_\gamma=E_\gamma^{\rm min}}^{E}\rho(E-E_\gamma)\mathscr{T}(E_\gamma)}. \quad (13)$$

The experimental matrix of first-generation γ rays is normalized [25] such that for every excitation-energy bin E, the sum over all γ energies E_γ from some minimum value $E_\gamma^{\rm min}$ to the maximum value $E_\gamma^{\rm max} = E$ at this excitation-energy bin is unity:

$$\sum_{E_\gamma=E_\gamma^{\rm min}}^{E} P(E,E_\gamma) = 1. \quad (14)$$

The experimental matrix $P(E,E_\gamma)$ and the fitted matrix $P_{\rm th}(E,E_\gamma)$ of ^{46}Ti are displayed in Fig. 5. The energy limits set in the first-generation matrix for extraction are also shown. These limits ($E^{\rm min}$, $E^{\rm max}$, and $E_\gamma^{\rm min}$) are chosen to ensure that the data utilized are from the statistical excitation-energy region and that no γ-lines stemming from, e.g., yrast transitions, are used in the further analysis. Note that the γ-ray energy bins are now re-binned to the same size (120 keV in this case) as the excitation-energy bins.

Each point of the ρ and $\mathscr{T}$ functions is assumed to be an independent variable, so that the reduced χ^2 of Eq. (12) is minimized for every argument $E-E_\gamma$ and E_γ. The quality of the procedure when applied to ^{46}Ti and ^{163}Dy is shown in Figs. 6 and 7, where the experimental first-generation spectra for various initial excitation energies are compared to the least-χ^2 solution. In general, the agreement between the experimental data and the fit is very good. Note, however, that differences of several standard deviations do occur. In the case of ^{46}Ti, this is particularly pronounced for the peaks at $E_\gamma \approx 4.7$ MeV for $E = 5.6$ MeV and $E_\gamma \approx 5.5$ MeV for $E = 6.4$ MeV. As these peaks correspond to the decay to the first excited state, one might expect large Porter-Thomas fluctuations [26] in the strength of these transitions.

The global fitting to the data points only gives the functional form of ρ and $\mathscr{T}$. In fact, it has been shown [25] that if one solution for the multiplicative functions ρ and $\mathscr{T}$ is known, one may construct an infinite number of other functions, which give identical fits to the $P(E,E_\gamma)$ matrix by

$$\tilde{\rho}(E-E_\gamma) = A\exp[\alpha(E-E_\gamma)]\rho(E-E_\gamma), \quad (15)$$
$$\tilde{\mathscr{T}}(E_\gamma) = B\exp(\alpha E_\gamma)\mathscr{T}(E_\gamma). \quad (16)$$

Therefore the transformation parameters α, A and B, which correspond to the physical solution, must be found from external data.

D. Normalization

In order to determine the correction α to the slope of the level density and the γ-ray transmission coefficient, and to determine the absolute value A of the level density in Eq. (15), the ρ function is adjusted to fit the number of known discrete levels at low excitation energy and neutron (or proton) resonance data at high excitation energy. This normalization is shown for ^{164}Dy in Fig. 8. The data point at high excitation energy (open square in Fig. 8) is calculated in the following way according to Ref. [25]. The starting point is Eqs. (4) and (5) of Ref. [27]:

$$\rho(U,J) = \frac{\sqrt{\pi}}{12}\frac{\exp(2\sqrt{aU})}{a^{1/4}U^{5/4}}\frac{(2J+1)\exp\left[-(J+1/2)^2/2\sigma^2\right]}{2\sqrt{2\pi}\sigma^3}, \quad (17)$$

and

$$\rho(U) = \frac{\sqrt{\pi}}{12}\frac{\exp(2\sqrt{aU})}{a^{1/4}U^{5/4}}\frac{1}{\sqrt{2\pi}\sigma}, \quad (18)$$

where $\rho(U,J)$ is the level density for a given spin J, and $\rho(U)$ is the level density for all spins. The intrinsic excitation energy U, the level-density parameter a, and the spin cutoff parameter σ are normally taken from Ref. [28] in previous works, or from Ref. [29] in recent works.

Now, let I_t be the spin of the target nucleus in a neutron resonance experiment. The average neutron resonance spacing $D_{\ell=0}$ for s-wave neutrons can be written as

$$\frac{1}{D_0} = \frac{1}{2}\left[\rho(S_n,J=I_t+1/2)+\rho(S_n,J=I_t-1/2)\right], \quad (19)$$

because all levels with spin $J = I_t \pm 1/2$ are accessible in neutron resonance experiments, and because it is assumed that both parities contribute equally to the level density at the neutron separation energy S_n. Combining Eqs. (17)–(19) with $U = S_n$, one finds the total level density at the neutron separation energy to be

$$\rho(S_n) = \frac{2\sigma^2}{D_0}\cdot\frac{1}{(I_t+1)\exp\left[-(I_t+1)^2/2\sigma^2\right]+I_t\exp\left[-I_t^2/2\sigma^2\right]}. \quad (20)$$

Note also that the resonance spacing between p-waves, D_1, could also be used for calculating $\rho(S_n)$, see Ref. [30].

Since our experimental data only reach up to excitation energies around $S_n - E_\gamma^{\rm min}$, an interpolation has been made between the Oslo data and $\rho(S_n)$ using the back-shifted Fermi gas model of Refs. [28, 29], as shown in Fig. 8. It should be noted that in most cases the gap between the data and $\rho(S_n)$ is small, so that the normalization is not very sensitive to the interpolation; a pure exponential function of the type $\rho(E) = C_0\exp(C_1E)$, where C_0 and C_1 are fitting parameters, gives an interpolation of equally good agreement (see Ref. [9]).

The slope of the γ-ray transmission coefficient $\mathscr{T}(E_\gamma)$ has already been determined through the normalization of the level density, as explained above. The remaining constant B in Eq. (16) gives the absolute normalization of $\mathscr{T}$, and it is determined using information from neutron resonance decay on the average total radiative width $\langle\Gamma_\gamma\rangle$ at S_n according to Ref. [31].

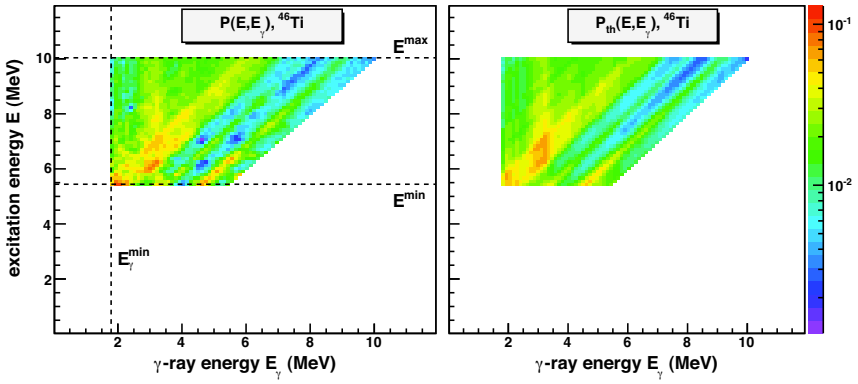

FIG. 5: (Color online). Experimental first-generation matrix $P(E,E_\gamma)$ (left) and the calculated $P_{\rm th}(E,E_\gamma)$ (right) of ^{46}Ti from the iteration procedure of A. Schiller *et al*. [25]. The dashed lines show the limits set in the experimental first-generation matrix for the fitting procedure. The data are taken from the experiment presented in Ref. [15].

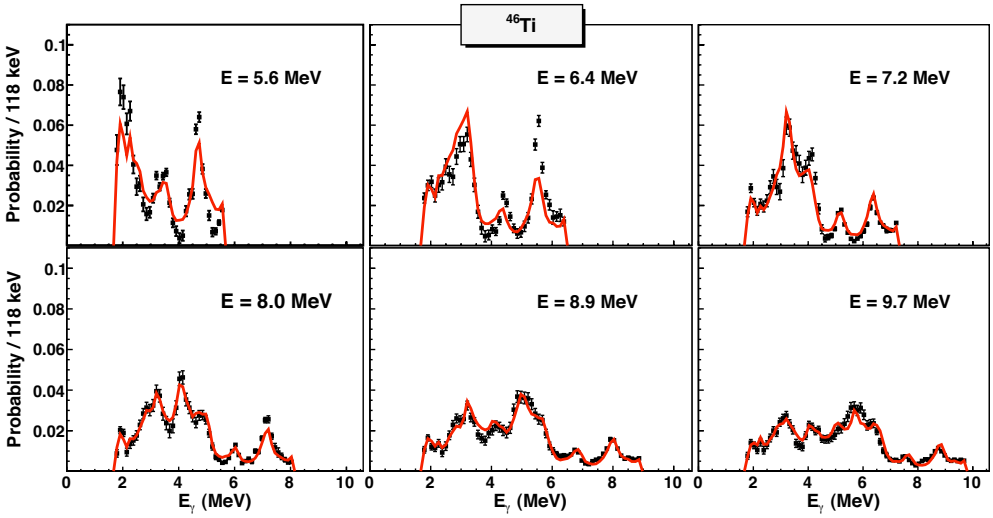

FIG. 6: (Color online). Experimental first-generation γ spectra (data points with error bars) at six different initial excitation energies (indicated in the figure) compared to the χ^2 fit (solid lines) for ^{46}Ti. The fit is performed simultaneously on the entire first-generation matrix of which the six displayed spectra are a fraction. The data are taken from the experiment presented in Ref. [15].

The starting point is Eq. (3.1) of Ref. [32],

$$\langle\Gamma_\gamma(E,J,\pi)\rangle = \frac{1}{2\pi\rho(E,J,\pi)}\sum_{XL}\sum_{J_{\rm f},\pi_{\rm f}}\int_{E_\gamma=0}^{E} {\rm d}E_\gamma \mathscr{T}_{XL}(E_\gamma) \times \rho(E-E_\gamma,J_{\rm f},\pi_{\rm f}), \quad (21)$$

where $\langle\Gamma_\gamma(E,J,\pi)\rangle$ is the average total radiative width of levels with energy E, spin J and parity π. The summation and integration are going over all final levels with spin $J_{\rm f}$ and parity $\pi_{\rm f}$ that are accessible through γ transitions with energy E_γ, electromagnetic character X and multipolarity L. Assuming that the main contribution to the experimental $\mathscr{T}$ is from dipole radiation ($L=1$), we get

$$B\mathscr{T}(E_\gamma) = B\sum_{XL}\mathscr{T}_{XL}(E_\gamma) \approx B\left[\mathscr{T}_{\rm E1}(E_\gamma)+\mathscr{T}_{\rm M1}(E_\gamma)\right], \quad (22)$$

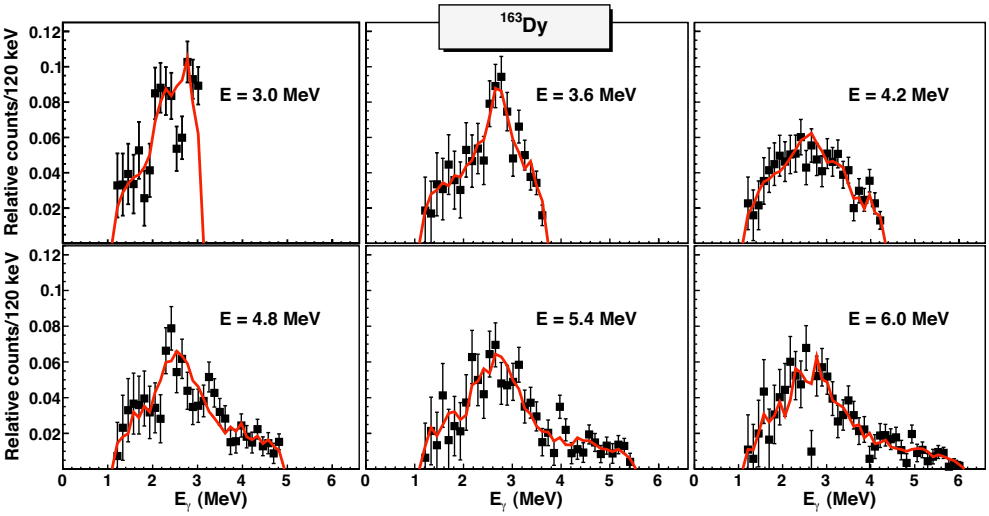

FIG. 7: (Color online). Same as Fig. 6 for ^{163}Dy. The data are taken from the experiment presented in Ref. [5].

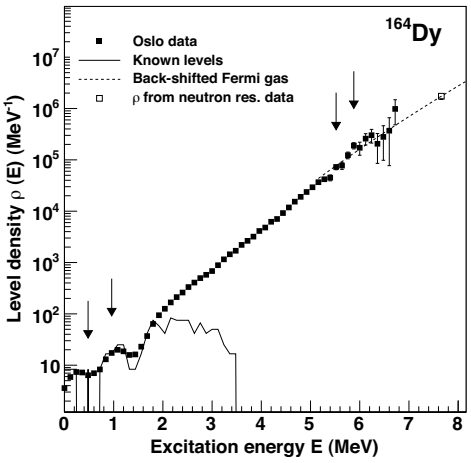

FIG. 8: Normalization procedure of the level density (data points) of ^{164}Dy. The data points between the arrows are normalized to known levels at low excitation energy (solid line) and to the level density at the neutron separation energy (open square) using an interpolation with the Fermi-gas level density (dashed line). The data are taken from the experiment presented in Ref. [5].

from which the total, experimental γ-ray strength function can easily be calculated:

$$f(E_\gamma) = \frac{1}{2\pi E_\gamma^3} B\mathscr{T}(E_\gamma), \tag{23}$$

from the relation between γ-ray strength function and γ-ray transmission coefficient [33]:

$$\mathscr{T}_{XL}(E_\gamma) = 2\pi E_\gamma^{(2L+1)} f_{XL}(E_\gamma)\,. \tag{24}$$

Further, we also assume that there are equally many accessible levels with positive and negative parity for any excitation energy and spin, so that the level density is given by

$$\rho(E-E_\gamma, J_\mathrm{f}, \pm\pi_\mathrm{f}) = \frac{1}{2}\rho(E-E_\gamma, J_\mathrm{f}). \tag{25}$$

Now, by combining Eqs. (21), (22) and (25), the average total radiative width of neutron s-wave capture resonances with spins $I_t \pm 1/2$ expressed in terms of the experimental $\mathscr{T}$ is obtained:

$$\langle\Gamma_\gamma(S_n, I_t \pm 1/2, \pi_t)\rangle = \frac{B}{4\pi\rho(S_n, I_t \pm 1/2, \pi_t)} \int_{E_\gamma=0}^{S_n} \mathrm{d}E_\gamma \mathscr{T}(E_\gamma) \times \rho(S_n - E_\gamma) \sum_{J=-1}^{1} g(S_n - E_\gamma, I_t \pm 1/2 + J), \tag{26}$$

where I_t and π_t are the spin and parity of the target nucleus in the (n,γ) reaction, and $\rho(S_n - E_\gamma)$ is the experimental level density. Note that the factor $1/\rho(S_n, I_t \pm 1/2, \pi_t)$ equals the neutron resonance spacing D_0. The spin distribution of the level density is assumed to be given by [27]:

$$g(E,J) \simeq \frac{2J+1}{2\sigma^2} \exp\left[-(J+1/2)^2/2\sigma^2\right]. \tag{27}$$

The spin distribution is normalized so that $\sum_J g(E,J) \approx 1$. The experimental value of $\langle \Gamma_\gamma \rangle$ at S_n is then the weighted sum of the level widths of states with $I_i \pm 1/2$ according to Eq. (26). From this expression the normalization constant B can be determined as described in Ref. [31]. However, some considerations must be done before normalizing according to Eq. (26).

Methodical difficulties in the primary γ-ray extraction prevent determination of the function $\mathscr{T}(E_\gamma)$ for $E_\gamma < E_\gamma^{\min}$ as discussed previously. In addition, the data at the highest γ-energies suffer from poor statistics. Therefore, $\mathscr{T}$ is extrapolated with an exponential function, as demonstrated for ^{51}V in Fig. 9. The contribution of the extrapolation to the total radiative width given by Eq. (26) does not normally exceed 15%, thus the errors due to a possibly poor extrapolation are of minor importance [31].

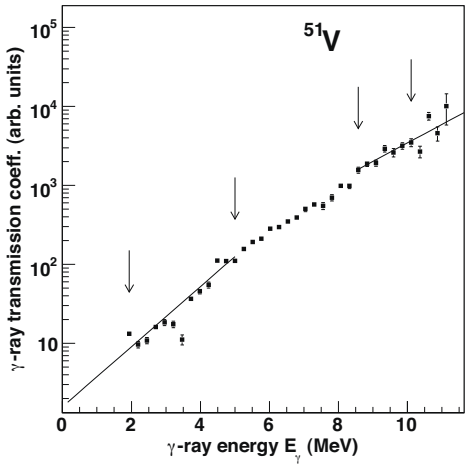

FIG. 9: Extrapolation of the γ-ray transmission coefficient of ^{51}V. The data points between the arrows in the low and high γ-energy regions are utilized to fit the exponential functions to the data. The data are taken from the experiment presented in Ref. [13].

III. UNCERTAINTIES AND POSSIBLE SYSTEMATIC ERRORS

In the following, we will go through the Oslo method step by step with a close look at the uncertainties and possible systematic errors connected to it.

A. Unfolding of γ-ray spectra

The unfolding method is described in great detail in Ref. [18]. The method is based on a successive subtraction-iteration technique in combination with a special treatment of the Compton background. The stability of the method has

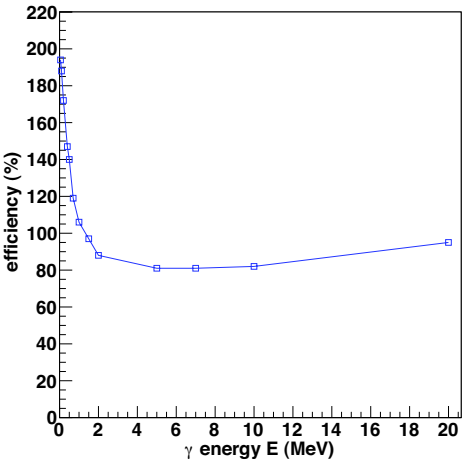

FIG. 10: (Color online). Efficiencies relative to the 1.33-MeV efficiency used in the unfolding method.

been extensively tested in previous works and has proven to be very robust and reliable (see, e.g., Refs. [13, 14, 30]). To some extent also the impact of slightly erroneous response functions has been investigated in Ref. [23]. As this is the part of the method that has the largest potential of influencing the final results, it is further addressed here.

In the unfolding method, the γ-ray spectra are corrected for the total absorption efficiency of the NaI crystals for a given γ energy. The applied efficiencies (normalized to the efficiency at 1.33 MeV) are shown in Fig. 10.

We have tested the effect of reducing these efficiencies by up to $\approx 20\%$ for γ energies above 1 MeV, using simulated particle-γ coincidences generated with the DICEBOX code [34]. In the DICEBOX algorithm, a complete decay scheme of an artificial nucleus is generated. In this case we have considered an artificial nucleus resembling ^{57}Fe. Below an excitation energy of about 2.2 MeV, all information from the known decay scheme is used; above this energy the levels and decay properties are generated from a chosen model of the level density and γ-ray strength function. The code allows to take into account Porter-Thomas fluctuations of the individual transition intensities as well as assumed fluctuations in the actual density of levels. Each particular set of the level scheme and the decay intensities is called a *nuclear realization*. For more details see Ref. [34]. A restriction on the spin distribution of the initial excitation-energy levels of $1/2 \leq J \leq 13/2$ was applied, and the chosen bin size was 120 keV. In these simulations, each level in a bin was populated with the same probability independently of its spin and parity. This means that Porter-Thomas fluctuations were not considered in the population of levels via the direct population, but only in the γ decay.

The results on the extracted level density and γ-ray strength

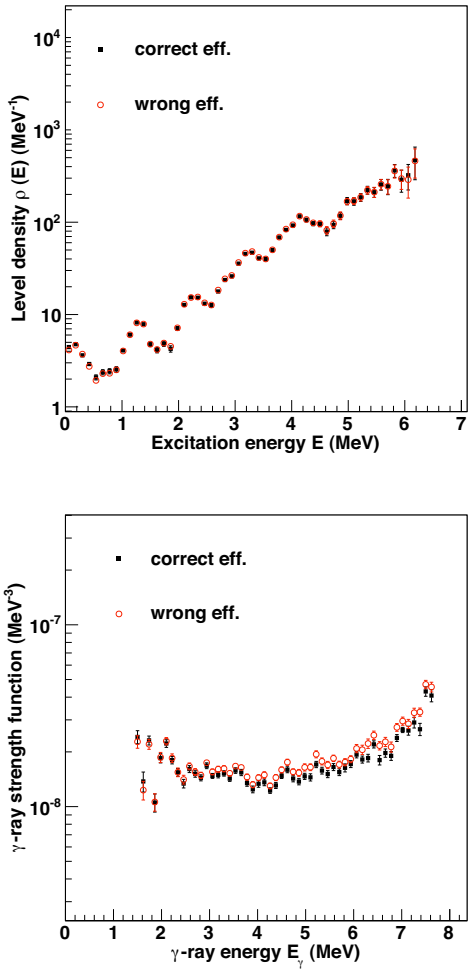

FIG. 11: (Color online). Test of sensitivity on the total γ efficiency on the level density (top) and γ-ray strength function (bottom) extracted from simulated data.

function are shown in Fig. 11. It is seen that the level density is not very sensitive to the total efficiency, but the slope of the γ-ray strength function is increased when using a too low efficiency for the high-energy γ rays, thus leading to a too large correction in the unfolding procedure. However, it is very gratifying that the overall shape is indeed preserved, and the deviation in absolute value of the two γ-ray strength functions does not exceed 20%, corresponding to the maximum change in the absolute efficiency.

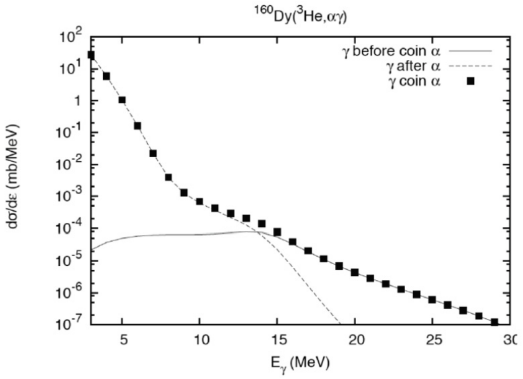

FIG. 12: Calculated γ-ray spectra from the ^{160}Dy(^{3}He,$\alpha\gamma$) reaction at 45 MeV [35]. The solid line shows the pre-equilibrium component of the total γ-ray spectrum (γ before α), the dashed line represents the equilibrium part (α before γ), and the filled squares give the total spectrum.

B. The first-generation method

The first-generation method, which is applied to extract the distribution of primary γ rays from each excitation-energy bin, is a sequential subtraction technique where an iterative procedure is applied to determine the weighting coefficients w_{ij}, which correspond to the primary γ-ray spectrum as described in Sec. II B.

The main assumption of the first-generation method is that the γ decay from any excitation-energy bin is independent on how the nucleus was excited to this bin. In other words, the decay routes are the same whether they were initiated directly by the nuclear reaction or by γ decay from higher-lying states, giving rise to the same shape of the γ spectra. This assumption is automatically fulfilled when states have the same cross section to be populated by the two processes, since γ branching ratios are properties of the levels themselves.

In the region of high level density, the nucleus seems to attain a compound-like system before emitting γ rays even though direct reactions are utilized. This is due to two factors. First, a significant configuration mixing of the levels will appear when the level spacing is comparable to the residual interaction. Second, the reaction time, and thus the time it takes to create a complete compound state, is $\approx 10^{-18}$s, while the typical life time of states in the quasi-continuum is $\approx 10^{-15}$s. Therefore, it is reasonable to assume that the nucleus has thermalized prior to γ decay. This is supported by recent calculations [35] based on the Iwamoto-Harada-Bispinghoff model, showing that for the ^{160}Dy(^{3}He,$\alpha\gamma$) reaction with a 45-MeV ^{3}He beam, the pre-equilibrium ("direct") component of the γ-ray spectra is very small for γ energies below ≈ 10 MeV (see Fig. 12). The same is true for the ^{46}Ti$(p,p'\gamma)$ reaction with proton beam energy $E_p = 15$ MeV, see Fig. 13. Note that the "direct" component is calculated using the pre-equilibrium (i.e. statistical) formalism.

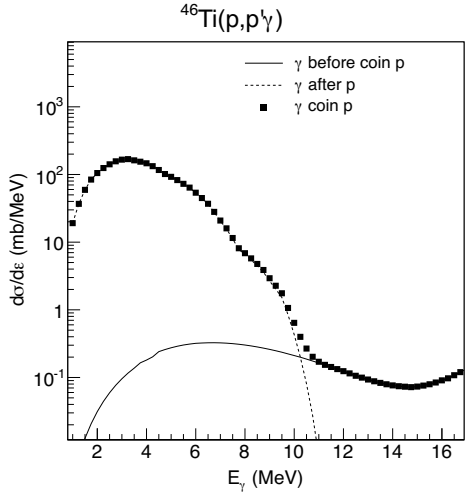

FIG. 13: Same as Fig. 12, but for the inelastic scattering ^{46}Ti$(p,p'\gamma)$ at $E_p = 15$ MeV.

Experimentally, the independence of the reaction mechanism has been tested by creating the same compound nucleus with the two different reactions (^{3}He,α) and (^{3}He,^{3}He'). This has been done for, e.g., ^{96,97}Mo [12], ^{161,162}Dy [4], and ^{171,172}Yb [3]. One observes an excellent agreement with the level density and γ-ray strength function resulting from the two reactions within the experimental error bars. However, at very low excitation energies, there is a significant difference in the obtained level density: the inelastic scattering gives consistently a higher level density close to the ground state than does the pick-up reaction. This could be a sign that the inelastic scattering populates states with wave functions having a large overlap with the ground state and the low-lying excited states. Thus, the decay to the ground state and low-lying states will be very fast, and cannot be characterized as compound decay.

The region at low excitation energies can be tricky also in other aspects. Vertical ridges and/or valleys can occur in the primary γ-ray matrix as a consequence of differences in feeding of these discrete states, giving significantly different shapes of the γ spectra at low E compared to higher excitation energies. The direct reaction cross section depends strongly on the intrinsic wave functions of low lying states, as seen in the particle spectra in Figs. 1–3. One can encounter the situation where some of these states are very weakly populated in the reaction, but strongly fed through decay from above-lying states. This means that some higher-order γ rays are not fully subtracted in the first-generation method, giving an erroneous primary γ-ray spectrum for low E_γ. On the other hand, the reaction might populate very strongly some low-lying states that are more moderately populated by decay from above. One can then subtract too much of the γ rays from these states.

The latter case is demonstrated for ^{50}V in the right panel of Fig. 4. A state at excitation energy 910 keV with spin/parity 7^+ decaying 100% to the ground state, is strongly populated in the neutron pick-up reaction, which favors high-ℓ transfer (here $\ell = 3$, see Ref. [36]). However, it is not so strongly populated by γ decay from above, and the result is that there is a vertical valley with zero counts in the primary γ-ray matrix at this γ energy.

Furthermore, it is important that the populated spin distribution is (at least approximately) independent on the excitation energy. Else, the bins at high excitation energy will contain decay from states with higher spin than the bins at lower excitation energy, again disturbing the low-energy part of the primary γ-ray spectra. For the ^{163}Dy(^{3}He, α)^{162}Dy reaction, the spin population has been extensively studied in Ref. [23] and references therein. In this specific case, the spin distribution turned out to be approximately constant in the excitation-energy region investigated. Also, for the lighter nuclei it is observed that indeed, the spins are populated with the same relative intensities within the error bars. This is seen for ^{50}V in the left panel of Fig. 4: the relative feeding to the low-lying states (vertical lines) is approximately the same for the whole quasi-continuum region. This is also the case for ^{46}Ti [15].

Another potential problem could arise from the finite detector resolution. To illustrate this, consider a first-generation γ-ray of 8 MeV, decaying from $E_i = 10$ MeV to $E_f = 2$ MeV. This γ-ray would typically have a resolution of ≈ 250 keV, while the particle resolution could be ≈ 150 keV (for 15-MeV protons). This means that the weighting function (see Sec. II B) for $E_f = 2$ MeV is about 100 keV broader than the excitation-energy resolution at this point. If the situation is that there is only one level within E_f, one could then "miss" some of the weighting function because it is broader than the particle peak. It could also be that the opposite situation applies: low-energy γ rays with, say, 50-keV resolution might decay to excitation energies with resolution ranging from $150-300$ keV, leading to too narrow weighting functions.

We have tested the effects of different resolutions by employing a very simple, artificial decay scheme, see Fig. 14. A hypothetical nucleus with three excited states at $E_1 = 3.5$ MeV, $E_2 = 6$ MeV, and $E_3 = 8$ MeV, was assumed to have the following decay scheme:

- from E_3: 30% γ_a, 20% γ_b, and 50% γ_c.
- from E_2: 67% γ_d, and 33% γ_e.
- from E_1: 100% γ_f.

The γ-ray energies involved are: $\gamma_a = 2.0$ MeV, $\gamma_b = 4.5$ MeV, $\gamma_c = 8.0$ MeV, $\gamma_d = 2.5$ MeV, $\gamma_e = 6.0$ MeV, and $\gamma_f = 3.5$ MeV. The first-generation γ rays from E_3 are then γ_a, γ_b, and γ_c, from E_2 γ_d and γ_e, and from E_1 γ_f.

Applying no smoothing for all excitation energies, i.e., the γ-ray peaks are δ functions, the exact result is obtained from the first-generation method. Then, we assume 200-keV resolution for all excitation energies, but with an energy-dependent resolution of the γ-ray spectrum with 50-keV resolution for 1-MeV γ rays and 300-keV resolution for 9-MeV γ rays, similar to the experimental conditions. This constructed

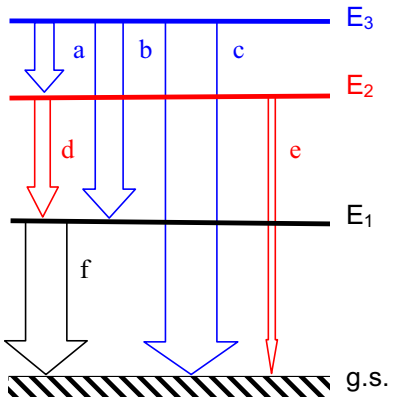

FIG. 14: (Color online). Hypothetical decay scheme of an artificial nucleus (see text).

matrix is shown in Fig. 15. When applying the first-generation method on this smoothed matrix, we get the result shown in the lower part of Fig. 15. It is seen that it is not exact any more, but the differences are small. For example, for $E_3 = 8$ MeV, γ_d is not a primary transition and should have been completely gone in the first-generation spectrum, but still about 5% of the counts in the original peak is present. For the γ_e and γ_f peaks, the situation is the same; also so for γ_f at $E_2 = 6$ MeV. This means that one might expect leftovers of higher-generation γ rays of the order of 5% in the primary spectra. Compared to values of experimental errors, which are typically within $5-30\%$, this is a relatively small effect (the error propagation is discussed in detail in Ref. [25]).

To check more thoroughly what effect possible errors in the first-generation method might have on the final results, namely the extracted level density and strength function, we have performed simulations with the generalized version of DICEBOX [34], as already discussed briefly in Sec. III A. Again, we have considered an artificial nucleus resembling ^{57}Fe, with a spin distribution of the initial excitation-energy levels of $1/2 \leq J \leq 13/2$, and bin size of 120 keV. Note also that equally many negative- and positive-parity states are assumed above the region of known, discrete levels.

First, the simulated spectra were folded with the CACTUS response functions, and also a Gaussian smoothing was applied giving a full width at half maximum (FWHM) of 250 keV for all excitation energies. These spectra were thus made to be as similar as possible to experimental spectra. Then, we applied the unfolding technique and the first-generation method to obtain the first-generation spectra. We then compared the extracted first-generation matrix with the true first-generation matrix from the simulations, after smoothing the true first-generation spectra with a resolution similar to the experimental one. Examples of two such matrices for one

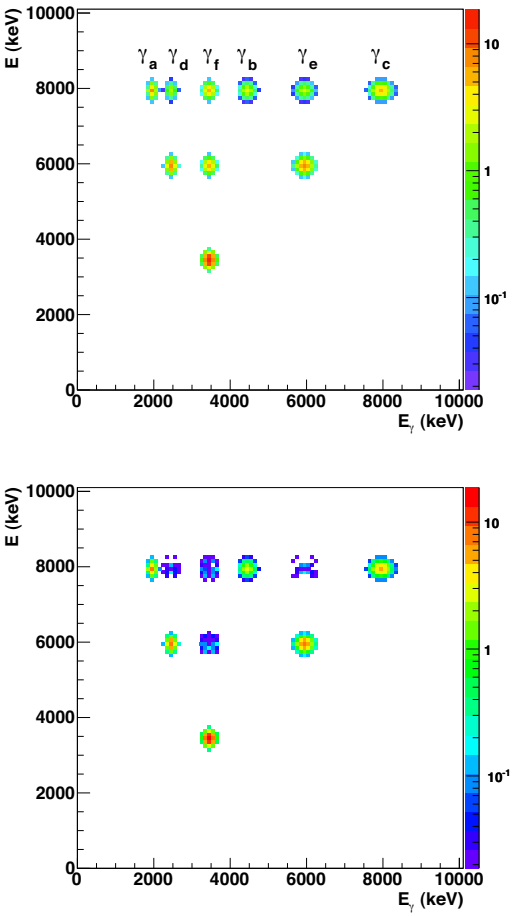

FIG. 15: (Color online). Matrix of energy levels and γ transitions in an artificial nucleus. Top: original matrix; bottom: result after the first-generation method is applied.

nuclear realization are shown in Fig. 16. The overall good similarity between the two matrices is gratifying. However, in the low-E_γ region, there are significant differences between the results extracted from the experiment-like matrix and the true, smoothed matrix. In particular, one can see that there are some vertical lines in the experiment-like first-generation matrix, e.g., for $E_\gamma \approx 1020$ keV, that are not present in the true matrix. This particular vertical ridge originates from the $7/2^-$ state at 1007 keV, which for this nuclear realization is strongly populated in the decay cascades at high excitation energy. However, at low excitation energies, which corresponds to the population from the direct reaction, this state is only moderately populated. Thus, its γ decay is not correctly sub-

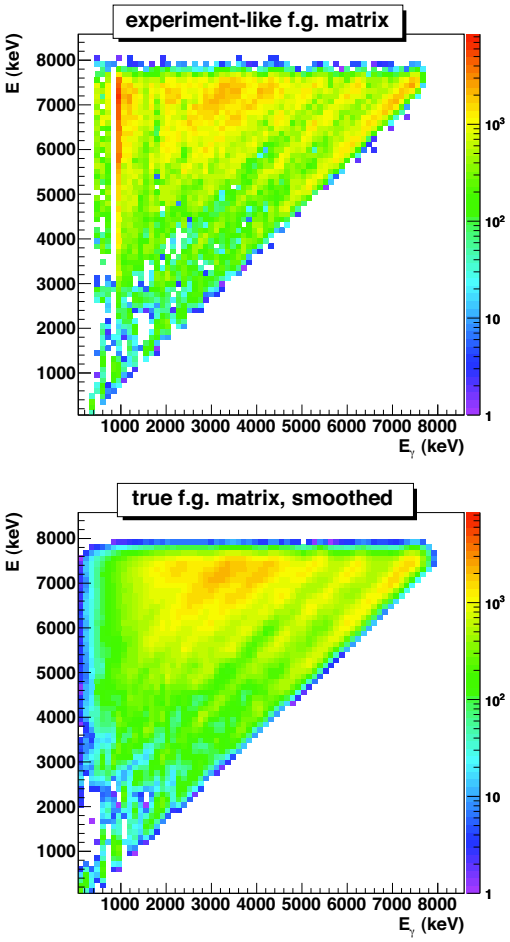

FIG. 16: (Color online). Simulated first-generation matrix for ^{57}Fe. Top: spectra from folded data set. Bottom: true spectra with smoothing similar to the experimental resolution.

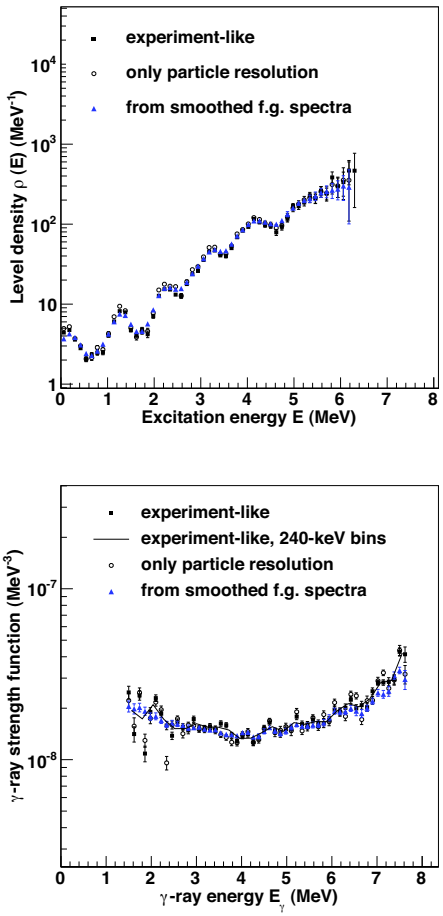

FIG. 17: (Color online). Results from simulated spectra on ^{57}Fe. Top: level density. Bottom: γ-ray strength function.

tracted in the first-generation procedure. It is therefore important to exclude such leftovers from higher-generation γ rays in the further analysis, as mentioned in Sec. II C.

We also tested the case with a Gaussian smoothing on the particle resolution, and the ideal response on the γ-detection side. The extracted level densities and strength functions for all three cases are displayed in Fig. 17. In general, the results agree very well. We note that there are larger fluctuations in the strength function extracted from the experiment-like matrix as well as the case where only the particle resolution is applied, especially in the region below $E_\gamma \approx 2.5$ MeV. These fluctuations are related to uncertainties in the first-generation subtraction procedure and could be due to small variations in the shape of the γ spectra. However, by compressing the experiment-like γ spectra by a factor of two (bin size of 240 keV), we obtain practically the same shape of the γ-ray strength function as from the true first-generation spectra (see Fig. 17).

Finally, we have tested the two normalization options (singles or multiplicity) of the first-generation method on experimental spectra to investigate the effect on the extracted level density and γ-ray strength function. The result for ^{51}V is shown in Fig. 18. We observe that the two options give very similar results, only a very few data points are outside the experimental error bars. It is clear that the two methods do not give any difference in the overall shape of neither the level density nor the strength function.

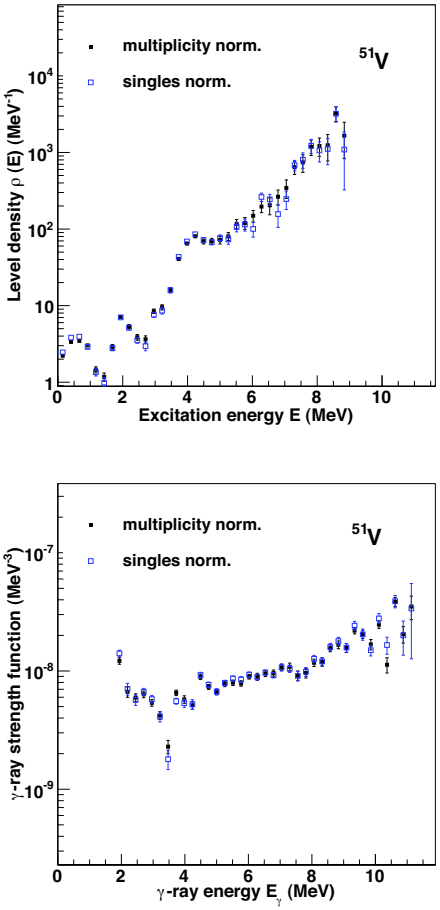

FIG. 18: (Color online). Test of the two normalization options in the first-generation method for ^{51}V. Top: level density. Bottom: γ-ray strength function. The data are taken from the experiment presented in Ref. [13].

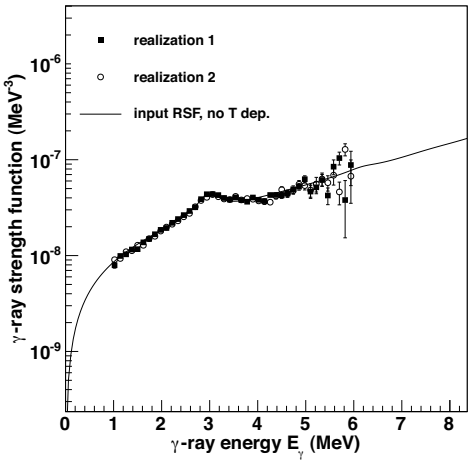

FIG. 19: Results from simulated spectra of the artificial nucleus ^{163}Dy. The extracted γ-ray strength functions are shown as black points and open circles for two different nuclear realizations, while the input γ-ray strength model is shown as a solid line.

C. The Brink hypothesis

The γ-ray transmission coefficient $\mathscr{T}(E_\gamma)$ in Eq. (10) is assumed to be independent of excitation energy (and thus nuclear temperature) according to the generalized Brink hypothesis [24], as discussed in Sec. II C. This hypothesis is violated when high temperatures and/or spins are involved in the nuclear reactions, as shown for giant dipole excitations (see Ref. [37] and references therein). However, since both the temperature reached and the spins populated are rather low for the Oslo experiments, these dependencies are usually assumed to be of minor importance in the relatively low excitation-energy region considered here.

The effect of the Brink hypothesis has been tested by analyzing simulated spectra on an artificial nucleus resembling ^{163}Dy. The simulations were again performed with the DICEBOX code [34] for a specific spin range on the initial excited levels, $1/2 \leq J \leq 13/2$.

As a first step, a temperature-independent model for the γ-ray strength function was used as input for the simulations. The extracted and input γ-ray strength function are shown in Fig. 19. As expected, the Oslo method works very well in this case.

In the next test, a temperature-dependent input γ-ray strength function was used, with temperature $T \propto \sqrt{E_f}$. In principle, it is not possible to disentangle the input level density and γ-ray strength function anymore, since now we have

$$P(E,E_\gamma) \propto \rho(E_f)\mathscr{T}(E_f,E_\gamma). \quad (28)$$

This we keep in mind when we use the procedure of Ref. [25] in order to extract the level density and γ-ray strength function.

The extracted γ-ray strength functions for two different nuclear realizations are shown in Fig. 20, within the excitation-energy range $2.1 < E < 6.2$ MeV. It is seen that the extracted γ-ray strength function lies in between the two extremes of the temperature-dependent input model, and thus an average strength function for the excitation energy region under study is found. The shape of the extracted γ-ray strength function is therefore quite reasonable, although it is clear that the low-energy part with $1 \leq E_\gamma \leq 2.5$ MeV must necessarily be quite different from the two extremes of the input.

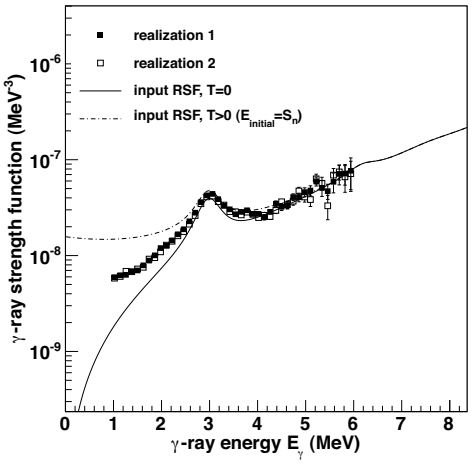

FIG. 20: Results from simulated spectra of ^{163}Dy. The extracted γ-ray strength functions are displayed as black and open squares for two different nuclear realizations. The input γ-ray strength function models for $T_f = 0$ (solid line) and $T_f \propto \sqrt{(S_n - E_\gamma)}$ (dashed-dotted line) are also shown.

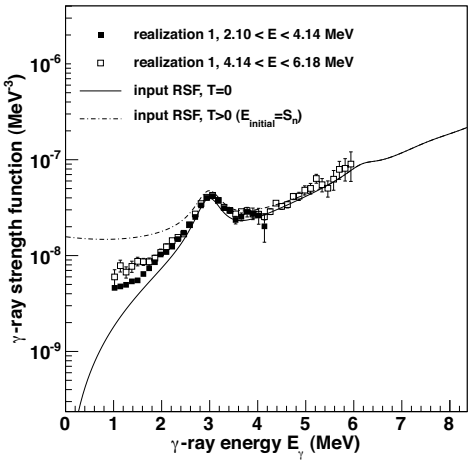

FIG. 21: Results from simulated spectra of the artificial nucleus ^{163}Dy. The extracted γ-ray strength functions for two excitation-energy regions are displayed as black and open squares. The input γ-ray strength function models for $T_f = 0$ (solid line) and $T_f \propto \sqrt{(S_n - E_\gamma)}$ (dashed-dotted line) are also shown.

This is further illustrated in Fig. 21, where we have extracted the γ-ray strength function for two separate excitation-energy regions: $2.1 < E < 4.1$ MeV and $4.1 < E < 6.2$ MeV. It is easily seen that the γ-ray strength function for γ energies between $\approx 1-2$ MeV is different in the two cases; the higher excitation energies lead to a higher temperature of the final states and thus a higher strength function.

However, one should keep in mind that the experimental γ-ray strength functions have been tested against the assumption of temperature dependence for many nuclei, e.g., ^{45}Sc [14], ^{56,57}Fe [10], ^{96,98}Mo [12], and ^{117}Sn [8]. This is also shown for ^{164}Dy [5] in Fig. 22, where the γ-ray strength function has been extracted for three sets of initial excitation energies. As can be seen from the figure, the similarity of the three γ-ray strength functions is striking. There is, therefore, no experimental evidence in this excitation-energy region for a strong temperature dependence in the strength function. Hence, the Brink hypothesis seems to be valid here.

D. The parity distribution

As mentioned previously, for both the normalization of the level density and the γ-ray transmission coefficient, the assumption of equally many levels with positive and negative parity is used. We will in the following investigate this assumption in detail.

Using ρ_+ and ρ_- to denote the level density with positive and negative parity levels, the parity asymmetry α is defined as [38]

$$\alpha = \frac{\rho_+ - \rho_-}{\rho_+ + \rho_-}, \tag{29}$$

which gives -1 and 1 for only negative and positive parities, respectively, and 0 when both parities are equally represented.

Another expression widely used in literature is the ratio ρ_-/ρ_+, which relates to α by

$$\frac{\rho_-}{\rho_+} = \frac{1-\alpha}{1+\alpha}. \tag{30}$$

We have considered theoretical parity distributions from combinatorial plus Hartree-Fock-Bogoliubov calculations of spin- and parity-dependent level densities [39]. Applying the definition in Eq. (29), we find the calculated parity distributions for several Fe, Mo, and Dy isotopes as shown in Figs. 23–25. As one might expect from the fact that more orbits are accessible at increasing excitation energy, the parity distributions are seen to approach zero as the excitation energy increases. However, it is clear that for the lighter nuclei, in particular the Fe isotopes, the assumption of zero parity asymmetry is not fulfilled in the calculations for excitation energies below ≈ 10 MeV.

We have also looked at other theoretical work such as shell-model Monte Carlo calculations [40] and macroscopic-microscopic calculations [41]. In Fig. 2 of Ref. [41], the ratio ρ_-/ρ_+ is shown for ^{56}Fe, indicating a value of $\rho_-/\rho_+ \simeq 0.1$ at 10 MeV excitation energy. From Fig. 4 in Ref. [40], the

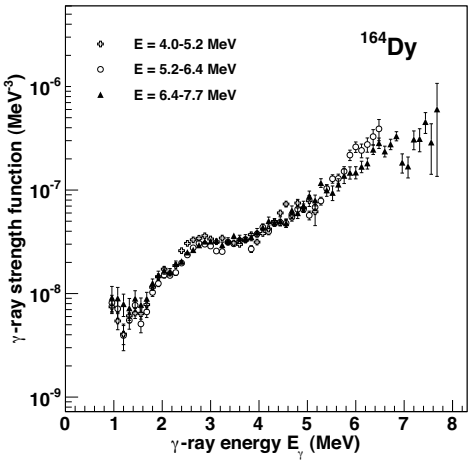

FIG. 22: Experimental γ-ray strength function of ^{164}Dy for three sets of initial excitation energies. The data are taken from the experiment presented in Ref. [5].

ratio $\rho_-/\rho_+ \simeq 0.2$ for $E = 10$ MeV. In contrast to this, the combinatorial calculations of Ref. [39] give $\rho_-/\rho_+ \simeq 0.7$ at $E = 10$ MeV, which is also in accordance with other microscopic calculations based on the Nilsson model and BCS quasi-particles [11], where $\rho_-/\rho_+ \simeq 0.5$. These results indicate considerably more negative-parity states in ^{56}Fe than found in Refs. [40, 41]. In this specific case, the amount of positive-parity states is very sensitive to the position of the $g_{9/2}$ orbital relative to the Fermi level.

To our understanding, there are currently no experimental data on the parity distribution in ^{56}Fe. However, recent measurements on level densities of $J^\pi = 2^+$ and 2^- states in ^{58}Ni and ^{90}Zr [42] show no indication of a significantly larger amount of states with one of the parities in none of the nuclei under study at $E \approx 10$ MeV. Also, from the study of proton resonances in ^{45}Sc [38], equally many $1/2^+$ and $1/2^-$ states were found, again at $E \approx 10$ MeV. Thus it seems reasonable to assume that the parity asymmetry is at least very small for these excitation energies, in support of the assumption of equal parity as described in Sec. II D.

We would nevertheless like to investigate the impact of the assumption of parity symmetry on the calculations of $\rho(S_n)$. Let us assume that the spin- and parity-projected level density $\rho(E,J,\pi)$ can be described by [41]

$$\rho(E,J,\pi) = \rho(E)\cdot g(E,J)\cdot \mathscr{P}(E,\pi), \tag{31}$$

where $\rho(E)$ is the total level density at excitation energy E, $g(E,J)$ is the spin distribution given by Eq. (27), and $\mathscr{P}(E,\pi)$ is the parity projection factor. According to Eq. (19), we get

$$\frac{1}{D_0} = \rho(S_n)\cdot g(S_n, J = I_t \pm 1/2)\cdot \mathscr{P}(S_n,\pi_t) \tag{32}$$

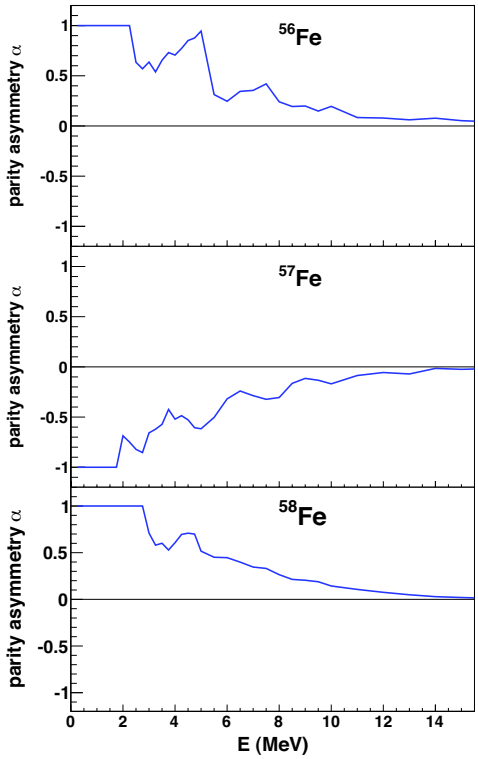

FIG. 23: (Color online). Calculated parity distributions as a function of excitation energy calculated for $^{56-58}$Fe, from Ref. [39].

for the neutron resonance spacing at S_n reaching states with parity $\pi_t \cdot (-1)^\ell = \pi_t$ for s-wave neutrons having $\ell = 0$. Now, we define the parity projection factor for positive and negative parities as

$$\mathscr{P}_+ \equiv \mathscr{P}(E,\pi=\pi_+) = \frac{\rho_+}{\rho} = \frac{1+\alpha}{2}, \tag{33}$$

and

$$\mathscr{P}_- \equiv \mathscr{P}(E,\pi=\pi_-) = \frac{\rho_-}{\rho} = \frac{1-\alpha}{2}, \tag{34}$$

using

$$\mathscr{P}_+ + \mathscr{P}_- = 1. \tag{35}$$

Further,

$$\frac{1}{D_0} = \rho(S_n)\left[g(S_n,J=I_t+1/2)+g(S_n,J=I_t-1/2)\right]\mathscr{P}(S_n,\pi) \tag{36}$$

$$= \rho(S_n)\left[g(S_n,J=I_t+1/2)+g(S_n,J=I_t-1/2)\right]\frac{1\pm\alpha}{2}, \tag{37}$$

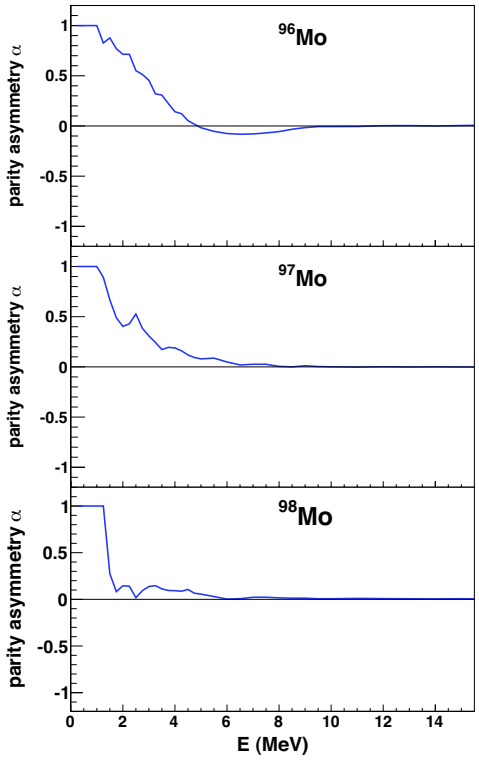

FIG. 24: (Color online). Same as Fig. 23 for $^{96-98}$Mo.

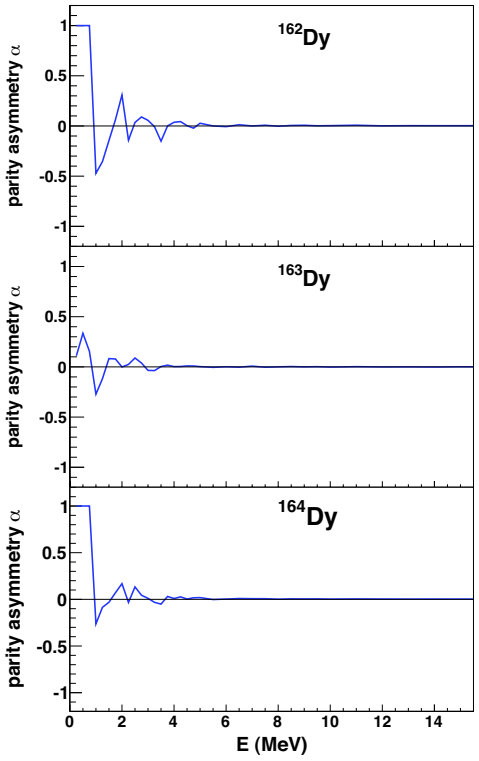

FIG. 25: (Color online). Same as Fig. 23 for $^{162-164}$Dy.

which gives

$$\rho(S_n) = \frac{\sigma^2}{D_0} \frac{(1\pm\alpha)/2}{(I_t+1)\exp\left[-(I_t+1)^2/2\sigma^2\right] + I_t \exp\left[-I_t^2/2\sigma^2\right]}, \quad (38)$$

using Eq. (27). If the target nucleus in the neutron-capture experiment has positive parity in the ground state, the factor $(1+\alpha)/2$ is used, and for negative ground-state parity we use $(1-\alpha)/2$.

For several key cases, we have applied Eq. (38) for calculating $\rho(S_n)$ and compared to the result using Eq. (20). For example, for ^{58}Fe with neutron resonance spacing $D_0 = 6.5$ keV at $S_n = 10.044$ MeV [33], and using the spin cutoff parameter $\sigma(S_n) = 3.93$ from the prescription of Ref. [29], we obtain $\rho(S_n) = 2518$ MeV^{-1} if the assumption of equal parity is used, and $\rho(S_n) = 2939$ MeV^{-1} if we correct for the parity asymmetry $\alpha = 0.14$ predicted by the combinatorial model of [39]. Thus, including the parity asymmetry gives about 17% higher level density at S_n. For ^{96}Mo, with $D_0 = 105$ eV [33], $\sigma(S_n) = 5.15$, and $\alpha = -0.017$ [39], we get $\rho(S_n) = 1.01\cdot 10^5$ MeV^{-1} when no parity asymmetry is taken into account, and $\rho(S_n) = 1.03\cdot 10^5$ MeV^{-1} when the parity asymmetry is considered; only a change of $\approx 2\%$.

To check the effect of the parity asymmetry on the normalization, we have renormalized the data on ^{96}Mo using the above-mentioned values for $\rho(S_n)$ with and without parity correction. Since the estimated α was so small for this case, we have also assumed a much larger parity asymmetry of $\alpha = -0.5$ leading to $\rho(S_n) = 2.02\cdot 10^5$ MeV^{-1}, a factor of 2 larger level density than the one assuming equal parity. Assuming that $\alpha = 0.5$ gives $\rho(S_n) = 6.74\cdot 10^4$ MeV^{-1}, roughly a factor of 2/3 reduction compared to the parity-symmetry case.

The resulting level density and strength function are shown in Figs. 26. Here, it is easily seen that a small parity asymmetry does not give any significant changes of the normalization in neither the level density nor the strength function. However, for $\alpha = -0.5$ corresponding to a factor of 2 larger $\rho(S_n)$ gives an overall larger level density for excitation energies larger than ≈ 3 MeV, and the steeper slope is reflected also in the strength function. In addition, one sees a suppression in the γ-ray strength function for $E_\gamma \lesssim 6$ MeV, a direct consequence of the changes in the level density. The opposite is true for $\alpha = 0.5$; here, $\rho(S_n)$ and thus the slope of the level density is reduced. Consequently, the slope is reduced also in the γ-ray strength function, but the absolute value for

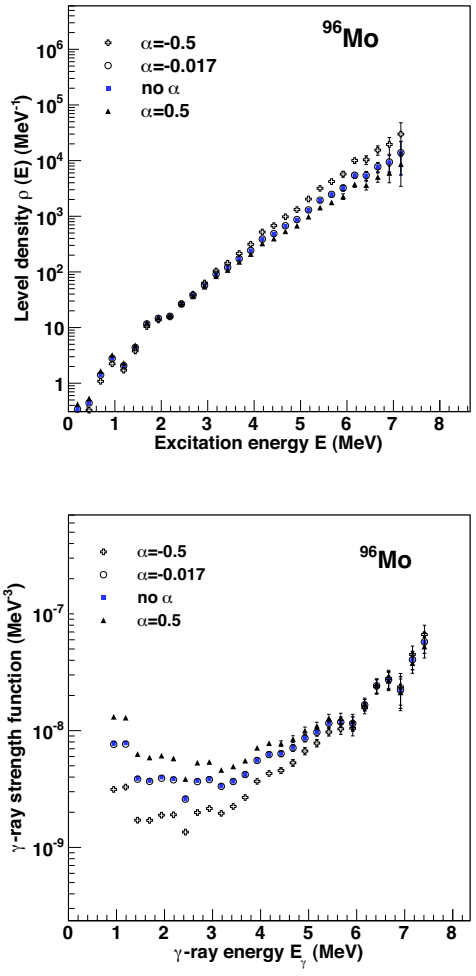

FIG. 26: (Color online). Effect of parity asymmetry on the experimental level density (upper panel) and strength function (lower panel) of ^{96}Mo. The data are taken from the experiment presented in Ref. [12].

$E_\gamma \lesssim 6$ MeV is in this case increased with respect to the parity-symmetry case. Note that such large values of α represent extreme cases; both from experimental data [38, 42] and several theoretical estimates (e.g, [11, 39]) the asymmetry around S_n should be smaller than typically ± 0.2.

The assumption of parity symmetry influences also the normalization of the γ-ray transmission coefficient. To take into account the parity distribution, one can modify Eq. (25) according to Eq. (31) so that

$$\rho(E-E_\gamma, J_f, \pi_f) = \rho(E-E_\gamma)\cdot \mathscr{P}(E-E_\gamma,\pi_f)\cdot g(E-E_\gamma, J_f). \quad (39)$$

We will restrict ourselves to consider $\ell = 1$ radiation only ($E1$ and $M1$), since in general, this multipolarity is expected to give by far the largest contribution to the strength function in the quasicontinuum region (see, e.g., studies by Kopecky and Uhl [32]).

For $E1$ radiation, the parity of the final state is opposite to the initial state. In s-wave neutron capture experiments, the parity of the target nucleus' ground state is equal to the parity of the neutron resonances of the created compound nucleus. Therefore, the accessible parity of the final states must be the opposite of the initial state. For $M1$ radiation, the accessible final states must have the same parity as the initial state.

Based on Eq. (21) and taking the parity distribution into account, one finds

$$\begin{aligned}\langle \Gamma_\gamma(S_n, I_t \pm 1/2, \pi_t)\rangle = & \frac{B}{2\pi\rho(S_n, I_t \pm 1/2, \pi_t)} \\ & \times \int_{E_\gamma=0}^{S_n} dE_\gamma \left[\mathscr{T}_{E1}(E_\gamma)\mathscr{P}_{-/+} + \mathscr{T}_{M1}(E_\gamma)\mathscr{P}_{+/-}\right] \\ & \times \rho(S_n - E_\gamma) \sum_{J=-1}^{1} g(S_n - E_\gamma, I_t \pm 1/2 + J). \quad (40)\end{aligned}$$

for target nuclei with positive/negative ground-state parity. It is easily seen that if $\mathscr{P}_+ = \mathscr{P}_- = 1/2$, Eq. (26) is restored.

The Oslo method does not enable the separation of $\mathscr{T}(E_\gamma)$ into its $E1$ and $M1$ components. We have therefore applied models for the level density and the $E1$ and $M1$ strength functions in order to investigate the influence of including parity on the integral in Eq. (40). For the level density, we have used the results of [39]. For the $E1$ strength function, we have used the the Kadmenskiĭ, Markushev and Furman (KMF) model [43] with a constant temperature $T_f = 0.3$ MeV, while for the $M1$ component (the spin-flip resonance [22]) we have applied a Lorentzian shape (see Ref. [33]). We use again ^{96}Mo as a test case, with experimental GDR parameters taken from Ref. [33] and $M1$ Lorentzian parameters from systematics [33]. The target nucleus ^{95}Mo in the $(n,\gamma)^{96}$Mo reaction has spin/parity $5/2^+$.

First, we take the parity distribution from Ref. [39] as shown in Fig. 24 and apply in the integral of Eq. (40). The resulting value is only about 1% smaller than the value obtained assuming $\mathscr{P}_+ = \mathscr{P}_- = 1/2$ for all excitation energies, implying that the effect of parity is negligible in this case. As a further test we used the parity distribution of ^{56}Fe shown in Fig. 23 on ^{96}Mo; then, we found a $\approx 47\%$ reduction using Eq. (40) compared to the parity-symmetry case. For the very extreme cases assuming that $\alpha = 1$ for all E (allowing only for positive-parity states and $M1$ transitions), we get about a factor of 3 reduction, and using $\alpha = -1$ for all E (allowing only for negative-parity states and $E1$ transitions), we obtain about 67% increase of the normalization integral in Eq. (40) relative to the case where no parity distribution is considered.

To summarize, for nuclei in the Mo mass region and above, we find only small corrections of the order of a few percent

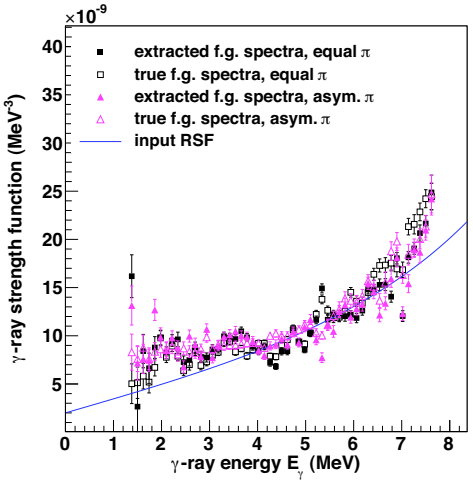

FIG. 27: (Color online). Extracted strength functions from simulated data for an artificial ^{57} Fe nucleus, with and without parity asymmetry in the level density.

to the estimation of $\rho(S_n)$ and also for the absolute normalization of the strength function when using realistic parity distributions (compared to the extreme cases). However, for light nuclei such as Fe, effects of the parity distribution could be significant on both the level-density and strength-function normalization, of the order of 30–50%.

The parity distribution could also potentially influence the γ-ray strength function in other ways than just the normalization. In the quasi-continuum region, one expects that $E1$ transitions largely dominate as long as the parity asymmetry is close to zero. However, if the parity asymmetry is large, $M1$ transitions will be favored over those of $E1$ type. We have investigated this using DICEBOX [34] to generate simulated data on an artificial nucleus resembling ^{57}Fe, as already described in Sec. III B. We have applied a symmetric parity distribution in the first case, and an asymmetric parity distribution in the second case. Note that the parity distribution is implemented directly in the level density only; the input γ-ray strength function is kept fixed.

The resulting γ-ray strength functions are shown in Fig. 27. Visually, it is hard to see any difference between the γ-ray strength functions with and without parity asymmetry. By taking the average γ-ray strength function for γ energies between $1.4-3$ MeV, we find an average increase of about 20% for the case with parity asymmetry relative to the equal parity case, using the true first-generation spectra. The statistical fluctuations here are typically less than 10% for $E_\gamma = 2-3$ MeV, and up to 40% for γ rays below 2 MeV. If we use the extracted first-generation spectra from the folded data, the difference between the two cases is approximately 6–7%, less than the statistical fluctuations which are larger than when using the true first-generation spectra. For higher E_γ, there is no effect of parity within the fluctuations. We therefore conclude that it could be an effect of $\approx 20\%$ on the low-energy part of the γ-ray strength function. Hence, we find it reasonable to believe that even a considerable parity asymmetry on the level density as in the ^{57}Fe case will not drastically change the shape of the γ-ray strength function.

In Fig. 27, we note that there is an enhanced strength for γ-ray energies below ≈ 3.5 MeV compared to the input γ-ray strength function, regardless of the parity distribution. This is in fact due to the spin range of the initial levels, which is further investigated in the following section.

E. The spin distribution

The uncertainty in the spin distribution may lead to errors in the Oslo method in three ways: (*i*) the extraction of first-generation γ rays and subsequent effects on the extracted level density and γ-ray strength function, (*ii*) the estimation of $\rho(S_n)$, and (*iii*) the spin range accessed experimentally (typically $0-8\hbar$ depending on the reaction and target spin) compared to the true, total spin distribution. These issues will be discussed in the following.

We have once more relied on simulated data applying the DICEBOX code [34] in order to test the sensitivity on the final results with respect to the spin range of the initial levels. We simulated again a light nucleus that resembles ^{57}Fe, as we expect that light nuclei would be most sensitive to the initial spin population. This is because the higher spin levels are missing at low excitations. Again, the critical energy was set to 2.2 MeV, as there are no available data in the literature about levels with higher spins above this energy. As before, all levels had the same probability of population. The input γ-ray strength function model was independent of excitation energy.

Three spin ranges were used: $1/2 \le J \le 7/2$, $1/2 \le J \le 13/2$, and $7/2 \le J \le 13/2$. This means that the highest possible spin reached at the final excitation energy was $9/2$ or $15/2$ depending on the maximum allowed initial spin. The weighting of the allowed spins followed the spin distribution of the input level density, which in this case was from the microscopic calculations of Ref. [39]. For all initial spin ranges we applied the full Oslo method, and in parallel we extracted the level density and γ-ray strength function from the true first-generation spectra. The resulting level densities and γ-ray strength functions are displayed in Figs. 28 and 29, respectively.

As can be seen from Fig. 29, there is an enhanced strength at low γ energies for the spin windows including the highest spins. Also, by looking at the average multiplicity $\langle M \rangle$ at 7.0 MeV of excitation energy, we get 1.8 for $1/2 \le J \le 7/2$, 2.2 for $1/2 \le J \le 13/2$, and 2.5 for $7/2 \le J \le 13/2$. At $E_\gamma = 2.1$ MeV, we find that the γ-ray strength function is increased with a factor of ≈ 1.7 for the spin range $1/2 \le J \le 13/2$, and a factor of ≈ 2.6 for the spin range $7/2 \le J \le 13/2$ with respect to the input γ-ray strength function. This is not an artifact from the unfolding or first-generation method, as it is also seen in the extracted γ-ray strength functions from the

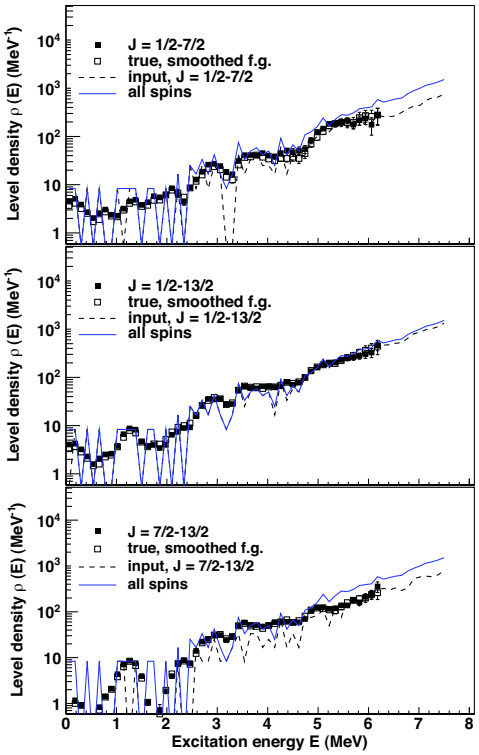

FIG. 28: (Color online). Extracted level densities from simulated data for initial spin range $1/2 \leq J \leq 7/2$ (top panel), $1/2 \leq J \leq 13/2$ (middle panel), and $7/2 \leq J \leq 13/2$ (bottom panel) on the initial levels.

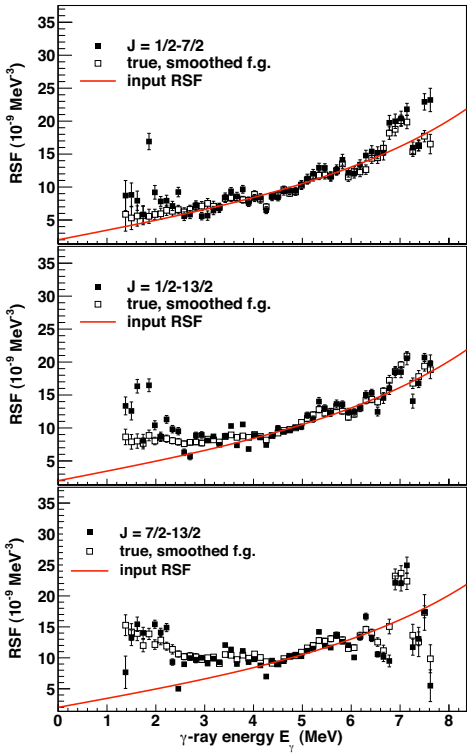

FIG. 29: (Color online). Extracted strength functions for spin range $1/2 \leq J \leq 7/2$ (top), $1/2 \leq J \leq 13/2$ (middle), and $7/2 \leq J \leq 13/2$ (bottom) on the initial levels.

true first-generation spectra.

The explanation for the observed behavior is probably connected to three issues: (*i*) the dominance of dipole radiation, which carries $L = 1$; (*ii*) the applied spin restriction on the initial levels; (*iii*) the low level density in this mass region at low excitation energies, especially for high spins. Let us take, as an example, the population of a 13/2 level at high excitation energy. If it is to decay to a low-lying level, involving a high-energy γ transition, a level with appropriate spin must be present at this excitation energy. This is not necessarily the case as there are only about $2-10$ levels per 120 keV for excitation energies below 4.7 MeV. Among these few levels, there are probably no high-spin levels at all. This leads to a higher average multiplicity and an enhanced probability for decaying with low-energy γ rays.

From Fig. 29, it is clear that the enhancement in the extracted γ-ray strength function is not present in the input γ-ray strength function, but is an effect of the three factors mentioned above. This means that the simple factorization in Eq. (10) of the first-generation spectra is not able to reproduce the input γ-ray strength function. The extracted γ-ray strength function, which could be considered as an "effective" γ-ray strength function, is however fully capable of reproducing the true primary γ-ray spectra, and it is seen from Fig. 28 that the extracted level density is very reasonable indeed.

However, it is not obvious whether the spin range of the inital states is the full explanation of the observed low-energy enhancement in light and medium-mass nuclei. Further investigations are therefore needed to clarify this issue. It should also be noted that similar tests have been performed for an artificial nucleus resembling ^{163}Dy. No such enhancement was seen in this case, in agreement with experimental findings in this mass region. This is not surprising since in these nuclei, the level density is much higher and relatively high spins are available already at low excitation energies.

The quantity $\rho(S_n)$ is calculated assuming a bell-like spin distribution according to Ref. [27] given by Eq. (27) and using a model for the spin cutoff parameter σ usually taken from Ref. [27] or from Ref. [29]. Both these assumptions could in principle be a source of uncertainty, as it is hard or even impossible to measure experimentally the total spin distribution

at high excitation energy. Thus, the theoretical spin distributions are seldom constrained to data for excitation energies higher than typically $2-3$ MeV.

In Fig. 30 various spin distributions for ^{44}Sc are shown, calculated at an excitation energy of 8.0 MeV. In the two upper panels, the spin distribution given in Eq. (27) has been used, but with the expression for the spin cutoff parameter of Refs. [27, 28] in panel a) and the formalism of Ref. [29] in panel b). In panel c) the spin distribution of the spin-dependent level densities of Ref. [44] are shown. Here, the authors also have assumed a bell-shaped spin distribution according to Eqs. (7) and (8) in Ref. [44]. It is clear from the figure that the spin distributions in panel b) and c) are broader with centroids shifted to higher spins compared to the one in panel a).

In panel d), the spin distribution of the calculated spin- and parity-dependent level density of Ref. [45] is shown. There are no underlying assumptions for the spin distribution in these calculations. It is seen from this distribution that there is a significant difference in the relative numbers of states with spin 0 and 1. The normalization procedure for the level density described above is especially sensitive to such variations at low spin if the neutron resonance spacing D_0 is measured from a neutron capture reaction where the target nucleus is even-even, that is, with zero ground-state spin. Then the states reached in neutron capture can only have spin $1/2^+$, and the number of all other states must be estimated using a certain spin cutoff parameter, introducing a larger uncertainty in the calculated $\rho(S_n)$. Therefore it is preferred to calculate $\rho(S_n)$ from both D_0 and D_1 resonance spacings if possible, since in the latter, also states with $3/2^-$ are reached for target nuclei with $I_t^\pi = 0^+$, and will therefore decrease this uncertainty.

We have investigated the relative difference in the value of $\rho(S_n)$ for several nuclei using the spin-cutoff parameter of [27] with global parameterization of [28] (referred to as Gilbert & Cameron), and the prescription of [29] (hereafter called von Egidy & Bucurescu), see Tab. I. For the cases investigated here, the general trend is that the Gilbert & Cameron approach leads to a lower value for $\rho(S_n)$ than the von Egidy & Bucurescu parameterization. However, this depends on the spins reached in the (n,γ) reaction. For example, for ^{51}V, we note that the obtained $\rho(S_n)$ using the spin cutoff of von Egidy & Bucurescu is lower than that of Gilbert & Cameron. This is easily understood from the fact that in this case, relatively high spins are populated in the (n,γ) reaction. We see from Fig. 31 that the Gilbert & Cameron parameterization gives lower relative values for states with spin 11/2 and 13/2 compared to the von Egidy & Bucurescu distribution. Thus, one divides by a smaller number in Eq. (20) and $\rho(S_n)$ gets larger.

One can conclude that the two approaches studied here give a $\approx 10-50\%$ change in the resulting $\rho(S_n)$, while other calculations [39] indicate even larger variations. Using this HFB-plus-combinatorial approach gives typically a factor of two change compared to $\rho_{GC}(S_n)$ for most cases and up to a factor of 3.7 for the extreme case of ^{172}Dy (see Tab. II in Ref. [39]).

Recently, a new expression for the spin-cutoff formula was proposed by von Egidy and Bucurescu [46]. In this work, the spin-cutoff parameter depends directly on the excitation

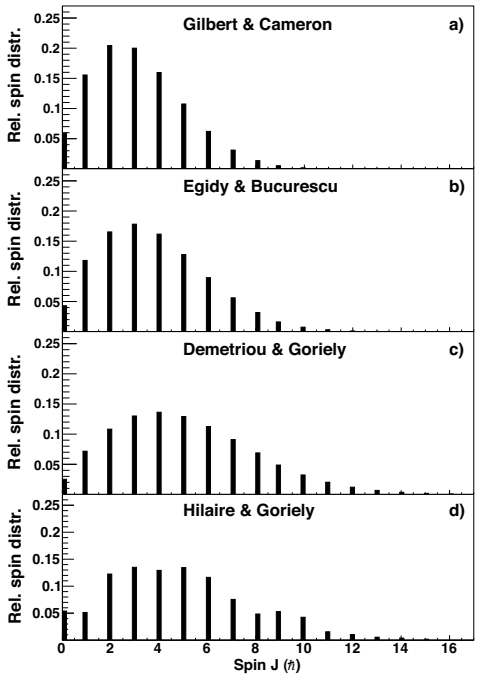

FIG. 30: Relative spin distributions calculated for $E = 8.0$ MeV of ^{44}Sc (see text).

energy and the deuteron pairing (see Eq. (16) in Ref. [46]). Using this expression for the light nuclei listed in Tab. I, we get rather similar values for σ as for the Gilbert & Cameron case. For the heavier ^{117}Sn and ^{164}Dy, the values are lower than using the Gilbert & Cameron approach, and consequently a lower value of $\rho(S_n)$ is obtained.

The effect of all these deviations is of course an uncertain determination of $\rho(S_n)$ and thus of the slope of the level density and the γ-ray strength function, in a similar fashion as for the parity dependence (see Sec. III D and Fig. 26).

There is also a question of how the spin range accessed experimentally relative to the true, total spin range might influence structures in the level density. In the analysis, we assume that the excluded spins contribute on average with a scaling factor of the level density, which is corrected for by normalizing to $\rho(S_n)$, i.e. the total level density for all spins at this energy. However, this relies on the hypothesis that structures in the level density due to, e.g., nucleon pair breaking are not severely affected by the spin window.

To test this, we have performed simplistic calculations with the code COMBI [47], which is based on a microscopic, combinatorial model using Nilsson single-particle energies and the concept of quasiparticles from the nuclear Bardeen-Cooper-Schrieffer (BCS) theory. The chosen spin windows were $0 \le J \le 6$ and $0 \le J \le 30$ (in units of $\hbar$). Details of the model can be found in Ref. [47].

TABLE I: Variation of the calculated $\rho(S_n)$ using different spin cutoff parameters. The target spin in the (n,γ) reaction is denoted by I_t^π, and E_1 is the total backshift for the back-shifted Fermi-gas model while a is the level-density parameter. All level spacings (D_0) are taken from [33]. The parameter η is the ratio $\rho_{EB}(S_n)/\rho_{GC}(S_n)$.

				Gilbert & Cameron				von Egidy & Bucurescu				
Nucleus	I_t^π	S_n	D_0	a	E_1	σ	$\rho_{GC}(Sn)$	a	E_1	σ	$\rho_{EB}(Sn)$	η
		(MeV)	(keV)	(MeV^{-1})	(MeV)		(MeV^{-1})	(MeV^{-1})	(MeV)		(MeV^{-1})	
^{51}V	6^+	11.05	2.3(6)	6.42	-0.511	3.24	5.18×10^3	6.17	-0.153	3.83	4.15×10^3	0.80
^{57}Fe	0^+	7.646	25.4(22)	7.08	-0.910	3.20	8.46×10^2	6.58	-0.523	3.83	1.20×10^3	1.41
^{96}Mo	$5/2^+$	9.154	0.105(10)	11.14	1.016	4.21	7.38×10^4	11.39	0.779	5.15	1.01×10^5	1.37
^{117}Sn	0^+	6.944	0.380(130)	13.23	0.197	4.48	1.08×10^5	13.62	-0.210	5.58	1.67×10^5	1.54
^{164}Dy	$5/2^+$	7.658	0.0068(6)	17.75	0.416	5.49	1.74×10^6	18.12	0.310	6.91	2.59×10^6	1.49

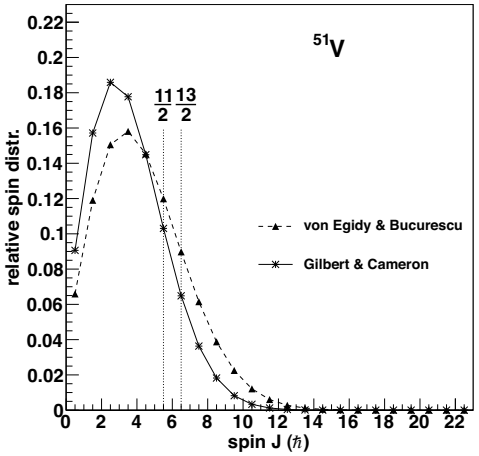

FIG. 31: Relative spin distributions calculated at $S_n = 11.051$ MeV of ^{51}V (see text).

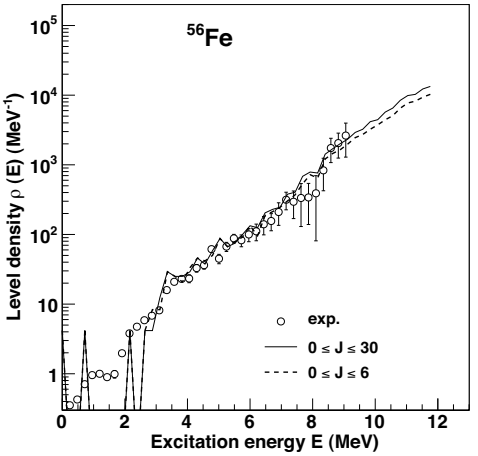

FIG. 32: Calculated level density of ^{56}Fe for two spin ranges: $0 \le J \le 6$ (dashed line) and $0 \le J \le 30$ (solid line) compared to experimental data (open circles, from Ref. [11]) normalized to the total level density at S_n.

The resulting calculated level densities for ^{56}Fe and ^{164}Dy are displayed in Figs. 32 and 33, respectively. For ^{56}Fe, is it clear that most of the states are found within the spin range of $0-6\hbar$. In fact, the relative difference between the large and the small spin window is at most $\approx 30\%$, and it is clear that there are no significant structural differences for the two cases. One would therefore not expect any severe problems with normalizing the level density of such light nuclei to the total level density $\rho(S_n)$. However, for the ^{164}Dy case, the deviation of the level densities calculated within the two spin ranges can be considerable and is increasing with excitation energy, up to a factor of ≈ 2.5 for $E \approx 7.5$ MeV. It is nevertheless very gratifying that, indeed, the gross structures of the level densities are very much alike, so that extracted information from the experimental level density, such as the onset of the pair-breaking process, is probably reliable (the larger spin window leads to a smoothing of the steps). However, experimental work to investigate the spin distribution further is highly desirable.

IV. SUMMARY AND CONCLUSIONS

In this work we have addressed uncertainties and possible systematic errors that one can encounter using the Oslo method. The main steps of the method have been outlined, and the assumptions behind each step are investigated in detail. Our findings indicate that although the Oslo method is in general very robust, the various assumptions it relies on must be carefully considered when it is applied in different mass regions. The results can be summarized as follows.

The unfolding procedure. We have investigated the effect of changing the total absorption efficiencies of the NaI(Tl) crystals up to $\approx 20\%$. We found that the extracted level density is

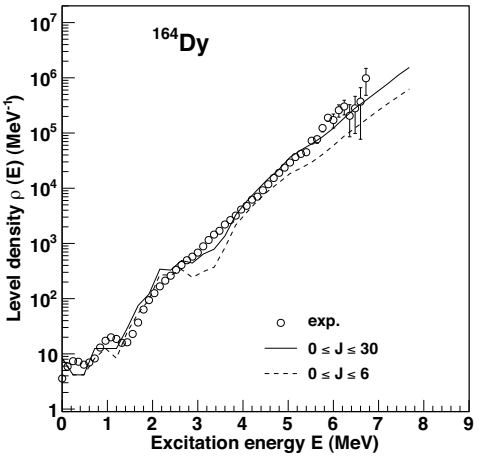

FIG. 33: Same as Fig. 32 for ^{164}Dy, with experimental data from Ref. [5].

hardly affected at all, while the γ-ray strength function gets a somewhat different slope. The quantitative effect on the γ-ray strength function corresponds directly to the imposed changes in the efficiencies.

The first-generation method. In general, the assumption of thermalization can be questioned at excitation energies above ≈ 10 MeV. Also, variation in the populated spin range as a function of excitation energy may lead to an erroneous subtraction, especially of yrast states and other strong transitions at low γ-ray energies. This is particularly pronounced at low excitation and low γ-ray energies, where the direct reaction may favor or suppress the population of some levels compared to feeding from γ decay. In addition, the finite, and for some energies, the mismatch of the detector resolution of the particle telescopes and CACTUS might in principle lead to problems with determining correct weighting functions. However, tests on simulated spectra show that this effect is probably of minor importance. The two different normalization options in the method turn out to give very similar results.

The Brink hypothesis. Since the extraction of level density and γ-ray strength relies on the Brink hypothesis, one would expect problems if there was an effective temperature dependence in the γ-ray strength function. From the results of simulated data, it is clear that especially the region of low E_γ is affected when the γ-ray strength function is temperature dependent, and the extracted strength is found to found to lie in between the two temperature extremes considered. However, we note that there is, so far, no experimental evidence for any strong temperature dependence of the γ-ray strength function in the excitation-energy region in question (below ≈ 10 MeV).

The parity distribution. The assumption of equally many positive- and negative-parity states may break down, especially for light nuclei, and would then affect the normalization of both the level density and the γ-ray strength function. If the parity asymmetry is large, the value of the normalization point $\rho(S_n)$ might change with a factor of ≈ 2, which will consequently change the slope of the level density and γ-ray strength function. For heavier nuclei, however, the parity distribution at S_n is expected to be quite even, and experimental data on lighter nuclei suggest that the parity asymmetry should be small also here. Therefore, we find it reasonable to believe that the error in $\rho(S_n)$ and on the absolute normalization of the γ-ray strength function due to this assumption does not exceed 50%.

Another issue is the influence on the relative contribution of $E1$ and $M1$ transitions, as a large parity asymmetry will favor $M1$ transitions. Tests with simulated data indicate, however, that the effect is not large even with a considerable parity asymmetry.

The spin distribution. From simulations on light nuclei with different spin ranges on the initial levels, it is seen that the ranges including higher spins might lead to an enhanced γ-ray strength function at low γ-ray energies. This is understood from considering the relatively low level density and the matching of spins between the initial and final levels for dipole radiation. This could explain, at least partially, the observed enhanced low-energy strength in experimental data for light and medium-mass nuclei.

The spin distribution is one of the largest uncertainties in the normalization, since the determination of the slope of the level density and γ-ray strength function strongly depends on the relative intensities of the populated spins at S_n. Assuming a bell-shaped spin distribution with various global parameterizations of the spin cutoff parameter give up to $\approx 50\%$ change in $\rho(S_n)$; however, microscopic calculations indicate that this value can vary within a factor of 2 or more, especially for nuclei in the rare-earth region. This will also consequently influence the γ-ray strength function.

The experimentally reached spin window in OCL experiments is typically $0-8\hbar$, which means that the extracted level-density data in fact represent this narrow spin range. This is usually compensated for by normalizing to the total level density at S_n. This is not a big effect for light nuclei with relatively few high-spin states. Even in the case of rare-earth nuclei, our calculations indicate that this scaling works well as the main structures in the level density are indeed present in the levels of a rather narrow spin range.

V. ACKNOWLEDGMENTS

The authors wish to thank E. A. Olsen and J. Wikne for providing excellent experimental conditions. Financial support from the Research Council of Norway (NFR), project no. 180663, is gratefully acknowledged.

[1] J. Rekstad *et. al.*, Physica Scripta Vol. T5, 45 (1983).
[2] A. Schiller, A. Voinov, E. Algin, J. A. Becker, L. A. Bernstein, P. E. Garrett, M. Guttormsen, R. O. Nelson, J. Rekstad, and S. Siem, Phys. Lett. B **633** 225 (2006).
[3] U. Agvaanluvsan, A. Schiller, J. A. Becker, L. A. Bernstein, P. E. Garrett, M. Guttormsen, G. E. Mitchell, J. Rekstad, S. Siem, A. Voinov, and W. Younes, Phys. Rev. C **70**, 054611 (2004).
[4] M. Guttormsen, A. Bagheri, R. Chankova, J. Rekstad, A. Schiller, S. Siem, and A. Voinov, Phys. Rev. C **68**, 064306 (2003).
[5] H. T. Nyhus, S. Siem, M. Guttormsen, A. C. Larsen, A. Bürger, N. U. H. Syed, G. M. Tveten, and A. Voinov, Phys. Rev. C **81**, 024325 (2010).
[6] E. Melby, L. Bergholt, M. Guttormsen, M. Hjorth-Jensen, F. Ingebretsen, S. Messelt, J. Rekstad, A. Schiller, S. Siem, and S. W. Ødegård, Phys. Rev. Lett. **83**, 3150 (1999).
[7] U. Agvaanluvsan, A. C. Larsen, M. Guttormsen, R. Chankova, G. E. Mitchell, A. Schiller, S. Siem, and A. Voinov, Phys. Rev. C **79**, 014320 (2009).
[8] U. Agvaanluvsan, A. C. Larsen, R. Chankova, M. Guttormsen, G. E. Mitchell, A. Schiller, S. Siem, and A. Voinov, Phys. Rev. Lett. **102**, 162504 (2009).
[9] H. K. Toft, A. C. Larsen, U. Agvaanluvsan, A. Bürger, M. Guttormsen, G. E. Mitchell, H. T. Nyhus, A. Schiller, S. Siem, N. U. H. Syed, and A. Voinov, Phys. Rev. C **81**, 064311 (2010).
[10] A. Voinov, E. Algin, U. Agvaanluvsan, T. Belgya, R. Chankova, M. Guttormsen, G.E. Mitchell, J. Rekstad, A. Schiller, and S. Siem, Phys. Rev. Lett **93**, 142504 (2004).
[11] E. Algin, U. Agvaanluvsan, M. Guttormsen, A. C. Larsen, G. E. Mitchell, J. Rekstad, A. Schiller, S. Siem, and A. Voinov, Phys. Rev. C **78**, 054321 (2008).
[12] M. Guttormsen, R. Chankova, U. Agvaanluvsan, E. Algin, L.A. Bernstein, F. Ingebretsen, T. Lönnroth, S. Messelt, G.E. Mitchell, J. Rekstad, A. Schiller, S. Siem, A. C. Sunde, A. Voinov and S. Ødegård, Phys. Rev. C **71**, 044307 (2005).
[13] A. C. Larsen, R. Chankova, M. Guttormsen, F. Ingebretsen, T. Lönnroth, S. Messelt, J. Rekstad, A. Schiller, S. Siem, N. U. H. Syed, A. Voinov, and S. W. Ødegård, Phys. Rev. C **73**, 064301 (2006).
[14] A. C. Larsen, M. Guttormsen, R. Chankova, F. Ingebretsen, T. Lönnroth, S. Messelt, J. Rekstad, A. Schiller, S. Siem, N. U. H. Syed, and A. Voinov, Phys. Rev. C **76**, 044303 (2007).
[15] M. Guttormsen, A. C. Larsen, A. Bürger, A. Görgen, S. Harissopulos, M. Kmiecik, T. Konstantinopoulos, M. Krtička, A. Lagoyannis, T. Lönnroth, K. Mazurek, M. Norrby, H. T. Nyhus, G. Perdikakis, A. Schiller, S. Siem, A. Spyrou, N. U. H. Syed, H. K. Toft, G. M. Tveten, and A. Voinov, Phys. Rev. C **83**, 014312 (2011).
[16] A. C. Larsen and S. Goriely, Phys. Rev. C **82**, 014318 (2010).
[17] M. Guttormsen, A. Ataç, G. Løvhøiden, S. Messelt, T. Ramsøy, J. Rekstad, T.F. Thorsteinsen, T.S. Tveter, and Z. Zelazny, Phys. Scr. **T 32**, 54 (1990).
[18] M. Guttormsen, T. S. Tveter, L. Bergholt, F. Ingebretsen, and J. Rekstad, Nucl. Instrum. Methods Phys. Res. A **374**, 371 (1996).
[19] M. Guttormsen, T. Ramsøy, and J. Rekstad, Nucl. Instrum. Methods Phys. Res. A **255**, 518 (1987).
[20] G. A. Bartholomew, I. Bergqvist, E. D. Earle, and A. J. Ferguson, Can. J. Phys. **48**, 687 (1970).
[21] J. Rekstad, A. Henriquez, F. Ingebretsen, G. Midttun, B. Skaali, R. Øyan, J. Wikne, and T. Engeland, Phys. Scr. **T 5**, 45 (1983).
[22] A. Bohr and B. Mottelson, *Nuclear Structure*, Benjamin, New York, 1969, Vol. I.
[23] L. Henden, L. Bergholt, M. Guttormsen, J. Rekstad, and T. S. Tveter, Nucl. Phys. **A589**, 249 (1995).
[24] D. M. Brink, Ph.D. thesis, p.101-110, Oxford University, 1955.
[25] A. Schiller, L. Bergholt, M. Guttormsen, E. Melby, J. Rekstad, and S. Siem, Nucl. Instrum. Methods Phys. Res. A **447**, 498 (2000).
[26] C. E. Porter and R. G. Thomas, Phys. Rev. **104**, 483 (1956).
[27] A. Gilbert and A. G. W. Cameron, Can. J. Phys. **43**, 1446 (1965).
[28] T. von Egidy, H. H. Schmidt and A. N. Behkami, Nucl. Phys. **A 481** (1988) 189.
[29] T. von Egidy and D. Bucurescu, Phys. Rev. C **72**, 044311 (2005); Phys. Rev. C **73**, 049901(E) (2006).
[30] N. U. H. Syed, M. Guttormsen, F. Ingebretsen, A. C. Larsen, T. Lönnroth, J. Rekstad, A. Schiller, S. Siem, and A. Voinov, Phys. Rev. C **79**, 024316 (2009).
[31] A. Voinov, M. Guttormsen, E. Melby, J. Rekstad, A. Schiller, and S. Siem, Phys. Rev. C **63**, 044313 (2001).
[32] J. Kopecky and M. Uhl, Phys. Rev. C**41**, 1941 (1990).
[33] T. Belgya, O. Bersillon, R. Capote, T. Fukahori, G. Zhigang, S. Goriely, M. Herman, A. V. Ignatyuk, S. Kailas, A. Koning, P. Oblozinsky, V. Plujko and P. Young, *Handbook for calculations of nuclear reaction data*, RIPL-2. **IAEA-TECDOC-1506** (IAEA, Vienna, 2006).
[34] F. Bečvář, Nucl. Instrum. Methods Phys. Res. A **417**, 434 (1998).
[35] E. Běták, in *Proceedings of the Second International Workshop on Compond Nuclear Reactions and Related Topics, 5−8 October 2009, Bordeaux, France*, EPJ Web of Conferences **2**, 11002 (2010).
[36] J. W. Smith, L. Meyer-Schützmeister, T. H. Braid, P. P. Singh, and G. Hardie, Phys. Rev. C **7**, 1099 (1973).
[37] A. Schiller and M. Thoennessen, At. Data Nucl. Data Tables 93, 549 (2007).
[38] U. Agvaanluvsan, G. E. Mitchell, J. F. Shriner Jr., and M. Pato, Phys. Rev. C **67**, 064608 (2003).
[39] S. Goriely, S. Hilaire, and A. J. Koning, Phys. Rev. C **78**, 064307 (2008).
[40] Y. Alhassid, G. F. Bertsch, S. Liu, and H. Nakada, Phys. Rev. Lett **84**, 4313 (2000).
[41] D. Mocelj, T. Rauscher, G. Martínez-Pinedo, K. Langanke, L. Pacearescu, A. Faessler, F.-K. Thielemann, and Y. Alhassid, Phys. Rev. C **75**, 045805 (2007).
[42] Y. Kalmykov, C. Özen, K. Langanke, G. Martínez-Pinedo, P. von Neumann-Cosel, and A. Richter, Phys. Rev. Lett **99**, 202502 (2007).

[43] S. G. Kadmenskiĭ, V. P. Markushev, and V. I. Furman, Sov. J. Nucl. Phys. **37**, 165 (1983).
[44] P. Demetriou and S. Goriely, Nucl. Phys. **A 695**, 95 (2001).
[45] S. Hilaire and S. Goriely, Nucl. Phys. **A 779**, 63 (2006).
[46] T. von Egidy and D. Bucurescu, Phys. Rev. C **80**, 054310 (2009).
[47] N. U. H. Syed, A. C. Larsen, A. Bürger, M. Guttormsen, S. Harissopulos, M. Kmiecik, T. Konstantinopoulos, M. Krtička, A. Lagoyannis, T. Lönnroth, K. Mazurek, M. Norby, H. T. Nyhus, G. Perdikakis, S. Siem, and A. Spyrou, Phys. Rev. C **80**, 044309 (2009).

Chapter 8

Summary and conclusions

8.1 Experimental results on Sn

In this thesis, the level densities of ^{118,119,121,122}Sn and the γ-ray strength functions of ^{116,118,119,121,122}Sn below the neutron separation energy have been studied. The approach has been to apply the Oslo method on data from the (^{3}He,$\alpha\gamma$) and (^{3}He,^{3}He$'\gamma$) reactions. The results have been compared to previous OCL studies of ^{116,117}Sn [6, 7]. The studies have been published in Articles 1 and 2.

In our experiments on the Sn isotopes, a region of unknown level density from the discrete region up to $1-2$ MeV below the neutron separation energy S_n has been studied (Articles 1 and 2). The level densities of ^{119,121,122}Sn display distinctive step-like structures for excitation energies below $E \approx 4$ MeV (Articles 1 and 2). This was also the case in ^{116,117}Sn [7]. The steps in the level densities of Sn isotopes are the most distinctive steps measured so far at the OCL. This is probably due to the closed proton shell of Sn ($Z = 50$), increasing the energy required to break a proton pair. Hence for the lower excitation energies, only neutron pairs are broken, without any interference on the level density from broken proton pairs. The bump centered around the neutron pairing energy, which is $2\Delta_n \approx 2.5$ MeV, is thus interpreted as a signature of neutron pair breaking in the Sn isotopes (Article 1).

A combinatorial BCS model has been used to extract nuclear properties from a prediction of the level densities of ^{118,119}Sn (Article 1). The model is simple and also relies on the given input values. However, since the experimental level densities in these isotopes are reproduced rather well by the model, we may expect that its predictions are representative. In particular, the log-scale slope of the predicted level densities agrees well with the measured ones. In the model, this slope depends on, e.g., the input values of the neutron and proton pair-gap parameters, and thus, support is given to the values we applied. Some of the most

interesting results from the simulations concern the bump in the measurements that we interpreted as a signature of neutron pair breaking: The predicted average number of neutron pair breakings per excitation energy bin has in fact at the energy $E \approx 2.5$ MeV a very abrupt increase from 0 to 1, while pair-breaking of protons almost do not occur below ≈ 4 MeV. Hence, the model shows that the pair breakings here are basically only due to neutrons. Provided that our applied values of the pair-gap parameters are reasonable, so that this abrupt increase in the model corresponds to the distinctive step in the measured level density, this step in the level density is probably due to pure neutron pair breaking.

The rare-earth midshell nuclei have a constant single neutron entropy of $\overline{\Delta S} \approx 1.7\ k_B$ for a wide range of excitation energies [48]. In other words, there is a simple scaling with the number of nucleons not coupled in Cooper pairs. We have deduced the single neutron entropy of ^{119}Sn from the experimental level densities of ^{118,119}Sn and determined it to be a constant, $\Delta S = 1.7 \pm 0.2\ k_B$, for excitation energies above ≈ 3 MeV (Article 1). Within the uncertainty, this is in agreement with the finding in ^{117}Sn [7]. For lower excitation energies than $E \approx 3$ MeV, the single neutron entropies of ^{117,119}Sn are clearly not constant. We conclude that Sn isotopes, having a filled proton shell, have a more complicated entropy difference than the rare-earth midshell nuclei.

The γ-ray strength functions of ^{116,118,119,121,122}Sn were compared to standard strength models and (γ,n) and (γ,x) measurements [34, 49, 50, 51, 52]. Significant enhancements in integrated strength in these isotopes were found for γ-ray energies above $E_\gamma \approx 4-5$ MeV (Articles 1 and 2), which was also the case for ^{117}Sn [6]. This observed enhancement in Sn is interpreted as due to the pygmy resonance. In the absence of any established theoretical model, we have modeled the resonance with a Gaussian distribution. A better prediction may be found in the future.

Neutron-capture cross sections for $^{117-119,121}$Sn have been calculated from our strength predictions using the reaction code TALYS [53] (Article 2). Experimental neutron-capture cross sections are well reproduced. Our predictions give significantly better agreement with experiments than standard strength models without the pygmy resonance.

Studying the neutron dependency of the pygmy resonance is important and may help in determining its origin. We have found that we cannot see any dependence within the uncertainties on isotope in the resonances' integrated strength, and that their centroid energies are shifted towards increasing γ-ray energies with increasing neutron number N of the isotope (Article 2). The significant increase of the centroid energies are also clear from studying the γ-ray energies for which there is a change of log-scale slope in the strength function. The change of slope is interpreted as the onset of the pygmy resonance.

Our estimates of the centroid energies of the pygmy resonances increase

smoothly from $E_{\mathrm{pyg}} \approx 8.0(1)$ MeV in ^{116,117}Sn to 8.6(2) MeV in ^{122}Sn (Article 2). However, the finding of an increase of centroid energy with increasing neutron number is in contradiction to existing theoretical calculations, which often predict a decrease instead.

The $E1$ neutron-skin oscillation mode is assumed to be the underlying physical phenomenon in most theoretical studies of the pygmy resonance (Article 2). They often predict a systematic increase in the resonance integrated strength as the number of neutrons increase, due to the increase of the neutron skin. The predicted increase of the integrated resonance strength from ^{116}Sn to ^{122}Sn is often significant and is thus expected to be detectable in measurements (see e.g., Refs. [25, 30, 31]), though one study [29] predicts that the integrated strength is relatively stable in the mass region $A = 120 - 126$.

We cannot see any dependency on neutron number in the resonance strength measured in these OCL experiments. For all the isotopes, the integrated strengths have been estimated to $\approx 1.7(9)\%$ or $\approx 1.8^{+1}_{-5}\%$ of the TRK sum rule. However, the experimental uncertainties are large, and more experimental information is needed to conclude in this important question.

The pygmy resonance may be small compared to the GEDR, but still, the enhancement in strength is significant. The significant magnitude might indicate that the resonance is indeed caused by a collective phenomenon, in contrary to independent single-particle excitations. This additional strength may have important impacts in nuclear astrophysics on the calculated distribution of elemental abundance.

It has been confirmed that also these Sn isotopes do not display any strongly enhanced strength function for low γ-ray energies.

8.2 Systematic uncertainties

This thesis has in Article 3 also investigated the systematic uncertainties in the Oslo method. The conclusion is that the Oslo method is generally very robust, but that some assumptions should be considered when analysing experiments. Here we will give a summary of the most important uncertainties from this article, in addition to a discussion of their impact on the results for Sn.

It is found that often in the first-generation method there will be an erroneous subtraction for the regions of low γ-ray energies. This may be visualised by vertical ridges (strongly populated regions) and/or vallies (empty regions) in the first-generation matrixes (see, e.g., Fig. 4.5). The problem occurs due to different feeding of these discrete states from the reaction and from the decay from higher-lying states (non-independence of method of formation). This different feeding leads to different shapes as a function of excitation energy of the γ-ray

spectra. This shortcoming of the first-generation method is taken into account by eliminating the low γ-ray energy part of the first-generation matrix from the analysis (Article 3).

Another finding of Article 3 is that a relatively small parity asymmetry does not have a significant impact on the normalisation of the level density and the strength function, while a large parity asymmetry, often found for light nuclei, may change the normalisation value $\rho(S_n)$ with a factor of ≈ 2. Tin, being a heavy element, is expected to have less parity asymmetry. In Article 1, we did calculations on the parity asymmetry in two Sn isotopes. The predicted parity asymmetry is smaller than for the medium-heavy nucleus $\left(^{96}\mathrm{Mo}\right)$ investigated in Article 3, for which the influence on the normalisation was found to be negligible. It is thus expected that the impact from parity asymmetry on the normalisation of the Sn isotopes is also negligible.

The probably largest uncertainty in the normalisation of the Sn isotopes stems from the uncertainty in the spin distribution. The calculations in Article 3 indicate that the normalisation value $\rho(S_n)$ may vary with a factor of two or more, depending on the choice of spin distribution. The variation will especially be found for nuclei in the rare-earth region. A variation in $\rho(S_n)$ influences the normalisation of both the level density and the strength function. Experimental work to further investigate the spin distribution is highly desirable.

The experimentally reached spin window at the OCL is typically $0-8\hbar$, while the true spin range for the heavier nuclei may be higher. Therefore, not all of the level density is measured in OCL experiments. Calculations in Article 3 on a rare-earth nucleus show that the main structures are very much alike when different spin windows are compared. This finding is expected to be the case also for Sn. Therefore when normalising the measured level density to the normalisation value $\rho(S_n)$, which has been estimated for all spins, the level density extracted from our experiments is thus expected to be scaled to including all spins.

Article 3 also discusses one possible origin of the low-energy enhancement in the strength function seen in light nuclei in earlier experiments at the OCL. Simulations on these nuclei applying different spin ranges on the initial levels shows that the case with the range including the highest spins may in these nuclei give an enhanced strength function at low γ-ray energies. This is understood from considering the relatively low level density and the matching of spins between the initial and final levels for dipole radiation. The enhancement in strength was not seen in the Sn measurements.

8.3 Conclusions

The present thesis has provided new knowledge of the Sn isotopes and the pygmy resonance. For the first time, the functional form from low energy to the neutron separation energy of the level density and the strength function have been measured in a systematic study of many Sn isotopes. One observed pronounced step in the level densities has been interpreted as due to neutron pair breaking. With increasing neutron number, the pygmy resonance seems to display an increase of centroid energy, while no change in the integrated strength is observed. The estimated centroid energies increase from $E_\gamma \approx 8.0(1)$ MeV in ^{116}Sn to 8.6(2) MeV in ^{122}Sn. The integrated strength of the resonance is determined to $\approx 1.8^{+1}_{-5}\%$ of the classical TRK sum rule. Also systematic uncertainties in the Oslo method have been investigated in this thesis.

8.4 Outlook

Several experimental issues would be desirable to investigate further. The theoretical predictions for the neutron-skin oscillation mode is of $E1$ character. Clarification of the electromagnetic character is of utmost importance and is one of the most interesting question to get an answer to. This knowledge may help in understanding the underlying physics of the pygmy resonance. This is a kind of experiment that cannot be performed at the OCL, since here, the total strength is measured without distinguishing between magnetic and electric radiation.

Tin is a ideal element for a systematic study of the pygmy resonance due to its large number of stable isotopes. The stable isotopes ^{112}Sn and ^{124}Sn may be chosen as targets for future OCL measurements. It will make possible the comparison of the pygmy resonances in ^{111}Sn (pick-up reaction) and ^{125}Sn (stripping reaction), giving an even larger difference in neutron number than studied in the present thesis. The comparison of even a larger isotope difference may provide more information. Support may be given to our finding of an increasing energy centroid with increasing neutron number, and one may actually establish if the integrated strength increases or not.

Also even more neutron-rich Sn isotopes are possible to study. This would be the unstable isotopes. They may be investigated in radioactive beam facilities, like the facilities ISOLDE [54] at CERN or SPIRAL2 [55] at GANIL.

At the moment, analyses on Pd ($Z = 46$) and Cd ($Z = 48$) experiments are ongoing at the OCL. We look forward to seeing if pygmy resonances are displayed for these cases.

For the future, the groups at the OCL hopes to get funding to replace the CACTUS NaI detector system with $LaBr_3$(Ce) scintillation detectors [56]. The

$LaBr_3$ are better than our current system in both energy resolution, γ-ray detection efficiency and timing properties. Such an instrument would significantly improve the γ-ray spectra and give more accurate measurements of the nuclear properties in the quasi-continuum region.

Bibliography

[1] E. Melby, L. Bergholt, M. Guttormsen, M. Hjorth-Jensen, F. Ingebretsen, S. Messelt, J. Rekstad, A. Schiller, S. Siem, and S. W. Ødegård, Phys. Rev. Lett. **83**, 3150 (1999).

[2] A. Voinov, E. Algin, U. Agvaanluvsan, T. Belgya, R. Chankova, M. Guttormsen, G. E. Mitchell, J. Rekstad, A. Schiller, and S. Siem, Phys. Rev. Lett. **93**, 142504 (2004).

[3] M. Guttormsen, R. Chankova, U. Agvaanluvsan, E. Algin, L. A. Bernstein, F. Ingebretsen, T. Lönnroth, S. Messelt, G. E. Mitchell, J. Rekstad, A. Schiller, S. Siem, A. C. Sunde, A. Voinov, and S. Ødegård, Phys. Rev. C **71**, 044307 (2005).

[4] A. Schiller, A. Voinov, E. Algin, J. A. Beccker, L. A. Bernstein, P. E. Garrett, M. Guttormsen, R. O. Nelson, J. Rekstad, and S. Siem, Phys. Lett. B **633**, 225 (2006).

[5] A. Voinov, A. Schiller, M. Guttormsen, J. Rekstad, and S. Siem, Nucl. Instrum. Methods A **497**, 350 (2003).

[6] U. Agvaanluvsan, A. C. Larsen, R. Chankova, M. Guttormsen, G. E. Mitchell, A. Schiller, S. Siem, and A. Voinov, Phys. Rev. Lett. **102**, 162504 (2009).

[7] U. Agvaanluvsan, A. C. Larsen, M. Guttormsen, R. Chankova, G. E. Mitchell, A. Schiller, S. Siem, and A. Voinov, Phys. Rev. C **79**, 014320 (2009).

[8] H. K. Toft, A. C. Larsen, U. Agvaanluvsan, A. Bürger, M. Guttormsen, G. E. Mitchell, H. T. Nyhus, A. Schiller, S. Siem, N. U. H. Syed, and A. Voinov, Phys. Rev. C **81**, 064311 (2010).

[9] H. K. Toft, A. C. Larsen, A. Bürger, M. Guttormsen, A. Görgen, H. T. Nyhus, T. Renstrøm, S. Siem, G. M. Tveten, and A. Voinov, accepted for publication in Phys. Rev. C (2010).

[10] A. C. Larsen, M. Guttormsen, M. Krtička, E. Běták, A. Bürger, A. Görgen, H. T. Nyhus, J. Rekstad, A. Schiller, S. Siem, H. K. Toft, G. M. Tveten, A. V. Voinov, and K. Wikan, accepted for publication in Phys. Rev. C (2010).

[11] M. Guttormsen, T. S. Tveter, L. Bergholt, F. Ingebretsen, and J. Rekstad, Nucl. Instrum. Methods A **374**, 371 (1996).

[12] W. R. Leo, *Techniques for Nuclear and Particle Physics Experiments* (Springer-Verlag, 1994).

[13] M. Guttormsen, T. Ramsøy, and J. Rekstad, Nucl. Instrum. Methods A **255**, 518 (1987).

[14] A. Schiller, L. Bergholt, M. Guttormsen, E. Melby, J. Rekstad, and S. Siem, Nucl. Instrum. Methods A **447**, 498 (2000).

[15] D. M. Brink, Ph.D. thesis, Oxford University (1955).

[16] P. Axel, Phys. Rev. **126**, 671 (1962).

[17] A. Bohr and B. Mottelson, *Nuclear Structure*, Vol. I. (W. A. Benjamin, Inc., 1969).

[18] T. von Egidy, H. H. Schmidt, and A. N. Behkami, Nucl. Phys. A **481**, 189 (1988).

[19] A. Gilbert and A. G. W. Cameron, Can. J. Phys. **43**, 1446 (1965).

[20] A. Voinov, M. Guttormsen, E. Melby, J. Rekstad, A. Schiller, and S. Siem, Phys. Rev. C **63**, 044313 (2001).

[21] J. Kopecky and M. Uhl, Phys. Rev. C **4**, 1941 (1990).

[22] G. A. Bartholomew, E. D. Earle, A. J. Fergusson, J. W. Knowles, and M. A. Lone, Adv. Nucl. Phys. 7, 229 (1972/73).

[23] N. Paar, Rep. Prog. Phys. **70** (2007), p. 691–793.

[24] R. Mohan, M. Danos, and L. C. Biedenharn, Phys. Rev. C **3**, 1740 (1971).

[25] P. Van Isacker, M. A. Nagarajan, and D. D. Warner, Phys. Rev. C **45**, R13 (1992).

[26] N. Paar, P. Ring, T. Nikšić, and D. Vretenar, Phys. Rev. C **67**, 034312 (2003).

[27] D. Vretenar, N. Paar, P. Ring, and G. A. Lalazissis, Nucl. Phys. A **692**, 496 (2001).

[28] J. Endres, E. Litvinova, D. Savran, P. A. Butler, M. N. Harakeh, S. Harissopulos, R.-D. Herzberg, R. Krücken, A. Lagoyannis, N. Pietralla, V. Yu. Ponomarev, L. Popescu, P. Ring, M. Scheck, K. Sonnabend, V. I. Stoica, H. J. Wörtche, and A. Zilges, Phys. Rev. Lett. **105**, 212503 (2010).

[29] I. Daoutidis (private communication).

[30] N. Tsoneva and H. Lenske, Phys. Rev. C **77**, 024321 (2008).

[31] E. Litvinova, P. Ring, and V. Tselyaev, Phys. Rev. Lett. **105**, 022502 (2010).

[32] J. Terasaki and J. Engel, Phys. Rev. C **74**, 044301 (2006).

[33] G. Tertychny, V. Tselyaev, S. Kamerdzhiev, F. Grümmer, S. Krewald, J. Speth, A. Avdeenkov, and E. Litvinova, Phys. Lett. B **647** 104 (2007).

[34] H. Utsunomiya, S. Goriely, M. Kamata, T. Kondo, O. Itoh, H. Akimune, T. Yamagata, H. Toyokawa, Y.-W. Lui, S. Hilaire, and A. J. Koning, Phys. Rev. C **80**, 055806 (2009).

[35] E. J. Winhold, E. M. Bowey, D. B. Gayther, and B. H. Patrick, Physics Letters **32B**, 7 (1970).

[36] P. Adrich, A. Klimkiewicz, M. Fallot, K. Boretzky, T. Aumann, D. Cortina-Gil, U. Datta Pramanik, Th. W. Elze, H. Emling, H. Geissel, M. Hellström, K. L. Jones, J. V. Kratz, R. Kulessa, Y. Leifels, C. Nociforo, R. Palit, H. Simon, G. Surówka, K. Sümmerer, and W. Waluś, Phys. Rev. Lett. **95**, 132501 (2005).

[37] K. Govaert, F. Bauwens, J. Bryssinck, D. De Frenne, E. Jacobs, W. Mondelaers, L. Govor, V. Y. Ponomarev, Phys. Rev. C **57**, 2229 (1998).

[38] S. Goriely and E. Khan, Nucl. Phys. A **706**, 217 (2002).

[39] S. Goriely, E. Khan, and M. Samyn, Nucl. Phys. A **739**, 331 (2004).

[40] A. Tonchev (private communication).

[41] Klimkiewicz, N. Paar, P. Adrich, M. Fallot, K. Boretzky, T. Aumann, D. Cortina-Gil, U. Datta Pramanik, Th. W. Elze, H. Emling, H. Geissel, M. Hellström, K. L. Jones, J. V. Kratz, R. Kulessa, C. Nociforo, R. Palit, H. Simon, G. Surówka, K. Sümmerer, D. Vretenar, and W. Waluś, Phys. Rev. C **76**, 051603(R) (2007).

[42] C. Djalali, N. Marty, M. Morlet, A. Willis, J. C. Jourdain, N. Anantaraman, G. M. Crawley and, A. Galonsky, and P. Kitching, Nucl. Phys. A **388**, 1 (1982).

[43] A. C. Larsen, M. Guttormsen, R. Chankova, F. Ingebretsen, T. Lönnroth, S. Messelt, J. Rekstad, A. Schiller, S. Siem, N. U. H. Syed, and A. Voinov, Phys. Rev. C **76**, 044303 (2007).

[44] N. U. H. Syed, A. C. Larsen, A. Bürger, M. Guttormsen, S. Harissopulos, M. Kmiecik, T. Konstantinopoulos, M. Krtička, A. Lagoyannis, T. Lönnroth, K. Mazurek, M. Norby, H. T. Nyhus, G. Perdikakis, S. Siem, and A. Spyrou, Phys. Rev. C **80**, 044309 (2009).

[45] M. Guttormsen, U. Agvaanluvsan, E. Algin, A. Bürger, A. C. Larsen, G. E. Mitchell, H. T. Nyhus, S. Siem, H. K. Toft, and A. Voinov, EPJ Web of Conferences **2**, 04001 (2010).

[46] J. Kopecky and R. E. Chrien, Nucl. Phys. A **468**, 285 (1987).

[47] T. Belgya, O. Bersillon, R. Capote, T. Fukahori, G. Zhigang, S. Goriely, M. Herman, A. V. Ignatyuk, S. Kailas, A. Koning, P. Oblozinsky, V. Plujko and P. Young, *Handbook for calculations of nuclear reaction data, RIPL-2* (IAEA, Vienna, 2006). Available online at [http://www-nds.iaea.org/RIPL-2/].

[48] M. Guttormsen, M. Hjorth-Jensen, E. Melby, J. Rekstad, A. Schiller, and S. Siem, Phys. Rev. C **63**, 044301 (2001).

[49] S. C. Fultz, B. L. Berman, J. T. Caldwell, R. L. Bramblett, and M. A. Kelly, Phys. Rev. **186**, 1255 (1969).

[50] V. V. Varlamov, B. S. Ishkhanov, V. N. Orlin, V. A. Tchetvertkova, Moscow State Univ. Inst. of Nucl. Phys. Reports No. 2009, p. 3/847 (2009).

[51] V. V. Varlamov, N. N. Peskov, D. S. Rudenko, and M. E. Stepanov, Vop. At. Nauki i Tekhn., Ser. Yadernye Konstanty 1-2 (2003).

[52] A. Leprêtre, H. Beil, R. Bergere, P. Carlos, A. De Miniac, A. Veyssiere, and K. Kernbach, Nucl. Phys. **A 219**, 39 (1974).

[53] A. J. Koning, S. Hilaire, and M. C. Duijvestijn, *"TALYS-1.2"*, in *Proceedings of the International Conference on Nuclear Data for Science and Technology*, April 22-27, 2007, Nice, France. Editors: O. Bersillon, F. Gunsing, E. Bauge, R. Jacqmin, and S. Leray, EDP Sciences, 211 (2008). Available online at [http://www.talys.eu/].

[54] The ISOLDE facility, CERN. Online homepage available at [http://isolde.web.cern.ch/ISOLDE/].

[55] The SPIRAL2 facility, GANIL. Online homepage available at [http://www.ganil-spiral2.eu/].

[56] BrilLanCe®380 documentation, Saint-Gobain Crystals and Scintillation Products. Available online at [http://www.detectors-saint-gobain.com/].